REMOTE SENSING APPLICATIONS OF UNCOOLED LONG-WAVE INFRARED THERMAL IMAGERS

by

Jennifer Erin Johnson

A thesis submitted in partial fulfillment
of the requirements for the degree

of

Master of Science

in

Electrical Engineering

MONTANA STATE UNIVERSITY
Bozeman, MT

July 2012

APPROVAL

of a thesis submitted by

Jennifer Erin Johnson

This thesis has been read by each member of the thesis committee and has been found satisfactory regarding content, English usage, format, citation, bibliographic style, and consistency, and is ready for submission to The Graduate School.

Dr. Joseph A. Shaw

Approved for the Department of Electrical and Computer Engineering

Dr. Robert C. Maher

Approved for The Graduate School

Dr. Carl A. Fox

STATEMENT OF PERMISSION TO USE

In presenting this thesis in partial fulfillment of the requirements for a master's degree at Montana State University, I agree that the Library shall make it available to borrowers under rules of the Library.

If I have indicated my intention to copyright this thesis by including a copyright notice page, copying is allowable only for scholarly purposes, consistent with “fair use” as prescribed by the U.S. Copyright Law. Requests for permission for extended quotation from or reproduction of this thesis in whole or in parts may be granted only by the copyright holder.

Jennifer Erin Johnson

July 2012

ACKNOWLEDGMENTS

The completion of this thesis was made possible by many different people. It was funded in part by Army Night Vision & Electronic Sensors Directorate as a subcontract from the University of Montana in Missoula. I would like thank the members of Bee Alert Technology for their valuable assistance in imaging and working with the bee hives. This thesis was also partially funded by the Zero Emissions Research and Technology Center under the United States Department of Energy with Award No. DE-FC26-04NT42262. I would also like to thank the ZERT center for allowing me to run the thermal infrared imager and multispectral imager on their test site.

I would also like to acknowledge the many individuals without whom this thesis would not have been possible. My advisor Dr. Joseph Shaw gave me the opportunity to work in the Optical Remote Sensor Laboratory (ORSL) at Montana State University that started me on this research. His advice and guidance have been invaluable throughout the process. I would also like to thank the other members of my thesis advisory committee, Dr. Rick Lawrence and Dr. Todd Kaiser. Dr. Lawrence in particular worked with me to understand the meaning and interpretation of my results. Many of the members of the ORSL group have helped to make this research possible with their past work. Both Paul Nugent and Justin Hogan provided the camera calibrations and image manipulation software that made the imagers usable in the applications discussed in my thesis. Last, but certainly not least, I would like to thank my family and friends for the support and encouragement they freely gave throughout these last years, without whom the process would have been much more difficult.

TABLE OF CONTENTS

TABLE OF CONTENTS - CONTINUED

LIST OF TABLES

LIST OF TABLES - CONTINUED

Table Page

LIST OF FIGURES

LIST OF FIGURES - CONTINUED

LIST OF FIGURES - CONTINUED

LIST OF FIGURES - CONTINUED

LIST OF FIGURES - CONTINUED

LIST OF FIGURES - CONTINUED

Figure Page

ABSTRACT

The commercial development of microbolometer uncooled long-wave thermal infrared imagers in conjuncture with advanced radiometric calibration methods developed at Montana State University has led to new uses of thermal imagery in remote sensing applications. As a result of being uncooled, microbolometer imagers are notably lighter and cheaper than typical cooled imagers, making them ideal for remote sensing. Two novel uses are discussed in the work presented here. The first is the imaging of beehives in order to remotely determine the hive vitality. Bees thermally regulate their hives to a narrow range of temperatures that creates a thermal signature seen in thermal infrared images. For each of the hives imaged, frame counts (or the number of full frames of bees in each hive) were found by manual inspection. Linear regressions of the normalized frame counts of the hives were performed versus the measured hive thermal radiance values. The resulting plots showed a strong relationship between the normalized frame count and the mean radiance of each hive, particularly in images taken just prior to dawn. The second novel use was imaging vegetation exposed to large ground concentrations of CO_2 over a four-week period in summer for use in leak detection. A CO_2 leak was simulated in a test field run by the Zero Emissions Research and Technology Center. Thermal infrared images were acquired along with visible and near-infrared reflectance images of the exposed vegetation and healthy control vegetation. Thermal radiance statistics were measured and a regression was performed versus the day of the experiment. The infrared data were found to have a strong R^2 value and clearly show the effect of the CO_2 on the vegetation. An additional regression was run on the infrared data combined with the reflectance data, and this was found to not add any unique information to the vegetation reflectance data. Both methods were found to independently indicate the potential of a CO_2 leak before it was detected visually.

INTRODUCTION

Development of Microbolometers

The development and improvement of thermal infrared microbolometer arrays has greatly widened the field of passive infrared remote sensing. Starting in the late 1970s bulk and surface micromachining processes were used to form thermally isolated detectors onto silicon wafer substrates (Liddiard 2004). Initial work was sponsored by the U.S. Army Communication Electronics Command (CECOM) Night Vision and Electronic Sensors Directorate, along with the Defense Advanced Research Projects Agency (Kruse 2001). Bolometer arrays only became available for commercial use when the work became unclassified in 1992, which led to quick advances in the research and commercial infrared imaging markets. Semiconductor film bolometers were developed using silicon in order for the detector to be infrared-responsive and heat-sensitive. The temperature-sensing material is chosen to maximize the sensitivity of the microbolometers by selecting materials with high temperature coefficients of resistance and small 1/f noise constants (Niklaus 2007). Typical materials include vanadium oxide (VO_x), amorphous silicon (α-Si), and silicon diodes (Rogalski 2011). Uncooled infrared microbolometers are thermal detectors commonly used within the range of 8 – 14 μm (Geoffrey et al. 2000).

Conventional bolometer detectors are temperature-sensitive resistors that convert absorbed radiation into changes in electrical resistance and subsequent changes in bias voltage or current (Liddiard 2004). Each microbolometer pixel is composed of a detecting area, a reflector area, and a readout area. The detecting area typically consists of a thin silicon nitride (Si_3N_4) membrane upon which a thin film of vanadium oxide (VO_x) is deposited (Kruse 2001). The detecting area is elevated over the reflector surface using supports made of $Si3N_4$ in order to thermally isolate the absorption region. The reflector surface itself is an electrically conductive film mounted on a silicon substrate. As infrared radiation is absorbed by the detecting area, some of it passes through and is reflected upward by the reflector surface for maximum absorption. The infrared radiation heats the absorbing material, which causes a change in the resistance. This change is measured by a current that flows between electrodes embedded in the Si_3N_4 supports. Typically, a silicon substrate containing a readout integrated circuit (ROIC) serves as the bottom of each pixel in the detector. Equation 1 shows how the temperature change from ambient is related to a change in radiant power from the incident background radiant power.

$$\Delta T = \frac{\varepsilon \Delta P}{G_{th}} \qquad [1]$$

In this equation, ε is the emissivity, for a Lambertian surface that has zero net transmittance so that the emissivity is equal to the absorptivity. G_{th} is the thermal conductance between the detector and the background. For improved detection, the rise in temperature is made as great as possible by using maximum absorption and minimum thermal conduction. Maximum conductance is accomplished in microbolometers by building them as an optical cavity that functions as an absorption interference filter (Liddiard 2004). Minimum thermal conductance is achieved using thermally efficient mechanical construction and operation in a vacuum, typically around 0.01 mbar (Liddiard

2004). This vacuum surrounds only the bolometer detector and uses a window that often is used as the substrate for a filter that defined the detector's optical bandwidth. The thermal conduction can be as low as 3.5×10^{-8} W/K (Niklaus 2007). More recently, microbolometers were proposed that used two planes located at different levels in a bridge (Xu et al. 2011). These two-layer microbolometers have been found to have improved thermal and optical properties than one-layer microbolometers.

Previous infrared-detecting sensors typically were fabricated from material such as photo-conductive HgCdTe and were more sensitive than the microbolometer arrays, but required cryogenic cooling, making them less desirable for either commercial use with low cost or scientific use outside the laboratory. In addition to decreased sensitivity, microbolometer arrays have relatively poor uniformity. However, using micro-electro-mechanical-system (MEMS) processes has allowed microbolometers to become advantageous for remote-sensing applications. Their ability to work at room temperature means they can be used in smaller systems, consume less power, and cost less than cooled detectors (Katayama et al. 2009).

Most microbolometers are used in low-cost systems. This is a direct result of their low sensitivity compared to cooled detectors, as well as their high drift. Current applications include firefighter masks, military night-vision goggles, and night driving cameras. The microbolometer detectors give a general idea of where a hot target is, but do not provide reliable and detailed thermal readings. This makes them difficult to use in quantitatively accurate systems.

Infrared Cloud Imaging

Microbolometers used in infrared imagers allow for new and unique remote sensing applications that would not be practical with cooled imagers that have much higher cost and larger size. This results from being approximately an order of magnitude cheaper and smaller than typical cooled infrared imagers. However, the initial downside to using microbolometer detectors for quantitatively demanding remote sensing applications was the lack of a good means of calibrating them. The Optical Remote Sensor Lab at Montana State University has developed reliable calibration methods for long-wave microbolometer infrared cameras and has undertaken numerous projects using them. The original motivation for the use of microbolometer cameras in our lab was developing a system to remotely measure cloud spatial and temporal variability from the ground. This work was undertaken initially for climate research (Shaw et al. 2005), especially in the Arctic where clouds are extremely difficult to measure with satellites (Thurairajah and Shaw 2005).

A later application of infrared cloud imaging at our lab was measuring cloud statistics at potential Earth-space optical communication stations, which require clear communication paths (Nugent et al. 2007). Heavy cloud cover will result in blocking the communication link, and thin clouds will result in notable attenuation on the link, making it important to accurately assess the statistical cloud coverage. The 2nd-generation Infrared Cloud Imager (ICI2) was developed to be a ground-based thermal imaging system that provides high-spatial-resolution, localized cloud statistics (Nugent et al.

2007). A third generation of the system (ICI3) was developed subsequently to better characterize cloud statistics in both climate and optical communications research.

The ICI2 uses a 110° diagonal field-of-view Photon320 microbolometer camera core from FLIR Indigo Systems that is housed in a sealed enclosure. The enclosure also contains a heater, control circuitry, a fan to circulate air, a LVDS-to-Ethernet signal conversion module, and a baffle around the lens that shields the window from internal variable reflection (Nugent et al. 2009). The camera germanium lens has a hard carbon coating that allows the imager to be used outdoors with minimal degradation. Two different calibration methods were developed to improve the microbolometer detector performance. The first method used a blackbody that was cycled between two reference temperatures to generate a linear calibration curve defined by unique gain and offset terms (Shaw et al. 2005, Thurairajah and Shaw 2005, Nugent 2007). The second method used a laboratory calibration. In this method, the gain for each microbolometer pixel is determined from blackbody reference images, while the offset term is determined using the camera's shutter as a real-time calibration source (Nugent 2007). These calibration techniques were shown to produce highly accurate calibrations with a calibration accuracy of $\pm 0.57\ \mathrm{W \cdot m^{-2} \cdot sr^{-1}}$ achieved (Nugent et al. 2009).

Thesis Research

With the successful deployment of the ICI systems for long-term cloud measurements, further uses for radiometrically calibrated microbolometer infrared imagers were explored that required the proper calibration techniques. This thesis will discuss two newly developed applications for uncooled infrared microbolometer imagers. The first is to image beehives and remotely determine their vitality and estimate bee population. The second is to image vegetation exposed to elevated levels of soil CO_2 and thereby determine the location of a gas leak.

Beehive Infrared Imaging

Infrared imaging has been used in numerous biological monitoring applications, including locating honeybee hives inside house walls and observing hive thermoregulation patterns (Kastberger et al. 2003). Honeybees have been found to regulate their hive temperatures for many reasons. When honeybees are threatened by predators like wasps, they defend themselves by swarming around the wasp in order to raise the local temperature and kill it. Typically, honeybee defensive swarms will raise the temperature around the predator to 47°C, which is lethal to wasps and hornets, but not the honeybees (Kastberger et al. 2003 and Ono et al. 1995). Images acquired using mid-wave infrared imagers show these spikes in temperature (Ono et al. 1995). Additionally, honeybees will cluster together in winter to counteract the colder temperatures. Studies were performed using calibrated mid-wave infrared imagers to image hives fitted with infrared-transparent plastic panels to monitor the hive thermoregulation (Stabentheiner et al. 2003). Bees on the outside of the cluster, or mantle bees, were packed tighter, forming an insulation layer that reduces heat loss. Endothermic heat production was shown in infrared thermograms to occur in winter bee clusters and takes place at the core of the cluster, which assisted in warming the entire colony as well as the mantle bees (Stabentheiner et al. 2003). Hives that have brood, or egg, larva and pupa stages, must maintain temperatures of 33-36°C to ensure the survival of the colony (Kleinhenz et al. 2003). Heat is produced by vibrations in the bee's thoracic muscles, which is then transferred to sealed brood cells through conduction.

The Optical Remote Sensor Lab expanded on these findings by proposing a unique method using a compact, long-wave infrared imaging camera to non-invasively assess beehive vitality as a component of a systematic methodology of using honey bees for locating explosives (Shaw et al. 2010). Quickly assessing beehive vitality is also of interest to commercial bee keepers. There are approximately 2.5 million commercial honeybee hives nationwide that require hive inspections to maintain the health of the hives (Foley 2011). Many bee keepers manage tens of thousands of hives, making inspection of each hive impractical (Jensen 2011). Additionally, opening the hives in winter months could potentially harm a hive by exposing it to cold temperatures. Using an infrared thermal imager provides a quicker and more efficient means of monitoring larger numbers of hives to prevent colony collapse disorder (CCD) or other health issues.

In our infrared beehive imaging experiments, an uncooled microbolometer detector array was used to thermally image beehives at the University of Montana bee yard in Missoula, Montana. The resulting images were calibrated radiometrically using the methods developed originally for cloud imaging, and then processed using custom MATLAB scripts. The region occupied by each hive stack was selected in each image, and the mean, minimum, and maximum radiance values were calculated, along with the spatial standard deviation of the radiance. Comparisons to the background radiation were also made in order to contrast each hive's thermal signature. Once all the hives were processed, plots were generated showing the mean hive radiance, the difference between the maximum and minimum hive radiance values, the difference between the mean hive radiance and the mean background radiance, and the hive radiance spatial standard deviation. These were all plotted against the normalized frame count (the number of bee-filled frames inside each hive body divided by the number of bodies in each stack) (Shaw et al. 2010). The procedure and results are discussed in this thesis in Chapter 2.

Thermal Imaging of Vegetation to Detect Carbon Dioxide Leaks

Carbon sequestration has long been of interest in reducing CO_2 atmospheric concentrations. These CO_2 concentrations can be reduced by either creating artificial sinks or by enhancing natural diffusive sinks that have retention times of approximately tens to hundreds of years (Bach et al. 2003). Current methods of storing CO_2 include underground reservoirs, saline aquifers, and soil sequestration. Underground reservoirs depend on accurate capture, compression, transport, and injection of CO_2 gas. These reservoirs fall into four groups: underground caverns or mines, pore spaces between the grains of porous and permeable rocks, storage in depleted or abandoned oil and gas fields, and coal beds (Holloway 2001). Reservoir sequestration is in use at the Sleipner West gas field CO_2 storage operation in the North Sea, and the Burlington Resources pilot in the San Juan Basin (Holloway 2001). Saline aquifers sequester CO_2 by solubility trapping through dissolution in the natural water layer lying under oil or gas, mineral trapping through geochemical reactions with the aquifer fluids and rocks, or hydrodynamic trapping of a CO_2 plume (Bach et al. 2003). Saline aquifer sequestration is being developed at the Viking aquifer in the Alberta basin, Canada (Bach et al. 2003). Soil sequestration is based on the fact that soil is capable of storing carbon released naturally by organic materials. Additionally, plants can sequester atmospheric CO_2 by transporting it to their roots and then into the surrounding soil carbon concentration. CO_2 sequestration can be accomplished by trapping the gas under grass or legumes with the addition of lime and rock phosphates (Batjes et al. 1998). However, this method is not as accepted as the methods mentioned previously because of concerns for increased adverse environmental side-effects of increasing soil CO_2 concentrations.

All the methods of CO_2 sequestration rely on accurate and reliable monitoring systems to detect if the gas leaks, thereby re-entering the atmosphere or creating a health hazard. Underground reservoirs and saline aquifers have either natural or manmade connections to the surface through which their original contents were removed. The connections make it possible for the injected CO_2 to escape. Soil sequestration along with storage in porous rocks or coal beds depends on the pressure and temperature around the sequestered CO_2 remaining constant. Decreasing the pressure or raising the temperature could potentially force the gas to leak (Holloway 2001). Proposed and current means of leak detection include geochemical monitoring, pressure monitoring wells, and the deployment of carbon isotope ratiometers. Geochemical monitoring is a proposed system stating that leaking CO_2 would enter the groundwater, causing a noticeable change in water chemistry (Carrol et al. 2009). While this method is feasible for a CO_2 flux greater than 10^4 metric tons per year (t/yr) within a 15-month time period, it is ineffective for smaller leaks (Carrol et al. 2009). Pressure monitoring wells is a second proposed method that would install the wells over injection formations (Nogues et al. 2009). This method was shown to perform well in a simulation with two leaky CO_2 wells, but future work is required to expand this method to a more complex system of leaks.

Carbon isotope ratiometers rely on sequestered CO_2 having a different isotope ratio than other ambient sources like biogenic CO_2. The ratiometers would compare the isotope ratio of the CO_2 versus the inverse of the CO_2 concentration (McAlexander et al. 2011). A Los Gatos Research CO_2 Isotope Analyzer that used off-axis integrated cavity output spectroscopy was deployed to simultaneously measure the gas concentration and the carbon isotope ratio at the Zero Emissions Research and Technology (ZERT) site in Bozeman, Montana (McAlexander et al. 2011). It was found that the system should be capable of detecting upwind CO_2 leaks at approximately 10-15 m from the leak location (McAlexander et al. 2011).

Since the winter of 2006, the ZERT site has been used to simulate CO_2 leaks, as well as test surface monitoring techniques. These release experiments have been used as opportunities to test a variety of optical methods of detecting the leaking gas indirectly by observing changes in vegetation reflectance spectra. It has been shown that high concentrations of CO_2 in the soil cause decreases in leaf chlorophyll, meaning leaks can be detected by examining leaf reflectance (Noomen et al. 2009). By observing the stress patterns in the vegetation at the ZERT site, CO_2 leaks can be located. Experiments based on this idea have been conducted at the ZERT site with hyperspectral and multispectral imaging. For example, during the 2008 CO_2 release, a cart-mounted spectrometer was used to determine the hyperspectral reflectance signatures of the site's vegetation from

350 to 2,500 nm with a 1-nm bandwidth (Male et al. 2010). Hyperspectral plant signatures were compared from the start of the release to the end to identify stressed plants, or plants growing in unfavorable environments (Male et al. 2010). Leaks were successfully identified using the hyperspectral signatures within four days of the release (Male et al. 2010).

Hyperspectral imagery was also used during the 2007 release where an imager was mounted on a tripod 1 m from the vegetation. A patch of vegetation approximately 20 cm x 20 cm was imaged through the release in the 400-900 nm spectral range (Keith et al. 2009). The resulting data indicated a threshold response of plant health as a response the release of the CO_2. During the 2010 release, an aerial imaging campaign was performed using a Pika hyperspectral imager from Resonon in order to quantify and characterize the spectral changes in the exposed vegetation (Bellante 2011). Eight sets of images were collected covering before the release start, during the release, and after the release. The spectral data was collected throughout the 424-929 nm wavelengths (Bellante 2011). This method was found to provide broad spatial coverage of the CO_2 release that demonstrated a divergence of the effected vegetation from the healthy vegetation. Another method tested during the 2007 and 2008 releases was to use a multispectral imaging system with customized wide-angle optics mounted on a platform adjacent to the ZERT plant test region. The camera split the incoming light into green (500 - 580 nm), red (630-710 nm), and NIR (735-865 nm) bands, from which each band's calibrated reflectance data was averaged over several different portions of the test region (Rouse et al. 2010). It was found that as the vegetation became stressed over the duration of the release, the NIR reflectance fell, the red reflectance rose, and the red edge shifted to shorter wavelengths (Rouse et al. 2010). By comparing the calculated normalized difference vegetation index, NDVI, reflectance of stressed vegetation with those of non-stressed vegetation the effects of the injected CO_2 were clearly seen. NDVI is determined from the near infrared (NIR) and red reflectances using Equation 2.

$$NDVI = \frac{NIR-RED}{NIR+RED} \qquad [2]$$

In 2010, a second, lower-cost, multispectral imaging system was designed and deployed in the ZERT field between July 19 and August 15. A 1.3 Megapixel CMOS camera was used with 1280 x 1024 pixels and a 6.7 μm pixel pitch (Hogan et al. 2012). As with the previous multispectral imager, red and NIR spectral bands were used to determine the NDVI to detect plant stress. This imaging method was able to detect CO_2-induced changes within two-to-three days of the start of the release (Hogan et al. 2012a, Hogan et al. 2012b).

We expanded on the findings of the multispectral imager by adding a long-wave infrared imaging camera to compare the radiance of the exposed vegetation to that of healthy vegetation. A FLIR photon 320 core infrared camera was used to acquire images of the ZERT field over the duration of the 2010 and 2011 releases. After calibrating the images radiometrically, three regions were selected for comparison: two control spots and a spot located near a CO_2 leak. The mean, maximum, and minimum radiance, as well as the radiance spatial standard deviation, were analyzed over time using a linear regression analysis. The simple linear regression consisted of fitting a straight line through each set of measured radiance values so that the sum of the squared residuals of each model became as small as possible. Further regressions were carried out to compare the statistical significance of the reflectance band data relative to the thermal infrared data. The procedure and its results are discussed in this thesis in Chapter 3.

Thesis Overview

This thesis provides descriptions and results from two novel uses for radiometrically calibrated, uncooled, microbolometer-based, long-wave infrared imagers. This work is presented in five chapters including this introduction. Chapter 2 presents the methodology and results of thermal imaging of beehives in order to noninvasively determine their population and hive vitality. Chapter 3 presents the use of the same type of long-wave infrared camera to detect CO_2 leaks in the ZERT test field near the Montana State University-Bozeman campus. Chapter 4 presents a comparison of the long-wave infrared camera results from monitoring the CO_2 leak with those from a two-band visible and near-infrared spectral imager. Chapter 5 provides concluding remarks on the work presented in this thesis and discuses future work that would further these applications. Overall, this thesis discusses two original applications of microbolometer infrared imagers for radiometrically calibrated remote-sensing purposes.

References

Bachu, S. and J.J. Adams. "Sequestration of CO_2 in Geological Media in Response to Climate Change: Capacity of Deep Saline Aquifers to Sequester CO_2 in Solution." *Energy Conversion and Management* 44.20 (2003) : 3151-3175.

Batjes, N.H. "Mitigation of Atmospheric CO_2 Concentrations by Increasing Carbon Sequestration in the Soil." *Biology and Fertility of Soils* 27.3 ((1998) : 230-235.

Bellante, Gabriel John. "Hyperspectral Remote Sensing as a Monitoring Tool for Geological Carbon Sequestration." MA thesis Montana State University, Bozeman, 2011. Web.

Carroll, Susan, Yue Hao, and Roger Aines. "Geochemical Detection of Carbon Dioxide in Dilute Aquifers." *Geochemical Transactions* 10.4 (2009).

Ehlig-Economides, Christine and Michael J. Economides. "Sequestering Carbon Dioxide in a Closed Underground Volume." *Journal of Petroleum Science and Engineering* 70.1-2 (2010) : 123-130.

Foley, I., Personal Correspondence to P. W. Nugent, State Entomologist, Montana Department of Agriculture, February 2011.

Geoffray, Herve, Alain Bardoux, Michel Laporte, and Jean-Luc Tissot, "Uncooled Infrared Microbolometer Arrays for Earth Remote Sensing", Proc. SPIE 4130, 527 (2000).

Hogan, Justin A., Joseph A. Shaw, Rick L. Lawrence, and Randal M. Larimer. "Low-cost Multispectral Vegetation Imaging System for Detecting Leaking CO_2 Gas." *Applied Optics* 51.4 (2012a) : 59-66.

Hogan, Justin A., Joseph A. Shaw, Rick L. Lawrence, Jennifer L. Lewicki, Laura M. Dobeck, and Lee H. Spangler, "Detection of Leaking CO_2 Gas ith Vegetation Reflectance Measured by a Low-Cost Multispectral Imager," *IEEE J. Selected Topics Appl. Earth Obs. Remote Sensing* 5.3 (2012b) : 699-706.

Holloway, Sam. "Storage of Fossil Fuel-Derived Carbon Dioxide Beneath the Surface of the Earth." *Annual Review of Energy and the Environment* 26 (2001) : 145-166.

Jensen, M., 2011: Personal correspondence to P. W. Nugent, Smoot Honey Company, Power, MT.

Kastberger, Gerald and Reinhold Stachl. “Infrared Imaging Technology and Biological Applications.” *Behavioral Research Methods, Instruments, & Computers* 35.3 (2003) : 429-439.

Katayama, Haruyoshi , Masataka Naitoh, Masahiro Suganuma, Masatomo Harada, Yoshihiko Okamura, Yoshio Tange, and Koji Nakau. “Development of the Compact InfraRed Camera (CIRC) for Wildfire Detection.” Proc. SPIE7458 (2009).

Keith, Charlie J., Kevin S. Repasky, Rick L. Lawrence, Steven C. Jay, and John L. Carlsten. “Monitoring Effects of a Controlled Subsurface Carbon Dioxide Release on Vegetation Using a Hyperspectral Imager.” *International Journal of Greenhouse Gas Control* 3:5 (2009) : 626-632.

Kleinhenz, Marco, Brigitte Bujok, Stefan Fuchs, and Jürgen Tautz. “Hot Been in Empty Broodnest Cells: Heating From Within.” *The Journal of Experimental Biology* 206.23 (2003) : 4217-4231.

Kruse, Paul W. *Uncooled Thermal Imaging: Arrays, Systems, and Applications*. Bellingham: ASPIE-The International Society for Optical Engineering, 2001. Print.

Liddiard, Kevin C. “The Active Microbolometer: A New Concept in Infrared Detection.” *Microelectronics: Design, Technology, and Packaging* Proc. SPIE 5274, 227 (2004).

Male, Erin Jing, William L. Pickles, Eli A. Silver, Gary D. Hoffmann, Jennifer Lewicki, Martha Apple, Kevin Repasky, and Elizabeth A. Burton. “Using Hyperspectral Plant Signatures for CO_2 Leak Detection During the 2008 ZERT CO_2 Sequestration Field Experiment in Bozeman, Montana.” *Environmental Earth Sciences* 60.2 (2010) : 251-261.

McAlexander, Ian, Greg H. Rau, Jimmy Liem, Thomas Owano, Ray Fellers, Douglas Baer, and Manish Gupta. “Deployment of a Carbon Isotope Ratiometer for the Monitoring of CO_2 Sequestration Leakage.” *Analytical Chemistry* 83.16 (2011) : 6223-6229.

Niklaus, Frank, Christian Vieider, and Henrik Jakobsen, "MEMS-Based Uncooled Infrared Bolometer Arrays: a Review", Proc. SPIE 6836, 68360D (2007).

Nogues, Juan P., Jan M. Nordbotten, and Michael A. Celia. “Detecting Leakage of Brine or CO_2 Through Abandoned Wells in a Geological Sequestration Operation Using PressureMonitoring Wells.” *Energy Procedia* 4 (2011) : 3620-3627.

Noomen, M.F. and A.K. Skidmore. "The Effects of High Soil CO_2 Concentrations on Leaf Reflectance of Maize Plants." *International Journal of Remote Sensing* 30.2 (2009) : 481-497.

Nugent, Paul W., Joseph A. Shaw, and Sabino Piazzolla. "Wide Angle Infrared Cloud Imaging for Measuring Cloud Statistics in Support of Earth Space Optical Communication." Proc. SPIE 6709 (2007).

Nugent, Paul W. "Wide-Angle Infrared Cloud Imaging for Cloud Cover Statistics." MA thesis Montana State University, Bozeman, 2008. Web.

Nugent, Paul W., Joseph A. Shaw, and Sabino Piazzolla. "Infrared Cloud Imaging in Support of Earth-Space Optical Communication." *Optics Express* 17.10 (2009).

Ono, Masato, Takeshi Igarashi, Eishi Ohno, and Masami Sasaki. "Unusual Thermal Defence by a Honeybee Against Mass Attack by Hornets." *Nature* 377 (1995) : 334-336.

Rogalski, Antoni. "Infrared Detectors: An Overview." *Infrared Physics & Technology* 43.3-5 (2002) : 187-210.

Rouse, Joshua H., Joseph A. Shaw, Rick L. Lawrence, Jennifer L. Lewicki, Laura M. Dobeck, Kevin S. Repasky, and Lee H. Spangler. "Multi-spectral Imaging of Vegetation for Detecting CO_2 Leaking From Underground." *Environmental Earth Sciences* 60.2 (2010) : 313-323.

Shaw, Joseph A., Paul W. Nugent, Nathan J. Pust, Brentha Thurairajah, and Kohei Mizutani, "Radiometric Cloud Imaging with an Uncooled Microbolometer Thermal Infrared Camera," *Optics Express* **13**(15), 5807-5817, http://dx.doi.org/10.1364/OPEX.13.005807 (2005).

Shaw, Joseph A., Paul W. Nugent, Jennifer Johnson, Jerry J. Bromenshenk, Colin B. Henderson, and Scott Debnam. "Long-wave Infrared Imaging for Non-invasive Beehive Population Assessment." *Optics Express* 19.1 (2011) : 399-408.

Stabentheiner, Anton, Helga Pressl, Thomas Papst, Norbert Hrassnigg, and Karl Crailsheim. "Endothermic Heat Production in Honeybee Winter Clusters." *The Journal of Experimental Biology* 206.2 (2003) : 353-358.

Thurairaijah, Brentha and Joseph A. Shaw, "Cloud Statistics Measured with the Infrared Cloud Imager," *IEEE Trans. Geosci. Remote Sens.* **43**(9), 2000-2007 (2005).

Xu, Xiangdong, Zhuo Yang, Zhi Wang, Chao Chen, Dong Zhou, Yang Yang, and Yadong Jiang. “Advanced Design of Microbolometers for Uncooled Infrared Detectors.” *2011 International Conference on Information Science and Technology* (2011) : 745.

NON-INVASIVE DETERMINATION OF BEEHIVE POPULATION

The purpose of this chapter is to show the use of a calibrated microbolometer-based long-wave infrared camera for non-invasively imaging and monitoring beehives. For the study, beehives at the University of Montana bee yard in Missoula, Montana were imaged repeatedly throughout the summers of 2010 and 2011. The bee yard is located at latitude 46.839° and longitude -114.056°. Appendix A contains maps of the bee yard at each date images were acquired. The bee yard is a fenced area containing seven tables of beehives, a wooden shed, a metal shed, and a concrete utility shed. These structures were assumed to not contribute to the thermal signatures of the hives. Careful notes were taken in order to track which hive stacks were present at each imaging. Each hive stack was composed of one or more numbered hive bodies, with each body containing up to ten honey frames. Some of the imaged hive stacks were only half the width of normal hive stacks. Figure 1(a) shows an example image of a table containing six hive stacks, with a total of 15 hive bodies, while Figure 1(b) shows an example hive body interior containing the ten honey frames.

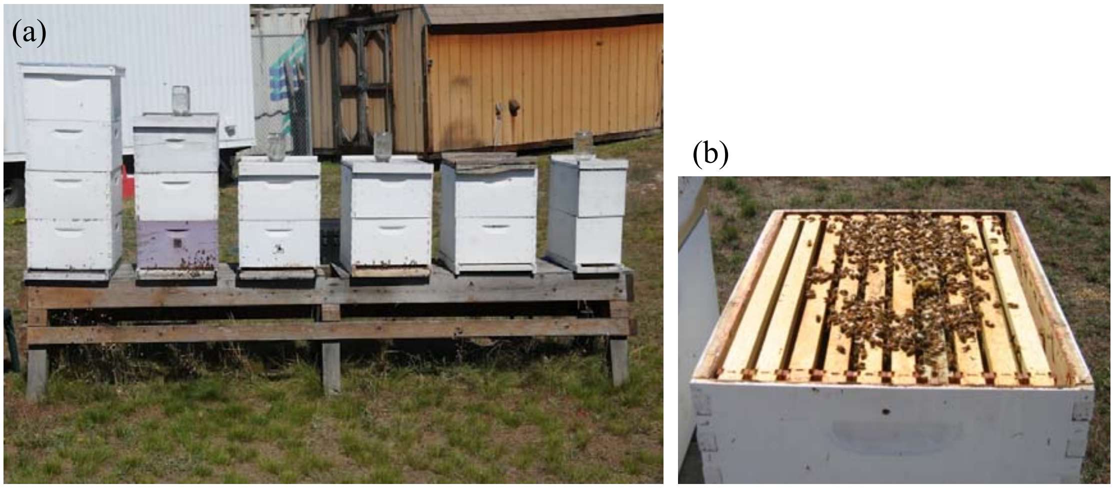

Figure 1. Example image of (a) table containing six hive stacks and (b) interior of a hive body containing ten honey frames. (J. A. Shaw 2010)

Different hives were found to have much different thermal signatures. The premise of this method is that a stronger thermal signature is caused by a greater number of bees within the hive. Figure 2 shows a group of hives containing both stronger and weaker hives that we made initial observations on and confirmed with the Missoula bee keeper.

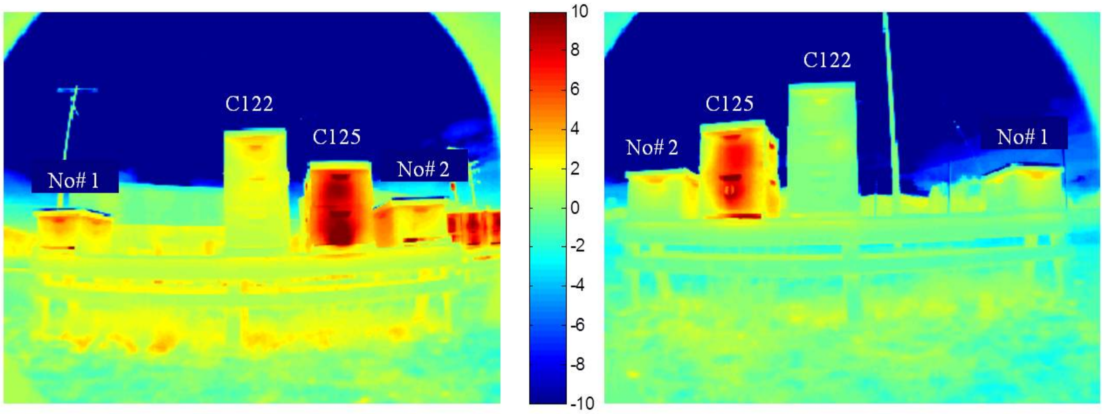

Figure 2. Hive backs (left) and fronts (right) for Table A May 12, 2010 AM. (Johnson)

The thermal signatures in Figure 2 imply that hive C125 contained a larger bee population than the other three hives present. Additionally, hive C122 appeared to be relatively empty of thermally active bees. Data supplied from the beekeeper stated that hive C125 was a healthy, well-established hive, meaning it contained a strong bee population and was actively storing honey and incubating brood. Hive C122 was listed as a dying, nearly empty hive, supporting our conclusions that it was a weaker hive. Hives No#1 and No#2 were listed as new, un-established hives, which accounts for their present, but weak, thermal signatures.

Hive frame counts, or the number of honey frames considered full of bees, were either supplied by our collaborators, Bee Alert Technology, Inc., of Missoula, or were found manually by us with visual inspection. In May 2010 each honey frame contained approximately 5,000 bees (Shaw et al. 2011), but the number of beehives varied between each imaging period. Table 1 shows the variation in number of hives from January 2010 to September 2010 and July 2011 to September 2011.

Table 1. Summary of Missoula bee yard hives for 2010 and 2011.

Imaging Period	**Number of Beehives**		
	Hive Stacks	Hive Bodies	Full Frames
January 27, 2010 – January 30, 2010	23	45	Unknown
May 12, 2010 – May 13, 2010	33	65	322
August 2, 2010 – August 5,2010	32	87	400
July 7, 2011 – July 8, 2011	37	74.5	Unknown
July 20, 2011 – July 21, 2011	12	29.5	141
August 24, 2011 – August 26, 2011	36	93	450
September 21, 2011 – September 22, 2011	40	101	507

The small number of hives from July 20, 2011-July 21, 2011 was a result of the majority of bee hives being transported to a demonstration experiment in Missouri.

Methodology

All the bee hive thermal images were acquired using a FLIR Photon 320 uncooled infrared camera core, with 324 x 256 microbolometer pixels and an optical bandwidth of 7.5 – 13.5 µm. An f/1.4 lens with 8.6-mm focal length was used to image groups of hives with a field of view of 86° x 67°. The camera was mounted inside a rain shield on a tripod, approximately 3-4 m from the hives. This distance allowed an entire table of hives to be imaged simultaneously, with the width of each hive body occupying approximately 40 pixels. Figure 3 shows the infrared camera positioned in front of a hive table.

Figure 3: FLIR Photon 320 infrared imager. (J. A. Shaw 2011)

This camera was calibrated using a custom calibration technique developed at the Optical Remote Sensor Laboratory at Montana State University, with a radiometric uncertainty of 0.5 W m^{-2} sr^{-1} (Shaw et al. 2011). All the thermal images were acquired approximately one hour after local sunset and just before the local sunrise in order to avoid solar heating effects on the hive surfaces. This also gave greater thermal contrast between the hive bodies and the background, making it easier to select only the hives during processing. The camera also was allowed to stabilize for a minimum of 20 minutes before use, which is accomplished by leaving the camera running in the ambient atmosphere. A blackbody source set alternately at 10°C and 60°C was also imaged for reference, as well as for validation of the camera calibration.

With the infrared camera correctly stabilized and positioned, each table of hives was imaged from the front and the back. The front side was determined as the side with the hive entrances. Throughout the imaging period, atmospheric data were recorded, including air temperature, wind speed, and humidity, as well as observed cloud cover, rain. The atmospheric conditions were recorded to rule out or understand their effects on the hive thermal signatures. For each table, 5-10 images were acquired at a time to generate an average thermal image later with any anomalies removed. These images were stored on a laptop computer for later processing.

Thermal infrared images were processed in the manner described in the following section, and linear regressions were calculated for the normalized frame count (the number of bee-filled frames inside each hive body, divided by the number of bodies in the hive stack), plotted versus various parameters calculated from the thermal images. It is important to note that all the linear regressions performed on the data used the normalized frame counts as the dependent variable and the statistical parameters from the thermal images as the independent variables. This allowed the coefficients of determination (R^2 values) from the regressions for each image set to be reliably compared. The R^2 value is computed for each regression as the sum of squares divided by the residual sum of squares. In this manner, the R^2 value describes the fraction of the measurement variance that is explained by the regression model.

Image Processing

The hive images were calibrated radiometrically using previously developed MATLAB scripts (Nugent 2008). After calibration, each set of images for a single table of hives was averaged into a single image. Custom MATLAB software was used to select the pixel region occupied by each entire hive in each image. In the selection process it was critical that the hive sides, tops, background, or entrances not be selected. The sides were excluded because of thermal coupling between adjacent hive stacks caused by their close spacing. The hive tops were excluded because they are primarily made of metal, meaning they easily reflect the ambient environment and do not provide accurate measurements of the hive's interior thermal signature. Since the hive tops ranged from painted white to bare metal, the variance introduced from the various tops was used to justify excluding them from the selection process. The metal tops in particular would reflect the environment, meaning the measured thermal values had no relation to the hives. Figure 4 shows a single selected hive for the data processing.

Figure 4. The black box indicates the selection of a single hive for processing. Table F, hive C1010, the evening of 8/24/2011. (image courtesy of Jennifer Johnson)

Hive entrances were also excluded when the hive fronts were selected, due to the heat escaping directly from the hive interior, which skews the measured radiance relative to the value observed without the entrance. A second method of selection was tried where only the hive entrances were selected and compared. This method was found to yield stronger regressions, particularly for the images acquired at night. A comparison of the regression coefficients found when selecting entire hive fronts and only hive entrances is shown in Table 2.

Table 2. Comparison of the coefficients of determination for selecting entire hive front vs selecting only the entrance.

Date	Mean		Max-Min		Mean-Background		STDV	
	Front/Entrance		Front/Entrance		Front/Entrance		Front/Entrance	
May 12, 2010 AM	0.489	0.494	0.295	0.463	0.566	0.494	0.491	0.490
May 12, 2010 PM	0.248	0.434	0.134	0.356	0.228	0.420	0.167	0.377

This suggests that a convenient and simple hive-monitoring method could be based on a hand-held non-imaging radiometer pointed at the hive entrances. However, even stronger regressions were found when selecting the backs of hives in the infrared images.

A third method of selection was attempted by selecting the individual hive bodies, but the effects of thermo-coupling between the bodies in a vertical stack made this method unreliable. Since each hive body was made of wood, and the lower bodies were open at the top, heat transfer between occupied and unoccupied hive bodies in a single stack provided false indications of bees. Therefore, the best results were obtained by selecting each hive stack as an integrated unit. A region near the hives was selected as the background radiance value. For the 2011 images, the background for each image was chosen to be the table supporting the hives. Each table in the bee yard was made of similar wood and construction methods, providing a uniform background level for each table of hives in the images. Images from previous years used the grass near the tables as a background reference, which introduced large amounts of variability into the background values.

After the selection of each hive stack, the MATLAB software calculated the mean, minimum, maximum, and spatial standard deviation of the hive's radiance. With these data recorded, plots were generated of the normalized frame count versus the mean hive radiance, the difference between the maximum and minimum hive radiance, the difference between the mean hive radiance and the mean background radiance, and the spatial standard deviation of the hive radiance (Shaw et al. 2011). All the image collections, except for the July 7, 2011 – July 8, 2011 set and the January 27, 2010 – January 30, 2010 set, were plotted in this manner. These particular sets were not plotted, due to the lack of frame counts for those time periods.

The 2011 images sets were scaled using infrared images taken of a blackbody. The blackbody was imaged at two different temperatures: once at the start of the imaging session at 10°C and once at the end of the imaging session at 60°C. A linear equation was developed using two known temperatures of the blackbody and the two measured temperature values in the images. This equation was then applied to the measured thermal radiance values of the hives to yield a scaled radiance value. Scaling the radiance values compensated for the atmospheric emission between the camera and the hive bodies.

Results

May 2010

The first set of results from 2010 was for the morning of May 12, 2010. Imaging started at 5:45 AM with the local sunrise occurring at 6:05 AM. The observed sunrise was approximately 10 minutes later due to the hills to the east of Missoula. The temperature ranged between 0.1– 5.3 °C, with a relative humidity of 51% and a pressure of 895 mb. These images were the first infrared images acquired of the beehives in the spring instead of the winter months. Prior to this, images were acquired during the fall and winter while the hives were entirely dormant. Additionally, the thermal camera was allowed to stabilize for 20 minutes, unlike in previous imaging sets. The resulting radiance statistics are shown in Figures 5-8 consisting of plots of normalized frame count versus the following parameters: mean radiance, the difference between the maximum and minimum hive radiances, the difference between hive mean radiance and the background mean radiance, and the spatial standard deviation.

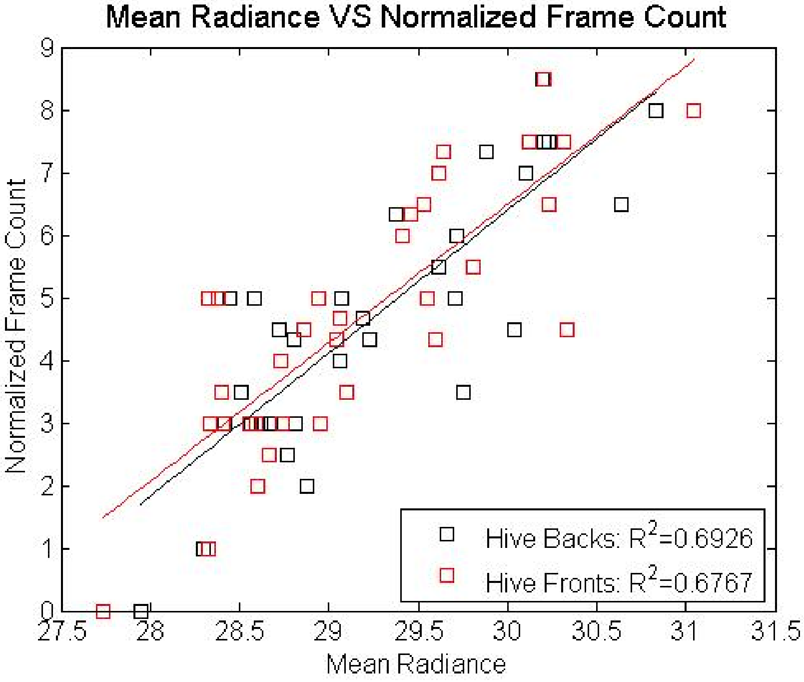

Figure 5. Normalized frame count plotted vs. mean radiance for 5/12/2010 AM

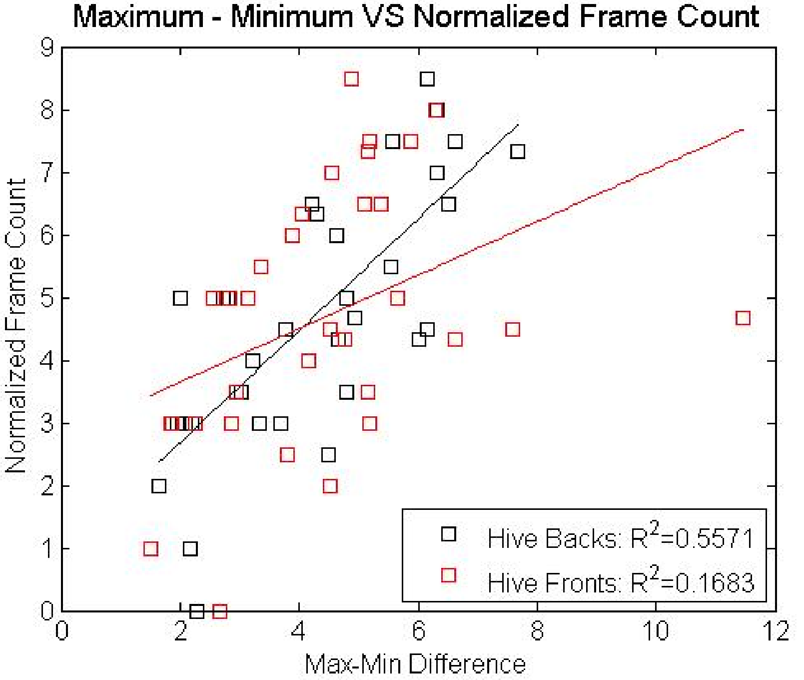

Figure 6. Normalized frame count plotted vs. difference between maximum and minimum radiance for 5/12/2010 AM

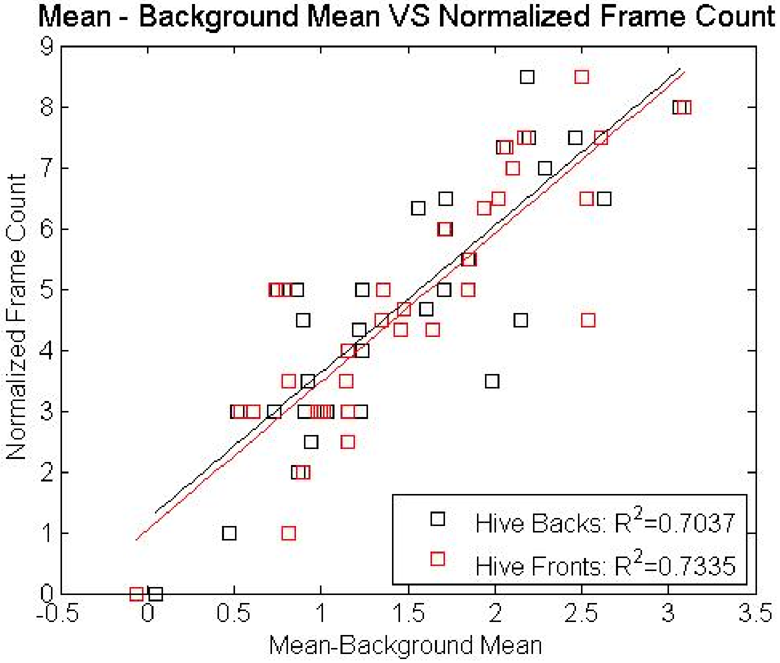

Figure 7. Normalized frame count plotted vs. difference between mean and background mean radiance for 5/12/2010 AM

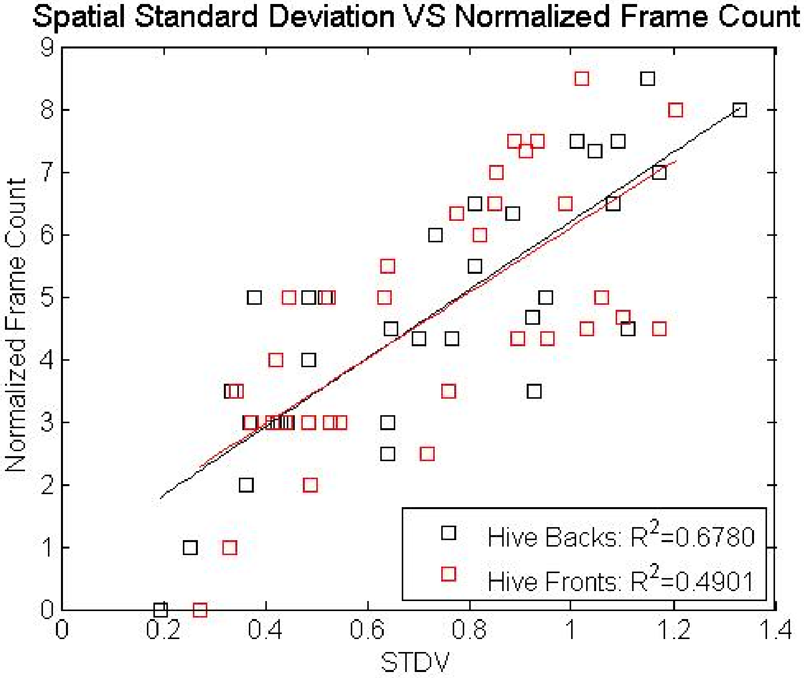

Figure 8. Normalized frame count plotted vs. spatial standard deviation of radiance for 5/12/2010 AM

Images were acquired again on the evening of May 12, 2010. Imaging started at 9:30 PM with the local sunset occurring at 9:01 PM. The temperature was measured to be 6.4 °C with a relative humidity of 31% and a pressure of 899 mb. The resulting radiance statistics are shown in Figures 9-12.

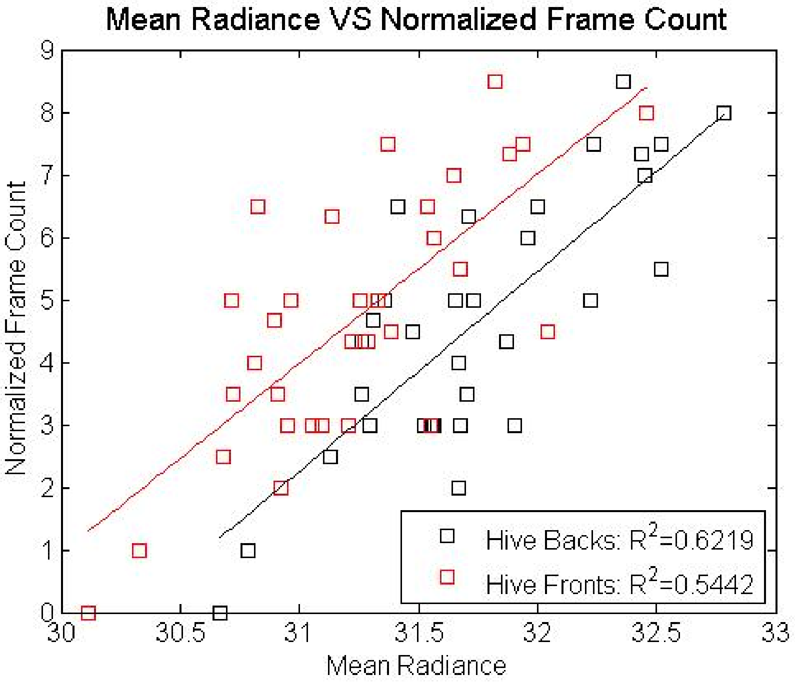

Figure 9. Normalized frame count plotted vs. mean radiance for 5/12/2010 PM

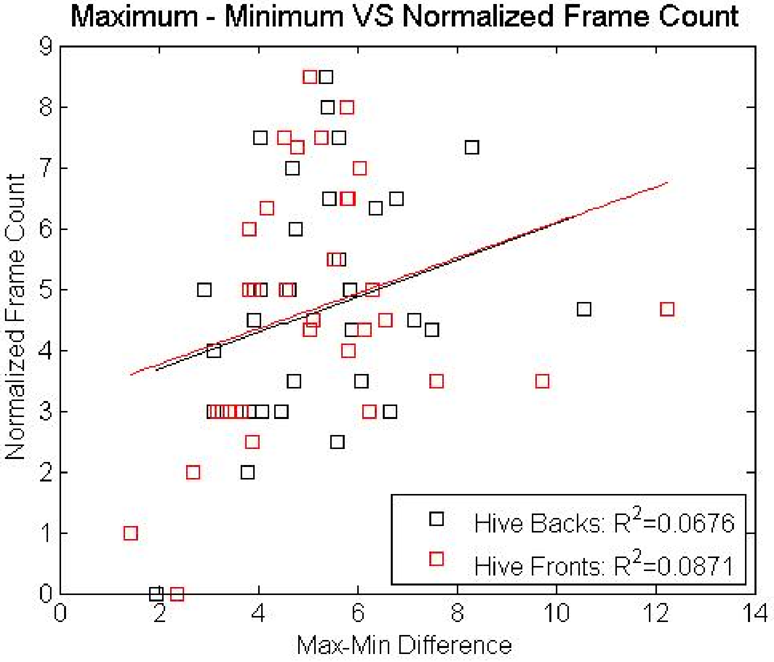

Figure 10. Normalized frame count plotted vs. difference between maximum and minimum radiance for 5/12/2010 PM

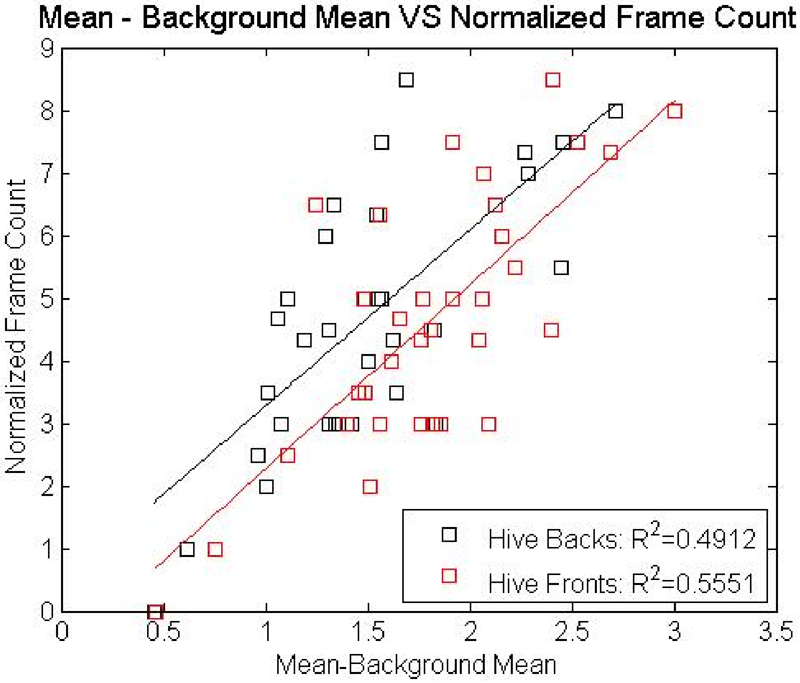

Figure 11. Normalized frame count plotted vs. difference between mean and background mean radiance for 5/12/2010 PM

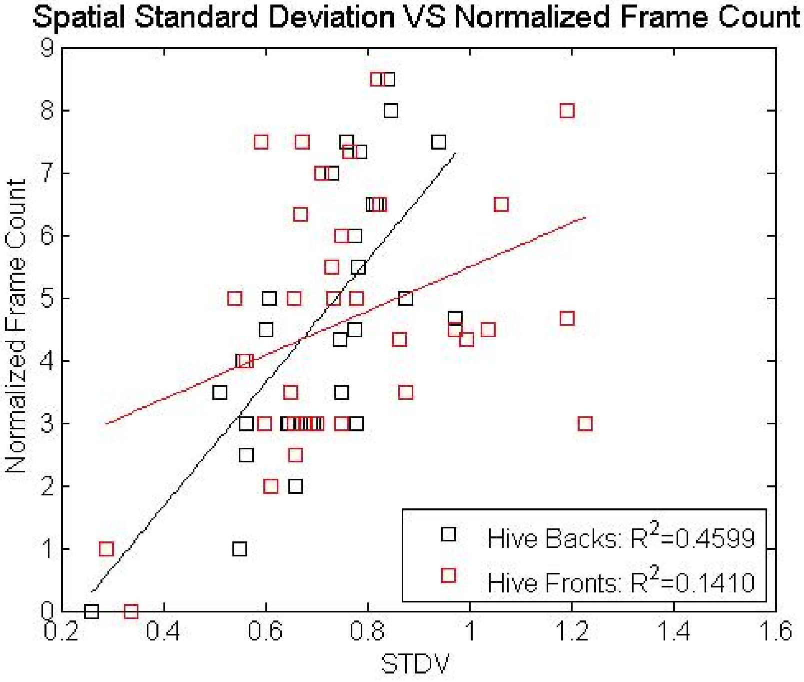

Figure 12. Normalized frame count plotted vs. spatial standard deviation of the radiance for 5/12/2010 PM

A third set of images were acquired on the morning of May 13, 2010. Imaging started at 5:50 AM, with the local sunrise occurring at 6:04 AM. The temperature was measured to range from -4.0 – 3.5 °C, with the relative humidity staying nearly constant at 45% and the pressure at 900 mb. The resulting radiance statistics are shown in Figures 13-16.

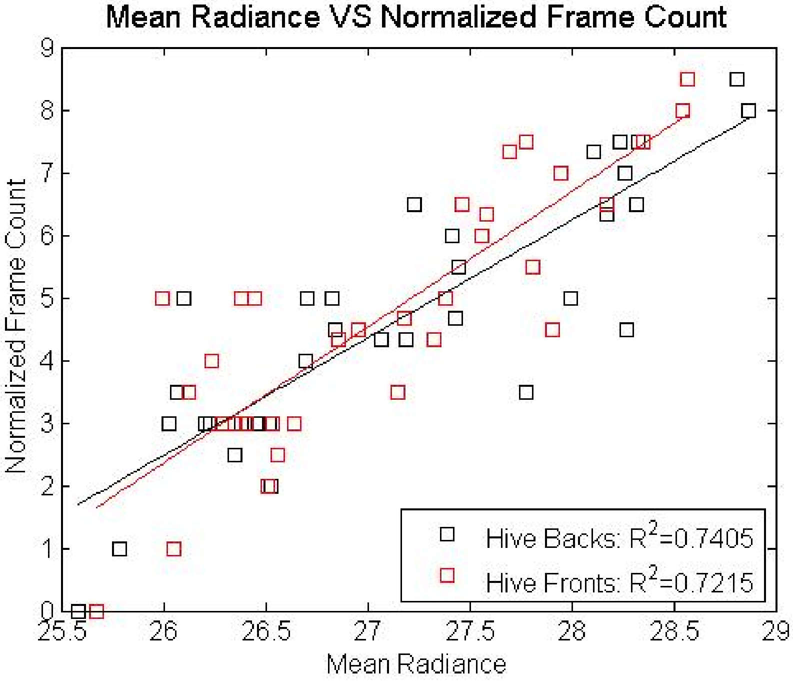

Figure 13. Normalized frame count plotted vs. mean radiance for 5/13/2010 AM

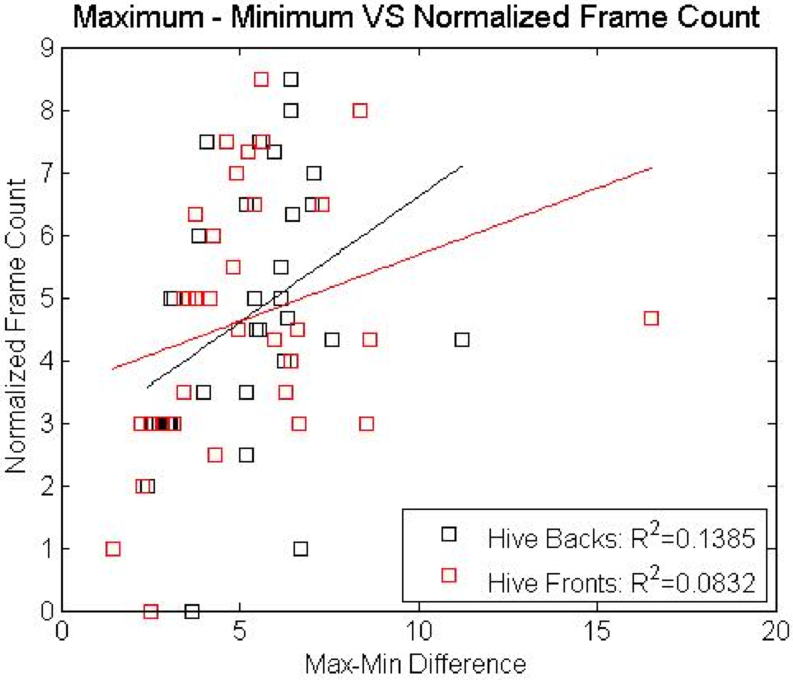

Figure 14. Normalized frame count plotted vs. difference between maximum and minimum radiance for 5/13/2010 AM

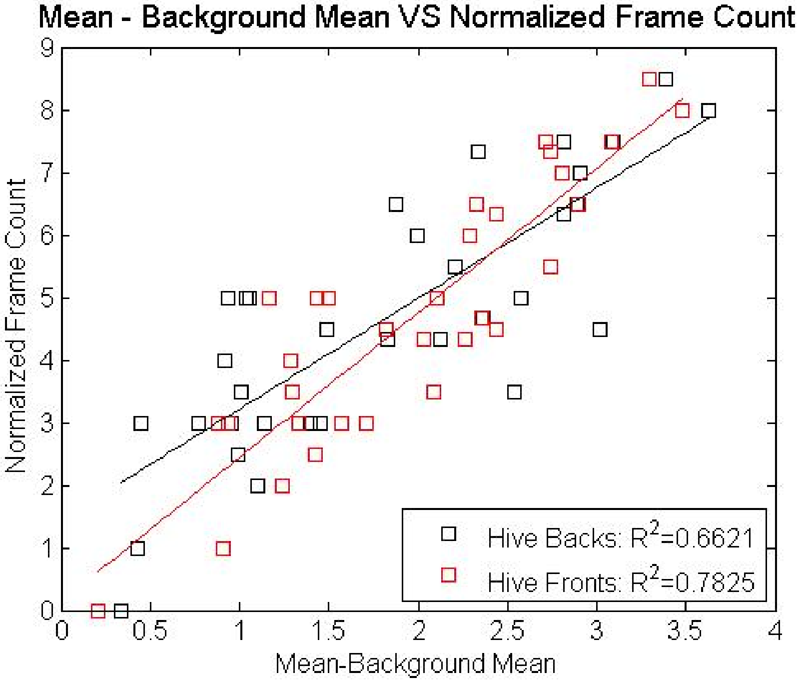

Figure 15. Normalized frame count plotted vs. difference between mean and background mean radiance for 5/13/2010 AM

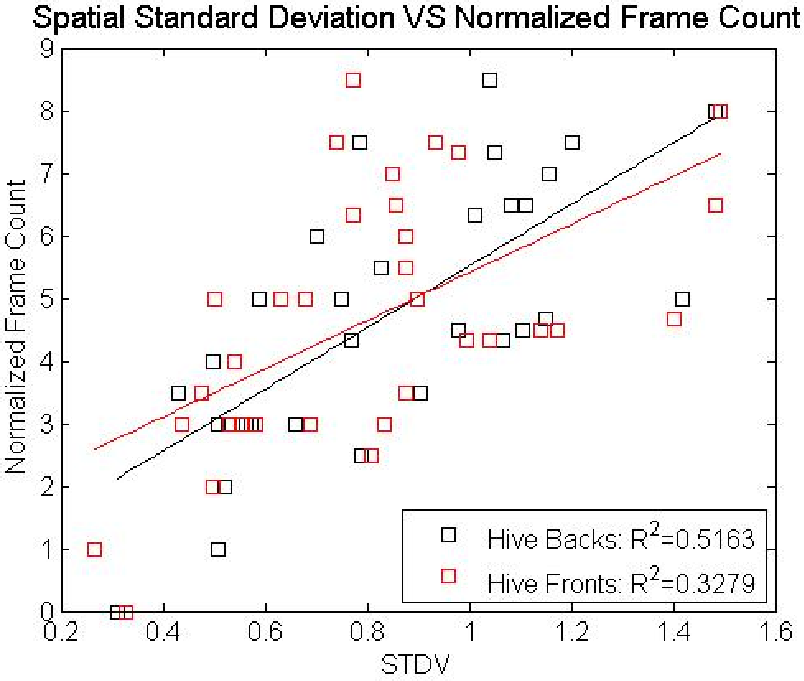

Figure 16. Normalized frame count plotted vs. spatial standard deviation of the radiance for 5/13/2010 AM

These image sets show similar results, which are summarized in Table 3. The morning results were found to give higher coefficients of determination than those of the evening. This could be a result of residual thermal heating in the evening or the result of the hives having higher thermal contrast due to the cooler morning temperatures. For each day, the strongest coefficients of determination (R^2) were found for the plot of mean radiance for each hive and the plot of the difference between the mean and background radiance for each hive. Hive backs had the highest R^2 values for mean radiance, while the hive fronts had the greatest R^2 values for the difference in mean and background mean radiance.

Table 3. Summary of R^2 values for the image sets from 5/12/2010 AM - 5/13/2010 PM.

		May 12, 2010 AM	**May 12, 2010 PM**	**May 13, 2010 AM**
Hive Backs	Mean	0.693	0.622	0.741
	Maximum-Minimum	0.557	0.068	0.139
	Mean-Background Mean	0.704	0.491	0.662
	STDV	0.678	0.460	0.516
Hive Fronts	Mean	0.677	0.542	0.722
	Maximum-Minimum	0.168	0.087	0.083
	Mean-Background Mean	0.734	0.555	0.783
	STDV	0.490	0.141	0.328

August 2010

Images were acquired on the night of August 2, 2010. Imaging started at 10:15 PM, with the local sunset occurring at 9:07 PM. The temperature was measured to range from 21.1–22.2°C, with the relative humidity staying nearly constant at 45% and the pressure at 904 mb. The resulting radiance statistics are shown in Figures 17-20.

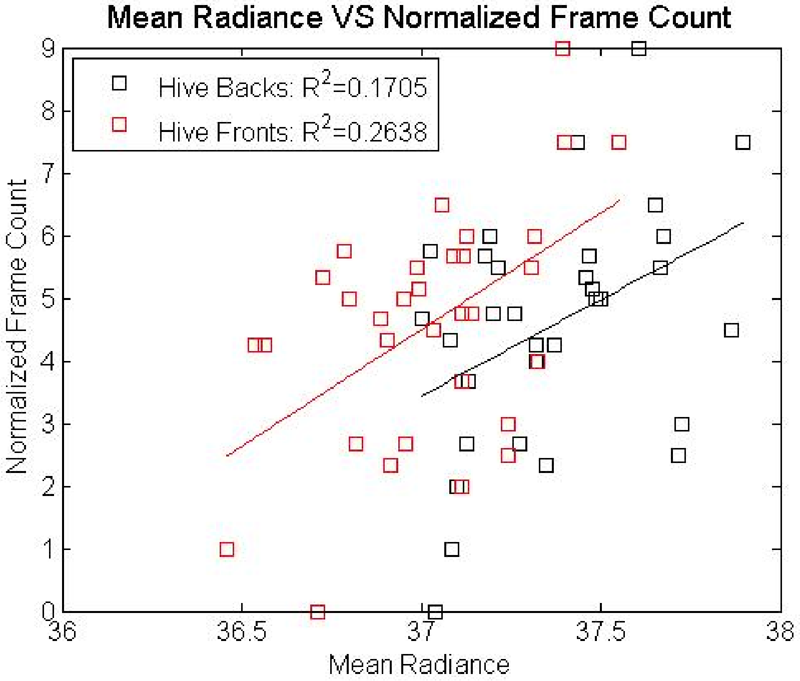

Figure 17. Normalized frame count plotted vs. mean radiance for 8/2/2010 PM

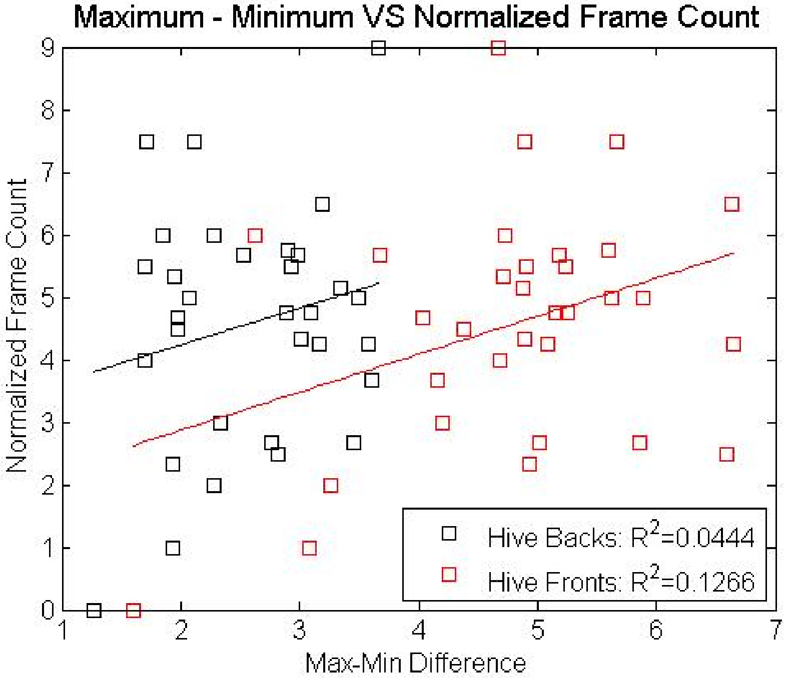

Figure 18. Normalized frame count plotted vs. difference between maximum and minimum radiance for 8/2/2010 PM

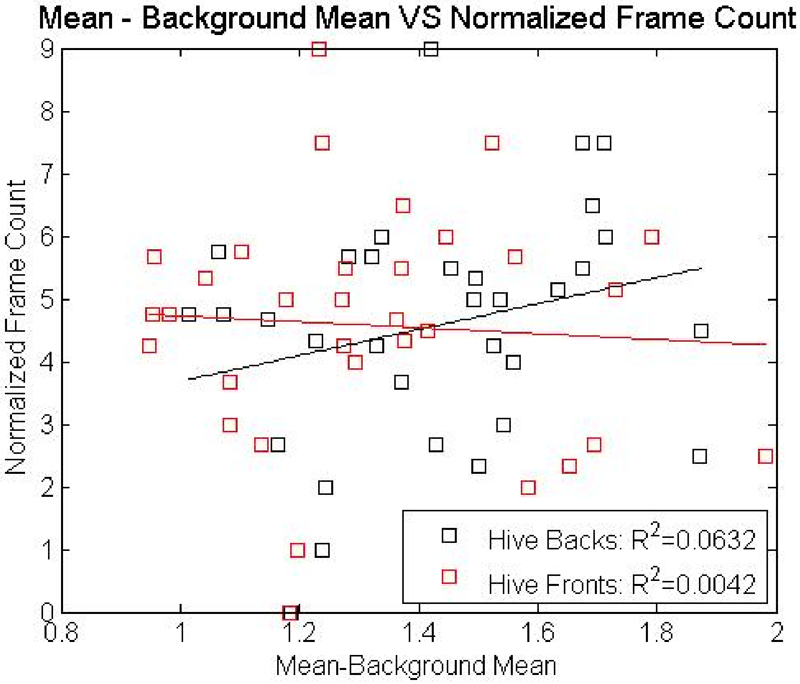

Figure 19. Normalized frame count plotted vs. difference between mean and background mean radiance for 8/2/2010 PM

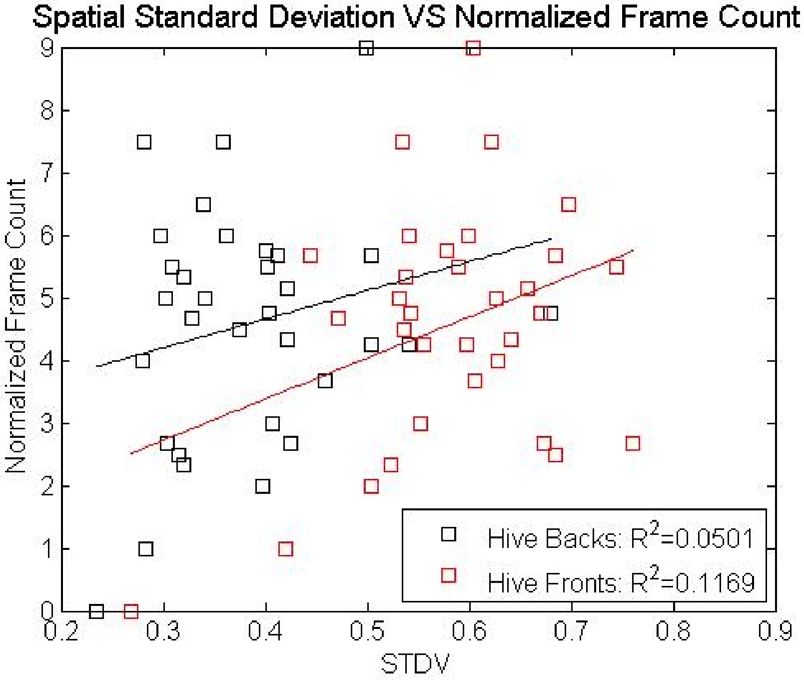

Figure 20. Normalized frame count plotted vs. special standard deviation in radiation for 8/2/2010 PM

Since the results from May 2010 showed that the morning data sets had stronger coefficients of determination than the evening sets, the remaining images acquired during this period were from the mornings. A second set of images were acquired the morning of August 3 starting at 5:50 AM. The local sunrise was at 6:19 AM, with the sun becoming visible approximately 20 minutes later. The temperature varied between 10.6 -11.1°C with the relative humidity staying constant at 85% and the pressure at 907 mb. The resulting radiance statistics are shown in Figures 21-24.

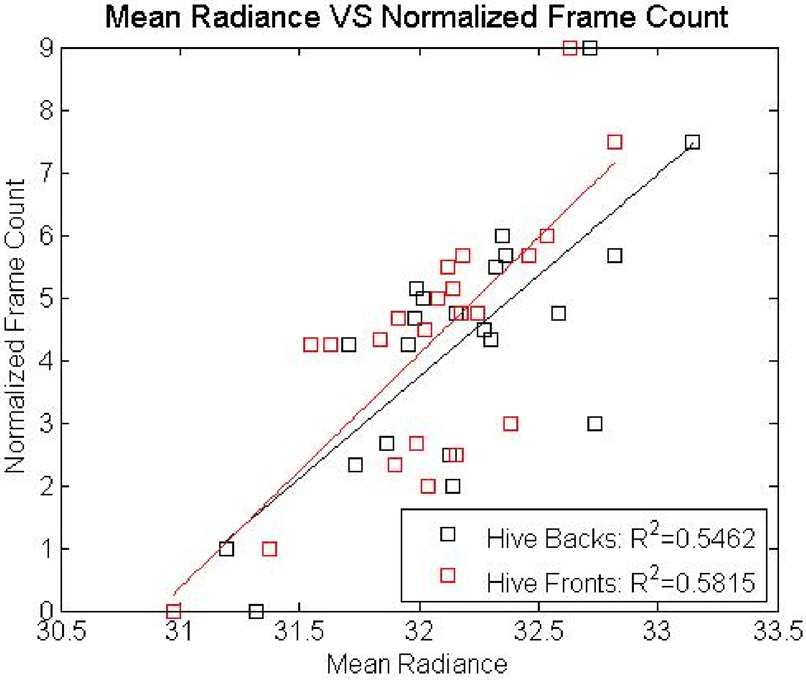

Figure 21. Normalized frame count plotted vs. mean radiance for 8/3/2010 AM

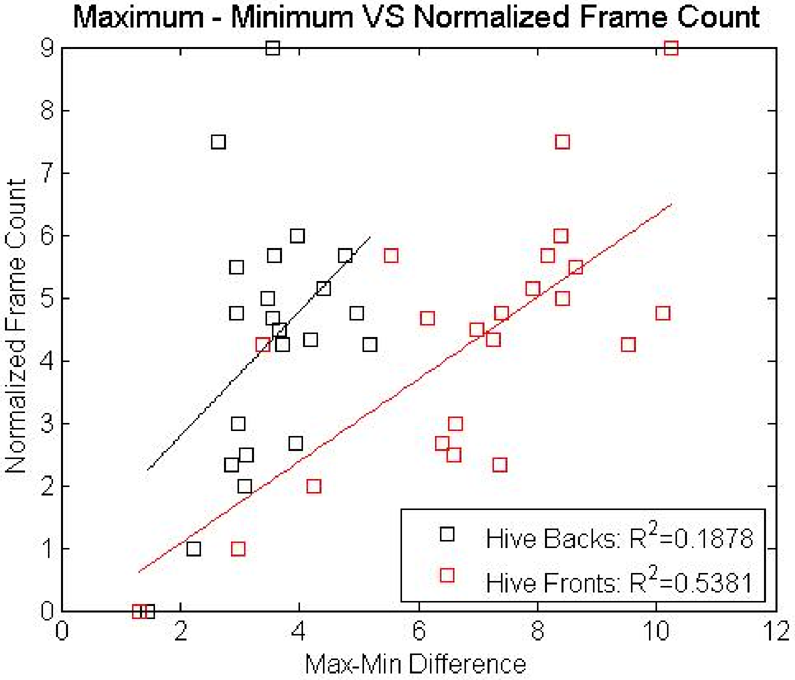

Figure 22. Normalized frame count plotted vs. difference between maximum and minimum radiance for 8/3/2010 AM

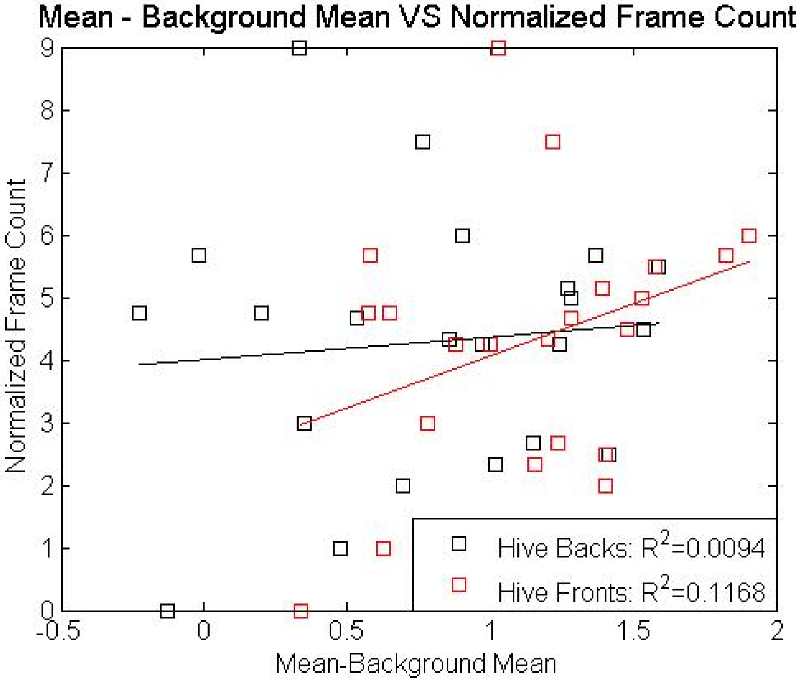

Figure 23. Normalized frame count plotted vs. difference between mean and background mean radiance for 8/3/2010 AM

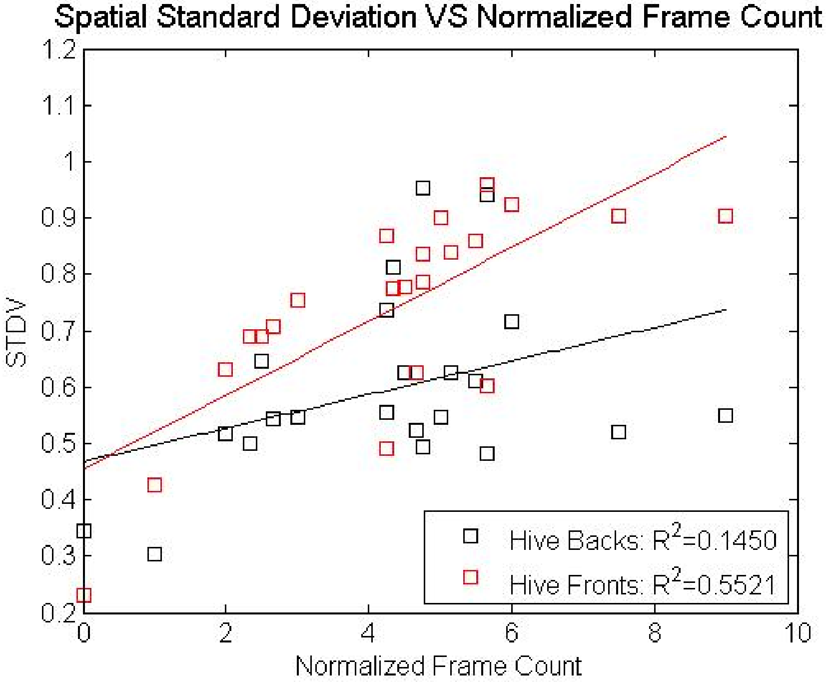

Figure 24. Normalized frame count plotted vs. special standard deviation in radiance for 8/3/2010 AM

A third set of images were acquired on the morning of August 4, starting at 5:40 AM. The local sunrise was at 6:20 AM, with the sun becoming visible approximately 20 minutes later. The temperature stayed constant at 17.8°C with a constant relative humidity of 58% and the pressure at 909 mb. The resulting radiance statistics are shown in Figures 25-28.

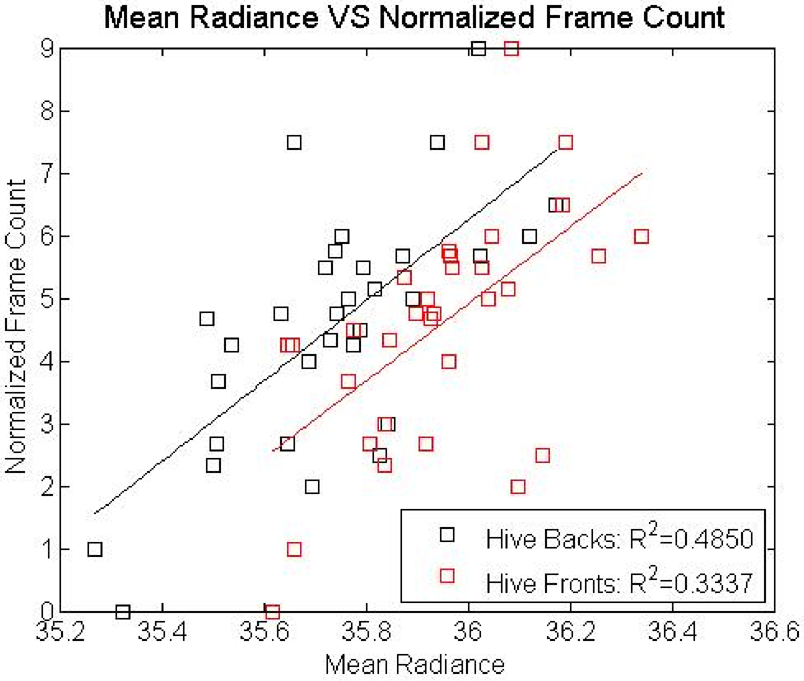

Figure 25. Normalized frame count plotted vs. mean radiance for 8/4/2010 AM

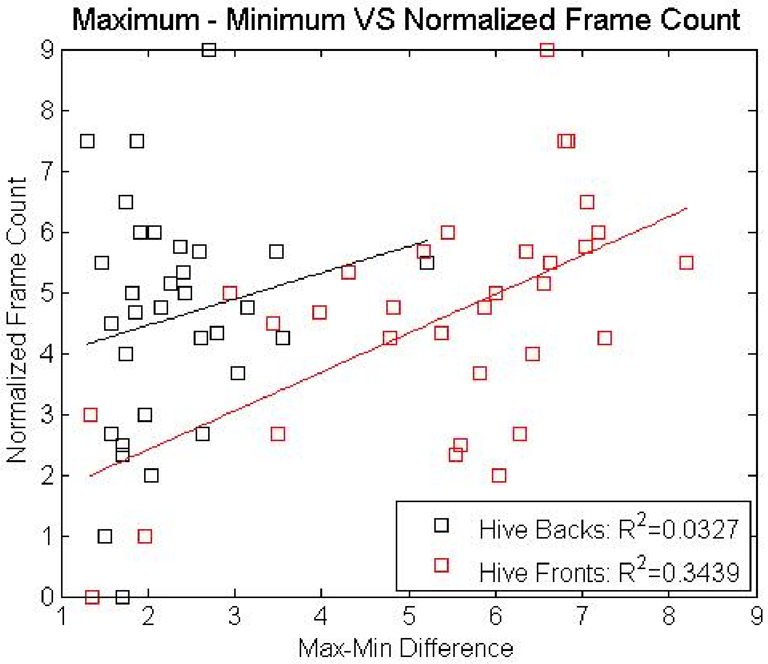

Figure 26. Normalized frame count plotted vs. difference between maximum and minimum radiance for 8/4/2010 AM

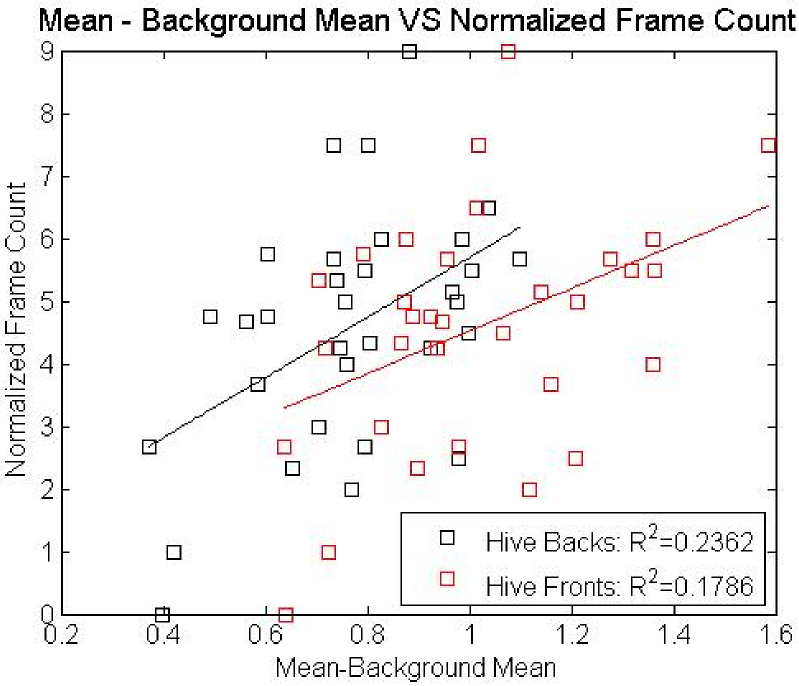

Figure 26. Normalized frame count plotted vs. difference between mean and background mean radiance for 8/4/2010 AM

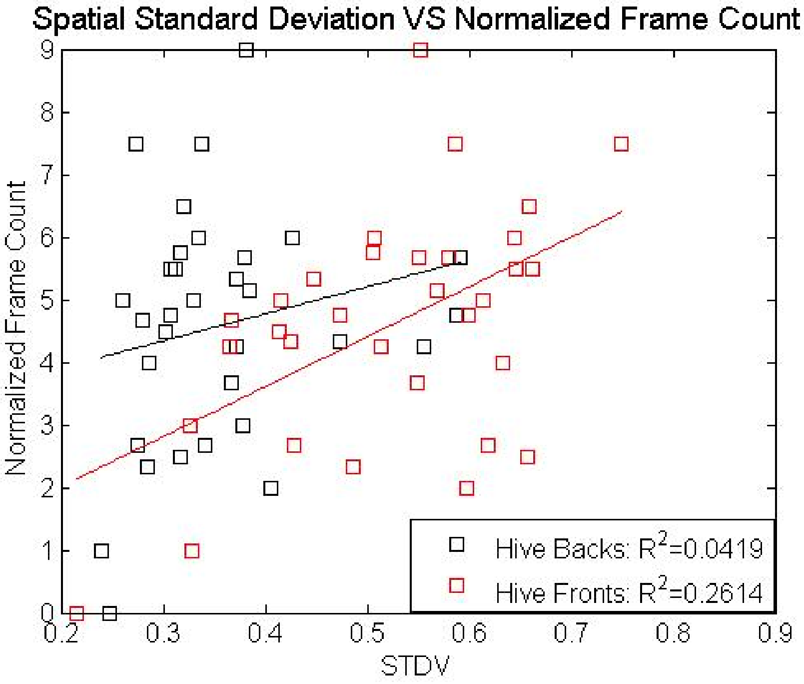

Figure 27. Normalized frame count plotted vs. special standard deviation in radiance for 8/4/2010 AM

A fourth set of images was acquired the morning of August 5 starting at 5:30 AM. The local sunrise was at 6:21 AM, with the sun becoming visible approximately 20 minutes later. The temperature stayed constant at 16.1°C, with a constant relative humidity of 60% and the pressure at 909 mb. The resulting radiance statistics are shown in Figures 29-32.

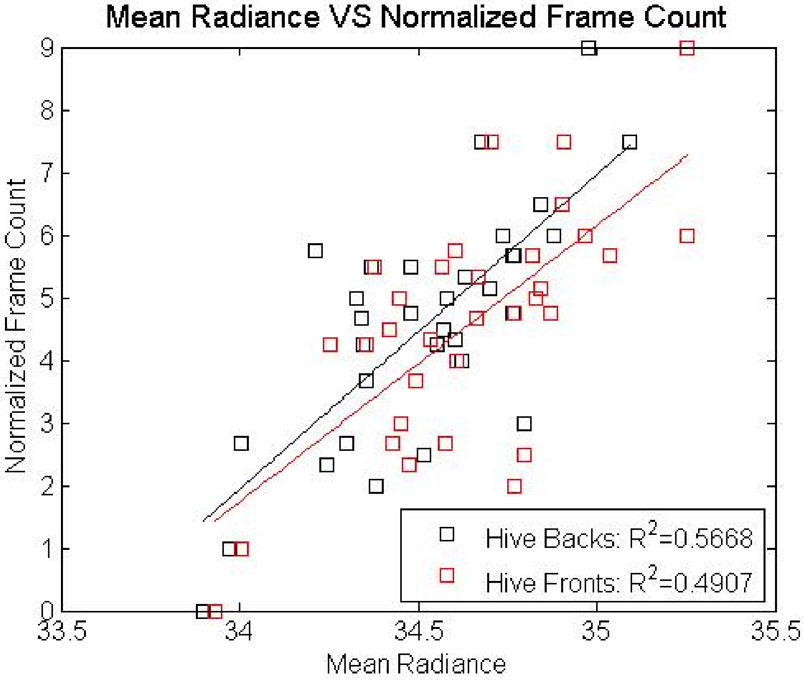

Figure 28. Normalized frame count plotted vs. mean radiance for 8/5/2010 AM

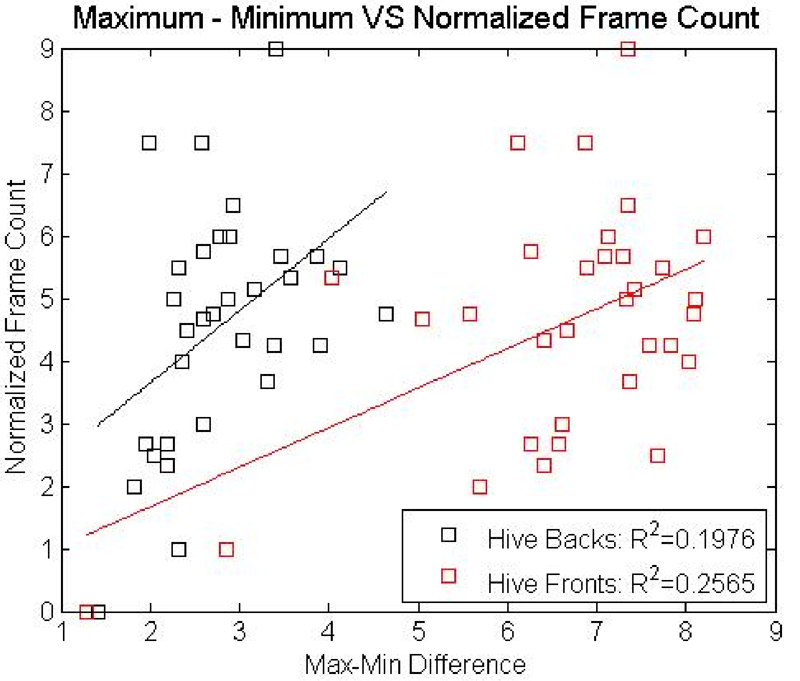

Figure 29. Normalized frame count plotted vs. difference between maximum and minimum radiance for 8/5/2010 AM

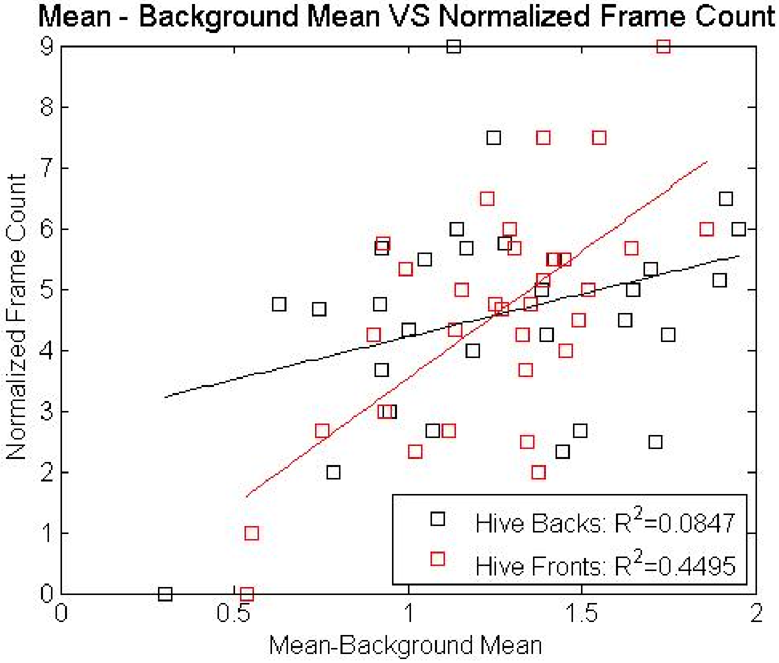

Figure 30. Normalized frame count plotted vs. difference between mean and background mean radiance for 8/5/2010 AM

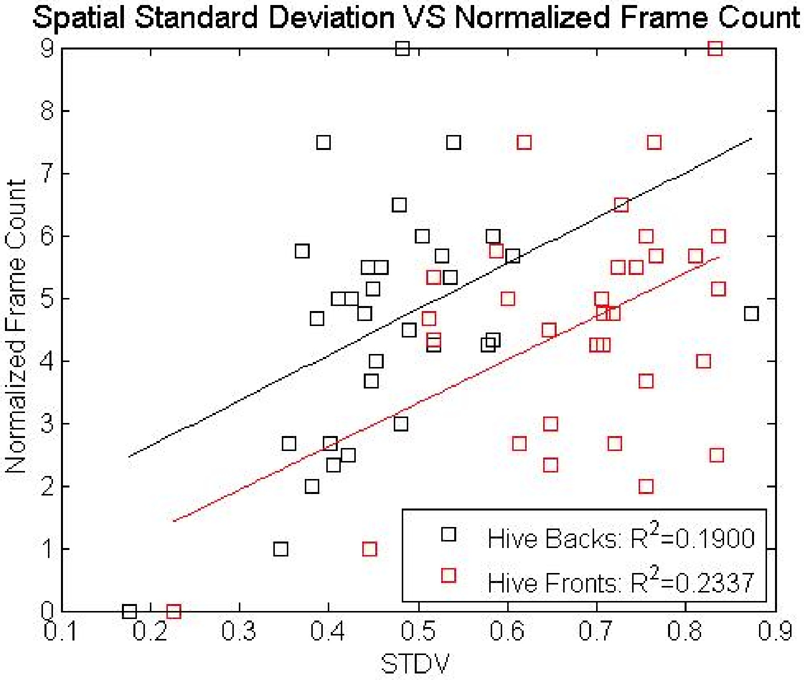

Figure 31. Normalized frame count plotted vs. special standard deviation in radiance for 8/5/2010 AM

These image sets show similar results, which are summarized in Table 4. As seen before, the morning sets generally had higher R^2 values than the evening set. The hive fronts had higher R^2 values than the hive backs for this imaging period. Overall, the mean radiance consistently gave a high R^2 value, while the difference between the maximum and minimum radiance plots, along with the difference between the mean and background mean radiance, also gave fairly good R^2 values. However, these values are significantly lower than those found in May, which could be a result of the time of year. In May the bees were leaving dormancy, while in August the bees were actively preparing for winter. At the approach of winter, the bees become increasingly inactive because they no longer need to secure pollen to produce honey to feed on over the winter. This lack of activity could result in a lower thermal signature since less heat from motion is produced. Additionally, it is known that honeybees form tight clusters as the ambient temperature drops in order to conserve heat (Stabetheiner et al. 2002). This clustering of the hive could be present at the onset of fall, meaning less heat would be escaping from the bees, resulting in a lower thermal signature. Nevertheless, despite the lower coefficients of determination, there was still evidence for a link between the thermal signature and the hive vitality.

Table 4. Summary of the R^2 values for the image sets from 8/2/2010 PM - 8/5/2010 AM.

	Hive Side	Mean	Maximum-Minimum	Mean-Background Mean	STDV
8/2/2010PM	Hive Backs	0.1705	0.0444	0.0632	0.0501
	Hive Fronts	0.2638	1.266	0.0042	0.1169
8/3/2010AM	Hive Backs	0.5462	0.1878	0.0094	0.145
	Hive Fronts	0.5815	0.5381	0.1168	0.5521
8/4/2010AM	Hive Backs	0.485	0.0327	0.2362	0.0419
	Hive Fronts	0.3337	0.3439	0.1786	0.2614
8/5/2010AM	Hive Backs	0.5668	0.1976	0.0847	0.19
	Hive Fronts	0.4907	0.2565	0.4495	0.2337

July 2011

The first sets of results from 2011 are for the evening of July 20, 2011. For this particular night, two sets of images were acquired, the first set starting at 10:00 PM and the second set starting at 11:25 PM. By taking two sets, it was possible to determine whether the hives were still showing the effects of solar heating approximately an hour after sundown. In the presence of such effects, a longer wait after sunset would be required. The local sundown on July 20, 2011 was 9:23 PM. The first images were collected between 10:00 and 10:30 during which the ambient temperature varied from 14.7° C to 16.2° C with the relative humidity remaining nearly constant at 49%. The sky was observed to be clear and only slight wind gusts up to 1.4m/s were measured. In order to include the effects of the variations in ambient temperature, the mean, minimum, and maximum radiance values were linearly scaled using infrared images acquired of the blackbody at the start and end of the imaging session. Figures showing the plotted radiance statistics for these images are shown in Appendix 2 as Figures 1-4. The plots all had very low R^2 values; however, these results still showed that the mean radiance and the spatial standard deviation plots yielded the best results, consistent with results from previous imaging periods.

The second set of images that same evening were collected between 11:25 and 11:50 PM, during which time the ambient temperature varied from 12.7 to 14.3° C, with the relative humidity remaining nearly constant at 61%. The sky was again observed to be clear and only slight wind gusts up to 1.0 m/s were measured. Figures showing the plotted radiance statistics for these images are shown in Appendix 2 as Figures 5-8. Again, these four plots all had very low R^2 values, although as before they showed better results from the spatial standard deviation plot and the difference between the mean and background mean radiance. The R^2 values from both evening sets are summarized in Table 5.

Table 5. Summary of the R^2 values for the two image sets from 7/20/2011 PM.

	Hive Side	**Mean**	**Maximum-Minimum**	**Mean-Background Mean**	**STDV**
Set 1	Hive Fronts	0.5223	0.3057	0.1879	0.3857
	Hive Backs	0.5547	0.2134	0.0397	0.3609
Set 2	Hive Fronts	0.1043	0.1822	0.3009	0.3588
	Hive Backs	0.3761	0.7028	0.3447	0.4860

The lack of improvement in R^2 values for the second measurements on the evening of July 20 means that waiting longer after sunset to take the images was unnecessary. One possible explanation for the thermal signatures being stronger closer to sunset is that the bees are more actively trying to heat the hive at that time. Immediately after sunset, the hive temperature may drop rapidly due to the cessation of solar heating, causing the bees to more actively produce heat as compensation.

A third set of images was acquired on the morning of July 21, 2011 between 5:20 AM and 5:40 AM. The local sunrise was at 6:03 AM but appeared slightly later due to the mountains to the east of Missoula. During the imaging, the ambient temperature varied from 6.0 to 7.7 ° C, with the relative humidity varying between 92.8% and 100%. The sky was observed to be clear and only slight wind gusts up to 0.7 m/s were measured. The hives were observed to have dew present on the metal tops. Figures showing the plotted radiance statistics for these images are shown in Appendix 2 as Figures 9-12. These radiance statistics are summarized in Table 6.

Table 6. Summary of R^2 values for the images from 7/21/2011 AM.

	Hive Side	Mean	Maximum-Minimum	Mean-Background Mean	STDV
7/21/2011 AM	Hive Backs	0.447	0.452	0.377	0.541
	Hive Fronts	0.7343	0.683	0.534	0.616

The R^2 values for the morning were significantly improved over those of the night images, as expected from previous results. Again, the fronts had slightly stronger R^2 values than the backs.

August 2011

Images also were acquired on the night of August 24, 2011. Imaging started at 10:40 PM, with the local sunset occurring at 8:30 PM. The temperature was measured to range from 15.8 – 16.9 °C, with the relative humidity ranging from 70.2%-79%. The wind speed was measured to gust up to 0.4 m/s. Figures showing the plotted radiance statistics for these images are shown in Appendix 2 as Figures 13-16. The results were very similar to those found in August of 2010.

A second set of images were acquired on the morning of August 25, 2011. Imaging started at 5:50 AM and the local sunrise was at 6:47 AM. The temperature was measured to vary from 17.4 – 18.1 °C, with the relative humidity varying between 59.8-62%. The wind speed gusted up to 0.4 m/s. A rain test was simulated over the previous night where a sprinkler was used to wet half the hives from 11:16 PM until 5:46 AM. A total of three tables containing seventeen hives were affected by the sprinkler. Figures showing the plotted radiance statistics for these images are shown in Appendix 2 as Figures 17-20.

A third set of images was acquired on the evening of August 25, 2011. Imaging started at 10:20 PM and the local sunset was at 8:29 PM. The temperature was measured to vary from 15.7 – 18.8 °C, with the relative humidity varying between 64.4-67.7%. Figures showing the plotted radiance statistics for these images are shown in Appendix 2 as Figures 21-24.

A fourth set of images was acquired on the morning of August 26, 2011. Imaging started at 6:20 AM and the local sunrise was at 6:48 AM. The temperature was measured to stay constant at 10.6 °C, with the relative humidity constant at 100%. No wind gusts were observed during the imaging. Figures showing the plotted radiance statistics for these images are shown in Appendix 2 as Figures 25-28. The radiance statistics from these three days are summarized in Table 7.

Table 7. Summary of the R^2 values for image sets from 8/24/2011 PM - 8/26/2011 AM.

	Hive Side	**Mean**	**Maximum-Minimum**	**Mean-Background Mean**	**STDV**
8/24/211PM	Hive Backs	0.159	.0392	0.1368	0.0502
	Hive Fronts	0.0469	0.1143	0.0197	0.0046
8/25/2011 AM	Hive Backs	0.0126	0.3043	0.0679	0.2963
	Hive Fronts	0.0489	0.2947	0.2235	0.3032
8/25/2011 PM	Hive Backs	0.1612	0.0197	0.1005	0.0047
	Hive Fronts	0.0816	0.0742	1.40E-04	4.01E-6
8/26/211AM	Hive Backs	0.3534	0.1298	0.1922	0.1602
	Hive Fronts	0.1976	0.0882	0.0103	0.0049

Overall, the R^2 values for the August 2011 images were very weak for both night and morning image sets. For the night sets, the mean radiance was usually the strongest, while for the morning sets there was no clear strongest statistic. Comparison with the results of August 2010 shows the August 2011 data to again had weak R^2 values. It is worth noticing that the simulated rain did not appear to have any considerable effect on the hive thermal signatures. This suggests that this technique of measuring hive vitality may still be valid during periods of precipitation.

September 2011

Next, images were acquired on the night of September 21, 2011. Imaging started at 9:15 PM, with the local sunset occurring at 7:22 PM. The temperature was measured to range from 7.5 – 11.1 °C, with the relative humidity ranging from 70.2-99.1%. No wind was observed during the imaging. Figures showing the plotted radiance statistics for these images are shown in Appendix 2 as Figures 29-32.

A second set of images was acquired on the morning of September 22, 2011. Imaging started at 6:10 AM, with the local sunset occurring at 7:23 PM. The temperature was measured to range from 1.1 – 4.8 °C, with the relative humidity ranging from 95-100%. The wind was measured to gust up to 0.4 m/s. Figures showing the plotted radiance statistics for these images are shown in Appendix 2 as Figures 33-36.

Table 8. Summary of the R^2 values for the image sets from 9/21/2011 PM - 9/22/2011 AM.

	Hive Side	**Mean**	**Maximum-Minimum**	**Mean-Background Mean**	**STDV**
9/21/2011 PM	Hive Backs	0.1503	0.0376	0.0209	0.1842
	Hive Fronts	0.1367	0.0202	0.0663	0.0218
9/22/2011AM	Hive Backs	0.3909	0.3217	0.1439	0.2781
	Hive Fronts	0.3060	0.0911	0.1615	0.0758

Data from both September 21 and 22, 2011, showed low R^2 values, although slightly improved from the August 2011 results. The hive fronts had stronger R^2 values in both the mean radiance plots and difference between the mean and background radiance plots. The hive backs had high R^2 values for the mean radiance plots.

Conclusions

Mid-wave infrared detector cameras have been used in the past to image beehives for biological studies (Kastberger et al. 2003). The use of a long-wave infrared imager is a novel continuation of this idea. This method of determining hive vitality depends on following the proper imaging procedure outlined in the methodology section. It is important to allow the camera to stabilize before imaging, as well as to note the atmospheric conditions. Initial thermal images acquired in 2007 and 2008, where the camera was not allowed to stabilize, showed noticeable drift with no clear trends in the statistical data. Calibrations performed in a thermal chamber at Montana State University were used to determine the minimum warm-up time needed for the imager to properly stabilize. Recording the atmospheric conditions, particularly the ambient air temperature, accounted for changes in ambient conditions that could cause corresponding changes in hive radiance.

The results of imaging on multiple occasions over two years showed that there was a meaningful statistical relationship between the thermal signatures of beehives and their normalized frame counts, although there was high variation from experiment to experiment. Images acquired in the morning generally had larger R^2 values than images acquired in the evening. The cooler morning temperatures just prior to sunrise allowed for greater contrast between the hives and the image background. Daytime imaging was found to not be a viable technique because the solar heating obliterated the hive thermal signatures. However, daytime imaging within a shed or trailer appeared to yield useable thermal signatures. Further work will be needed to determine the range of acceptable imaging conditions. In the 2010 data, the mean radiance plots and the difference between the mean and background mean radiance generally had larger R^2 values. The 2011 data had generally small R^2 values, with the mean radiance generally yielding a better fit than the other parameters. It was also shown that rain has no significant impact on the hive thermal signatures, which was a concern in initial image sets acquired in 2008-2009. Future work will consist of showing this method to be valid inside bee sheds. Most commercial bee keepers enclose their hives in sheds during the winter months while they are dormant. Showing that a long-wave infrared imager could also be used inside would prove invaluable to bee keepers with large numbers of hives.

References

Kastberger, Gerald and Reinhold Stachl. "Infrared Imaging Technology and Biological Applications." *Behavioral Research Methods, Instruments, & Computers* 35.3 (2003) : 429-439.

Shaw, Joseph A., Paul W. Nugent, Jennifer Johnson, Jerry J. Bromenshenk, Colin B. Henderson, and Scott Debnam. "Long-wave Infrared Imaging for Non-invasive Beehive Population Assessment." *Optics Express* 19.1 (2011) : 399-408.

Stabentheiner, Anton, Helga Pressl, Thomas Papst, Norbert Hrassnigg, and Karl Crailsheim. "Endothermic Heat Production in Honeybee Winter Clusters." *The Journal of Experimental Biology* 206.2 (2003) : 353-358.

INFRARED IMAGING OF VEGETATION TO DETECT CO_2 LEAKS

The purpose of this chapter is to show the use of a calibrated, microbolometer-based, long-wave infrared camera in a second novel application, which is to detect a CO_2 gas leak in a controlled gas release experiment. Rather than detecting the leaking gas directly, this experiment was designed to use thermal imaging for indirectly detecting gas leaking from underground through changes in the infrared emission of overlying vegetation. The basis of this measurement is that plant canopy temperature has been shown to be a reliable indicator of plant water stress and ecosystem health (Alchanatis et al. 2010 and Moran 2004). When vegetation is stressed from lack of water or other factors, the plants lose their ability to self regulate their internal temperature. This results from a reduction in transpiration that causes the leaf temperatures to rise (Jackson et al. 1981).

From this basis, several research groups have begun using thermal infrared emission to monitor plant health. Several vegetation indices were developed to use ambient temperature differences in conjunction with canopy temperature differences. One such model is the Crop Water Stress Index (CWSI) shown in Equation 1 (Moran 2004).

$$CWSI = \frac{[(T_c - T_a)_m - (T_c - T_a)_r]}{[(T_c - T_a)_m - (T_c - T_a)_x]} \qquad [1]$$

The values T_c and T_a are the vegetation canopy and ambient air temperatures, respectively. The subscripts x, m, and r refer to the maximum, minimum, and measured temperature values, respectively. This index has been found to give reasonable approximations of vegetation health from airborne and space-borne infrared imagers (Menentu et al. 2008 and Torrion 2008). However, practical implementation of this method typically requires the user to know or estimate multiple parameters, such as the plant roughness length for momentum transfer, the sensible heat flux conducted to the soil, the ambient psychrometric constant, and the minimum canopy resistance. The Optical Remote Sensor Lab has been searching for a simpler, more direct method of using thermal images to detect plant stress resulting from elevated CO_2 ground concentrations. This search was carried out during experiments in the summers of 2009-2011 during controlled CO_2 gas release experiments.

From the summer of 2007 through the summer of 2011, the Zero Emission Research and Technology (ZERT) center has simulated a CO_2 leak from an underground horizontal well, buried in a research field in Bozeman, Montana. The test site is a hay field belonging to the agriculture department at Montana State University. The vegetation present in the field consists mostly of alfalfa, clover, dandelions, thistles, and variety of grasses (Spangler et al. 2010).

Layout of Release Mechanisms

Initially, a vertical pipe was placed in the soil at a nominal depth of 2.5 m (Strazisar et al. 2009). CO_2 was injected into it over ten days at a rate of 800 standard mL/min in order to simulate a point source leak (Stazisar et al. 2009). Next, a horizontal well was installed 45° east of true north at a depth of 1.8 m. This orientation allowed for the resolution of vector components perpendicular to the well of potential CO_2 transport in the groundwater and the wind (Spangler et al. 2010). The well casing consisted of a 98 m stainless steel pipe with a slotted central length allowing for an open area of 0.55%

(Spangler et al. 2010). The well itself was partitioned into six zones using a packer system. This allowed the CO_2 to be more evenly distributed along the pipe length. Figures 33 and 34 show aerial views of the ZERT site with the CO_2 release mechanisms drawn in.

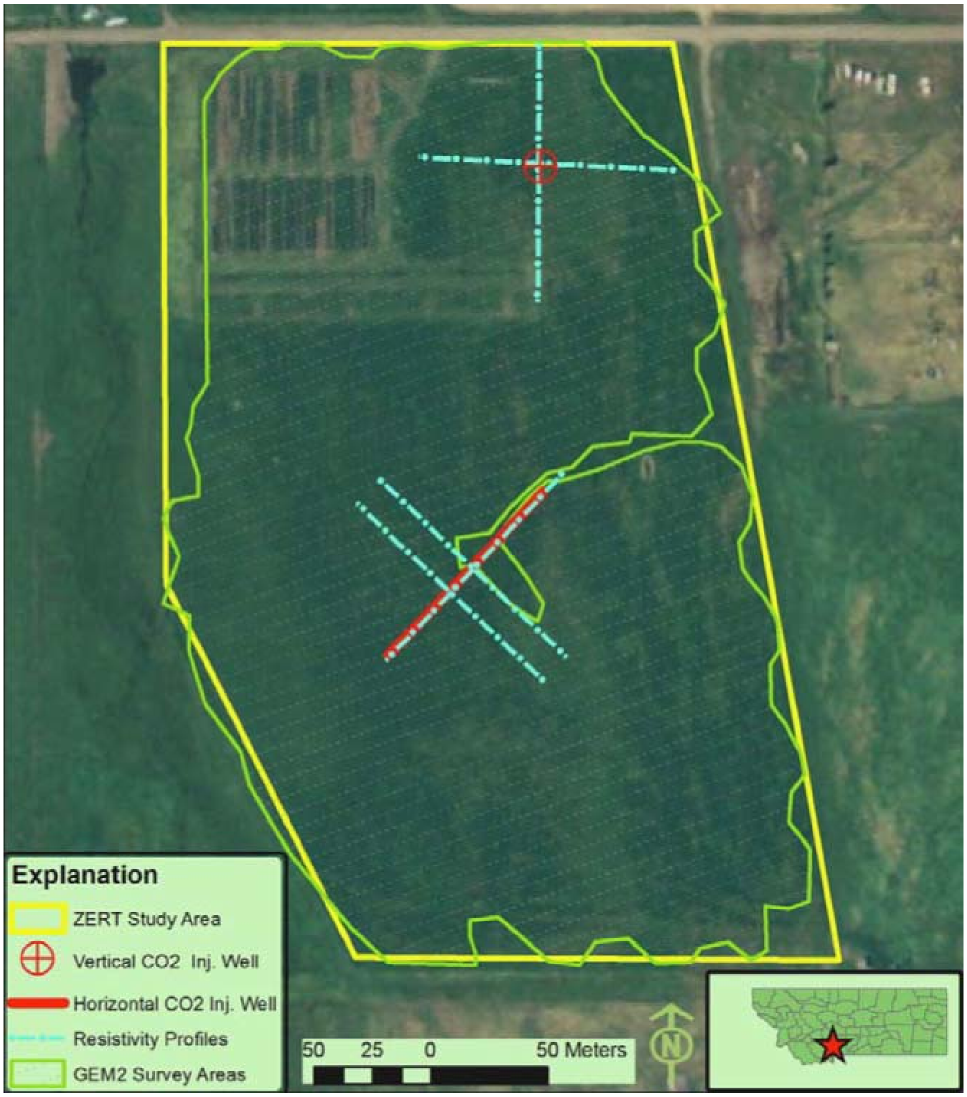

Figure 32. ZERT field map showing the two injection wells (Strazisar et al. 2009)

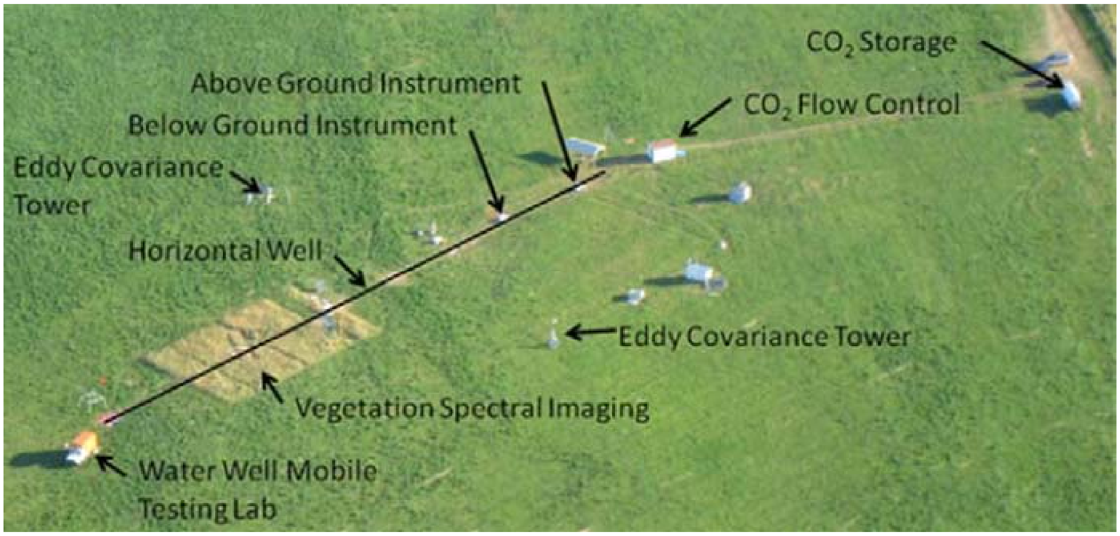

Figure 33. Aerial view of the ZERT CO2 release facility (Barr et al. 2011)

Various flow rates and additives were tried in the five years of CO_2 releases. These release statistics are summarized in Table 9.

Table 9. Summary of ZERT release periods

Release Date	Flow Rate (ton/day)	Additional Comments
July 9-18, 2007	0.1	6.5 mL perfluorinated tracer injected into zone 4 for 48 hrs
August 3-10, 2007	0.3	Equal flux in all six zones
July 9-August 7, 2008	0.3	16.5 mL perfluorinated tracer injected into zone 4 for 132 hrs
August 27-Sept. 9, 2008	0.05	Injected into zone 3 only
July 15-August 12, 2009	0.2	Equal flux in all six zones
June 3-June 24, 2010	0.2	Early-season release in zones 1-3
July 19-August 15, 2010	0.15	Equal flux in all six zones
July 15-August 15, 2011	0.15	Equal flux in all six zones

Methodology

For the infrared images, a FLIR photon 320 infrared camera was mounted to scaffolding at the ZERT site. The scaffolding was located at the south-east edge of the vegetation spectral imaging patch shown in Figure 34 and was offset approximately three meters from the horizontal well. The camera was located at the top of the 3-m scaffolding and imaged the vegetation below at a 45° angle with the well running horizontally through the images. The vegetation patch was a 400-m^2 area separated from the rest of the field. During the 2009 release, half of the vegetation patch was mown in order to compare it to the un-mown vegetation. The patch was left un-mowed in both 2010 and 2011. Figure 35 shows the camera mounted on the scaffolding while Figure 36 shows the vegetation patch from the camera's position.

Figure 34. Scaffolding housing the infrared thermal imager (the round tube shaped camera). (J.A.Shaw 2010)

Figure 35. The camera's view from the top of the scaffolding (J.A.Shaw 2010)

The camera was pointed to see a vegetation region extending from the outer edge of the vegetation test area to near a hot spot above the horizontal well. The hot spot was a point where particularly high CO_2 flux was observed during each year's release experiment. This ensured that the images showed the gradual CO_2 effects without showing the immediate death of the vegetation directly over the leak. For the 2009 release, imaging started June 25th and ended August 30th, with images being acquired every 10 minutes of each day. For the 2010 release, imaging started on July 12th and ended on August 28th, with images being acquired every five minutes. For the 2011 release, imaging started June 17th and ended August 22nd, with images being acquired every minute. In all three cases, imaging began before the start of the actual CO_2 release in order to get a base reading for unaffected vegetation. Before the 2010 and 2011 releases, it was noticed that a difference in vegetation could be observed between the healthy vegetation and affected vegetation, presumably from previous releases.

Image Processing

Once images were acquired, they were calibrated using custom MATLAB software. Each image was then run through a MATLAB routine which selects user-defined regions of interest. Images acquired in the 2009 and 2010 releases selected two regions of interest: a control region and a hot spot region. Figure 37 shows sample regions of interest for the 2009 and 2010 releases.

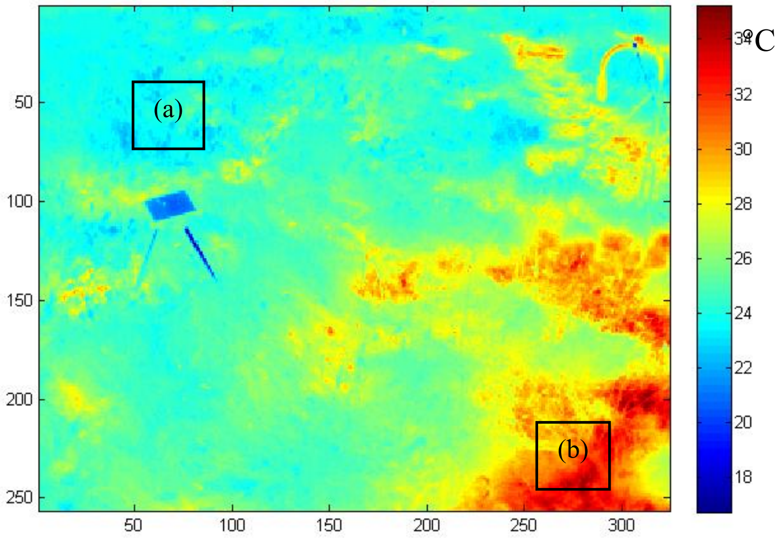

Figure 36. Thermal image for 7/26/2010 at 13:20 PM showing analysis regions: (a) control region and (b) hot spot region.

For the 2011 release, three regions of interest were chosen: a horizontal control region, a vertical control region, and a hot spot region. Figure 38 shows sample regions of interest for the 2011release.

Figure 37. Thermal image for 7/13/2011 at 23:59 PM, showing analysis regions: (a) vertical control region, (b) horizontal control region, and (c) hot spot region.

Two control regions were used to evaluate the effects of imaging the scene at different angles. After the selection process, the MATLAB script returned the temperature values of the three regions for each image. For the three releases, the following values were determined for each day: the maximum and minimum differences between each region temperature and the ambient air temperature, the maximum and minimum temperature differences between the horizontal control region and the hot spot region, and the maximum and minimum temperature difference between the vertical control region and the hot spot region. These values were plotted over the duration of the release for each summer.

Results

2009 Results

A clear diurnal pattern was observed each day as the vegetation heated up during the day and cooled down at night. This pattern is shown in Figures 39, 40, and 41, representing the start, the middle, and the end of the release, respectively.

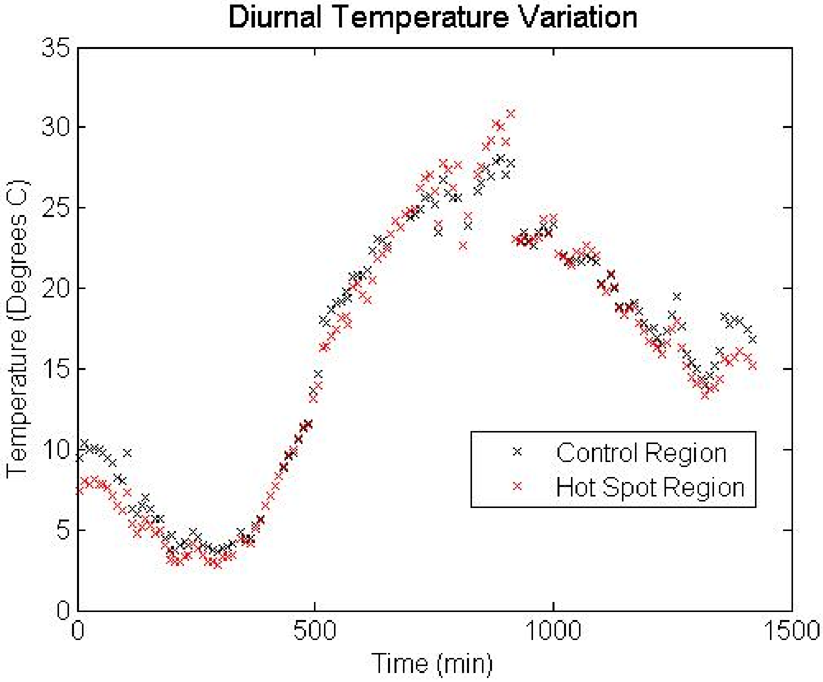

Figure 38. Diurnal variation of vegetation brightness temperature for July 11, 2009.

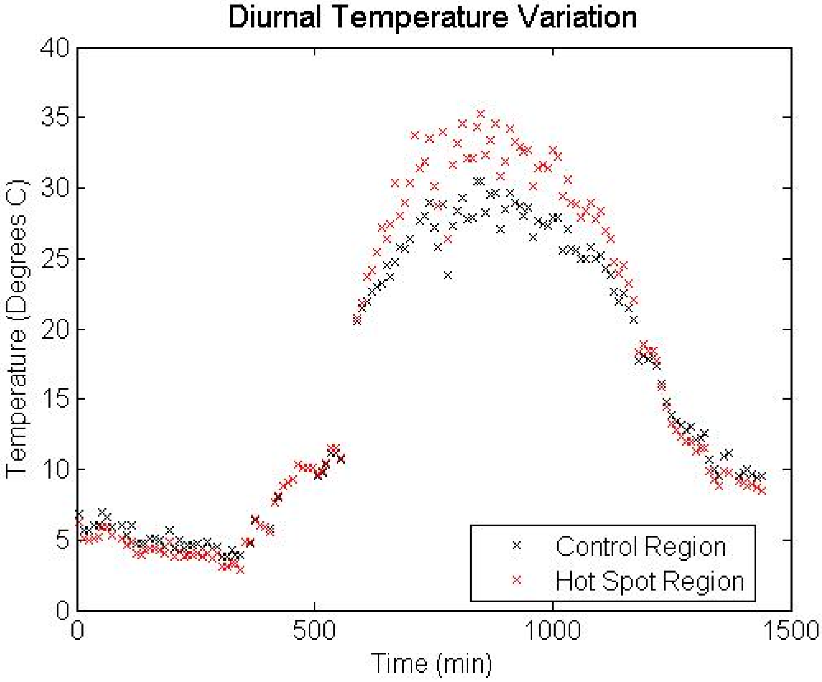

Figure 39. Diurnal variation of vegetation brightness temperature for August 1, 2009.

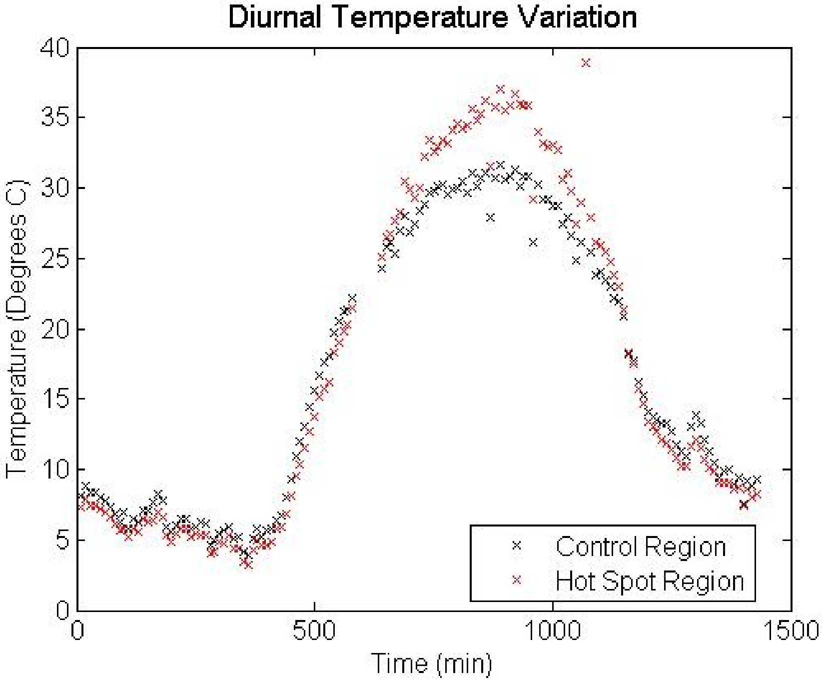

Figure 40. Diurnal variation of vegetation brightness temperature for August 26, 2009.

The diurnal results show a general separation between the control region and the hot spot region as the CO_2 appears to cause the vegetation to die off near the hot spot. This trend is consistent with that seen in saturated vegetation roots that are unable to thermally regulate their temperature as effectively during the heat of the day like the healthy vegetation can. These diurnal trends follow the daily temperature profiles closely, which accounts for the difference between the starting and ending diurnal temperatures for each day. The clear change in diurnal trends over the 2009 release showed that using thermal imaging had the potential to detect regions with elevated CO_2 levels.

2010 Results

As with the 2009 data, a clear diurnal thermal regulation pattern was again observed each day. This pattern is shown in Figures 42 and 43, representing the start and the middle of the release, respectively.

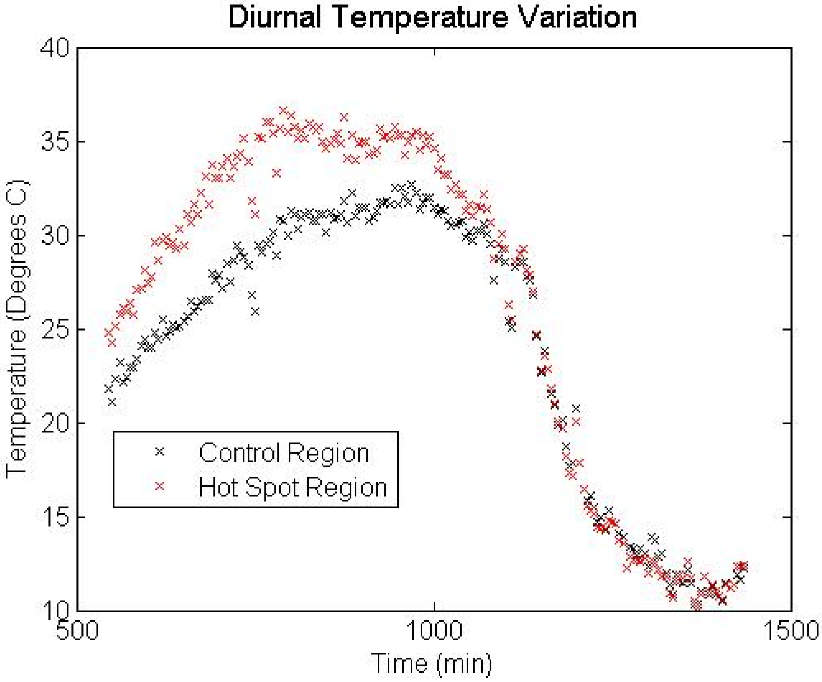

Figure 41. Diurnal trends for July 18, 2010

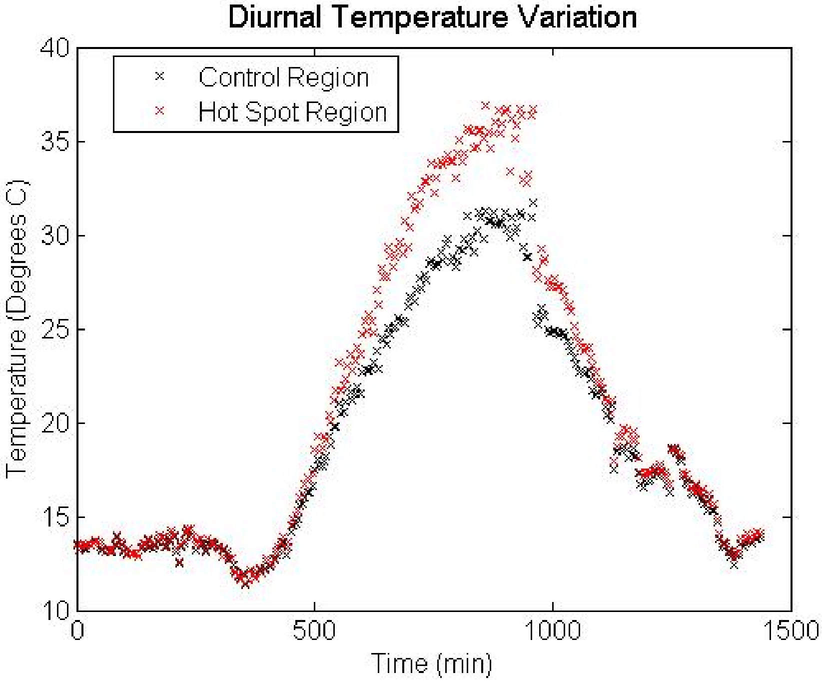

Figure 42. Diurnal trends for August 5, 2010

The diurnal trend at the start of the 2010 summer showed a slight residual effect on the vegetation near the hot spot from an early-season release conducted in June. Later in the release, the hot spot region showed a more noticeable divergence from the control region as expected, especially in the later portion of the day. Only one control region was selected in each image for the 2010 release. Figures 44 – 47 show the overall summer 2010 results.

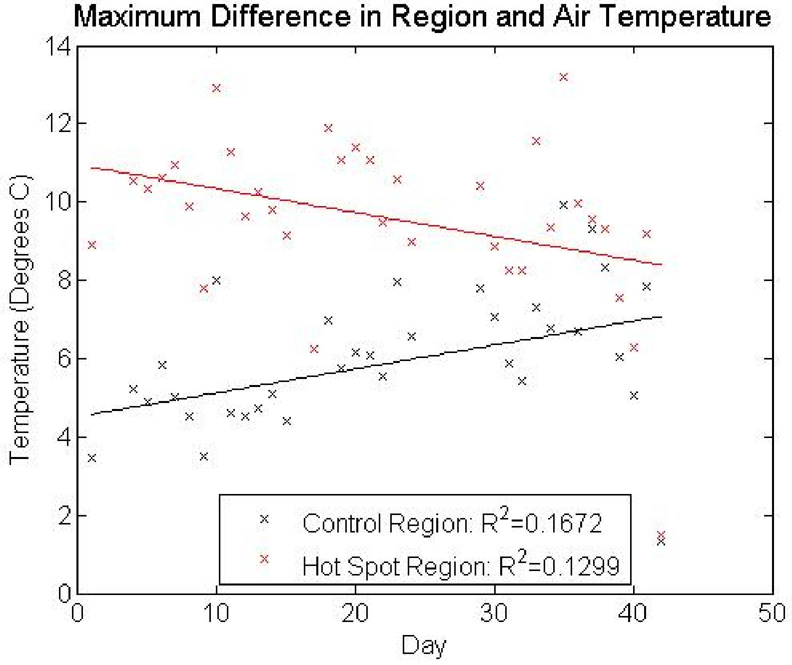

Figure 43. Maximum difference between region temperatures and ambient air temperature vs day

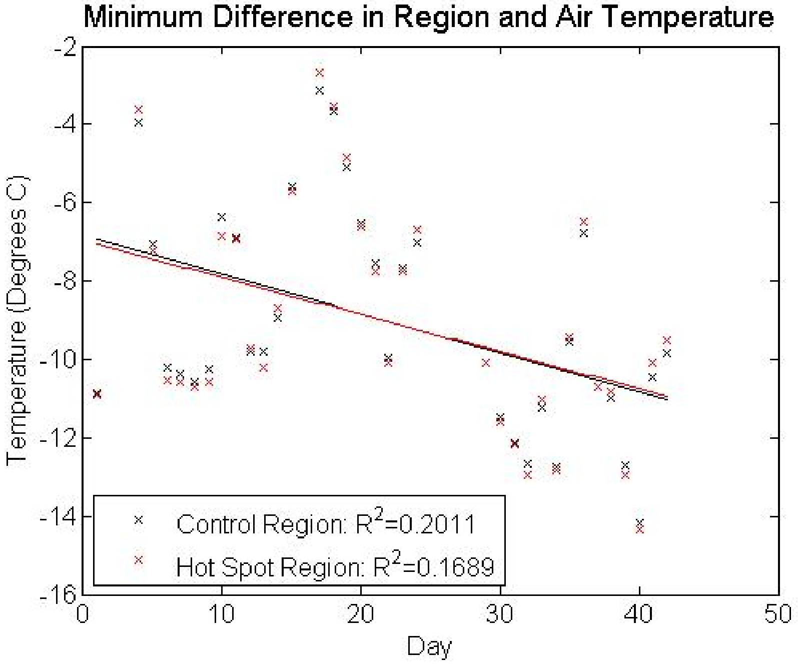

Figure 44. Minimum difference between region temperatures and ambient air temperature vs day

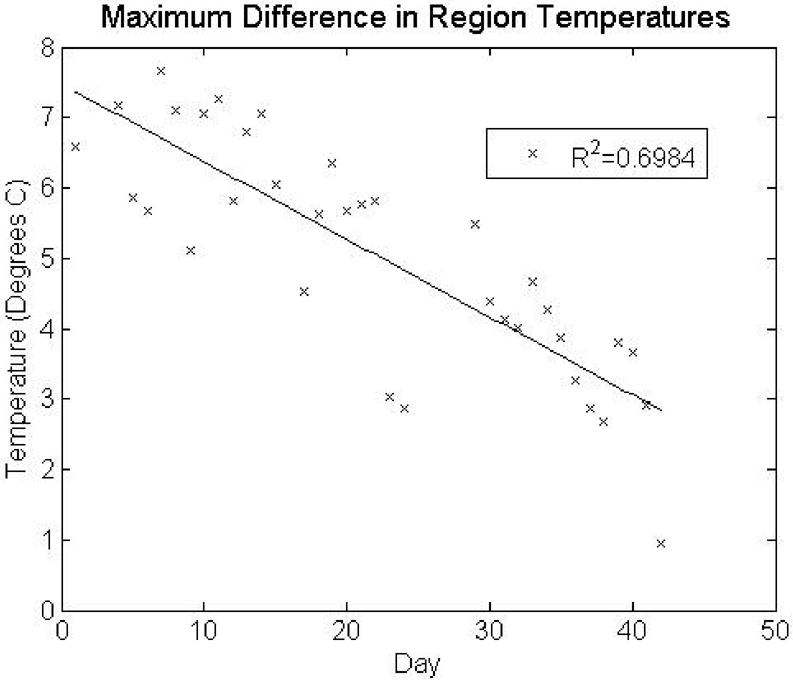

Figure 45. Maximum difference between the control region and the hot spot region vs day

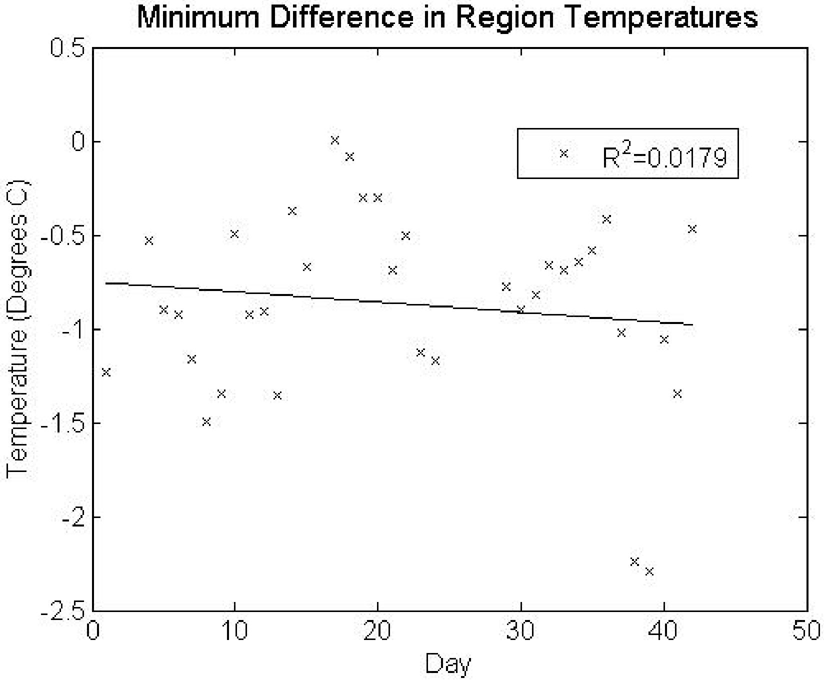

Figure 46. Minimum difference between the control region and the hot spot region vs day

These regressions from the 2010 data yielded fairly low R^2 values, with the minimum air temperature difference plot and the minimum region temperature difference plot showing the smallest values. Since the nights during the summer were generally warm, the plants did not need to thermo regulate as much to keep warm. This caused the vegetation to have very small temperature differences from the ambient air and between the regions of interest. The plot of the maximum difference between each region and the ambient air temperature showed the greatest difference between the control region and the hot spot region. Over the release, the healthy vegetation appeared to thermo regulate well, causing it to have a much different temperature than the ambient air (cooler than the hot daytime air, and warmer than the cool nighttime air). The difference in thermo regulation could also be a result of other causes, such as high water content in the vegetation which would result in an increase in thermal inertia. As it dies off naturally due to the hot summer weather, it becomes more similar to the ambient air temperature. The vegetation exposed to the CO_2 starts out weaker than the healthy vegetation, meaning it has a smaller variation from the ambient air due to weakened temperature regulation. By the end of the release, it has completely died off and become extremely dry, meaning it absorbs and loses heat well. This yields the increasing difference between its temperature and the ambient air temperature. Figure 46 also shows a clear difference between the two regions. At the start of the release the healthy vegetation has a much different temperature from that of the hot spot, which died off quite rapidly throughout the release from the CO_2. At the end of the release, the two regions became much more similar as the healthy vegetation had begun to die off naturally, meaning both regions were possibly no longer thermo regulating. A second method was used where the maximum temperature difference values were chosen from between the hours of 10 AM and 2 PM. When the temperatures were higher, the vegetation was more actively regulating its temperature, meaning a clearer difference between the control region and the hot spot region should be evident. These results are shown in Figures 48 and 49.

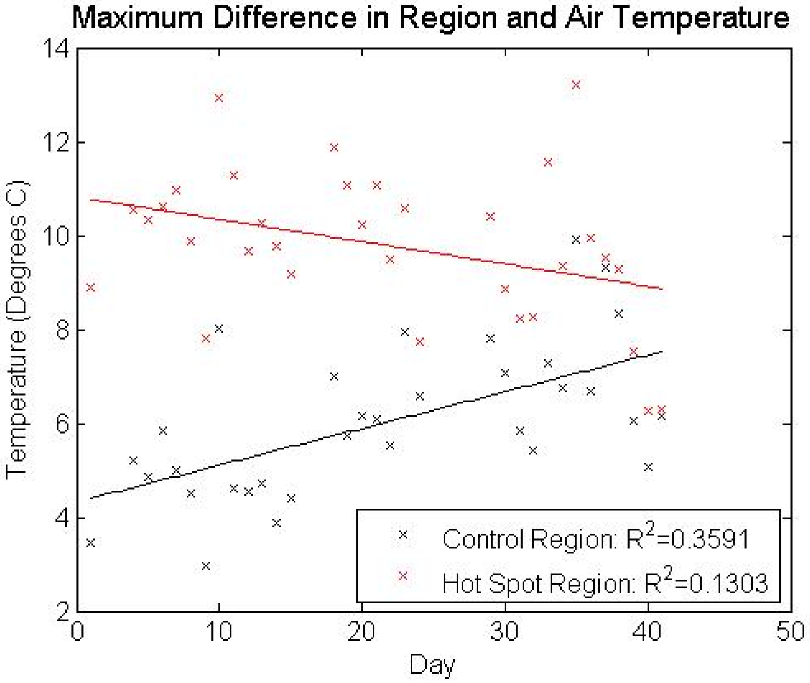

Figure 47. Maximum difference between region temperatures and ambient air temperature vs day for 10AM-2PM

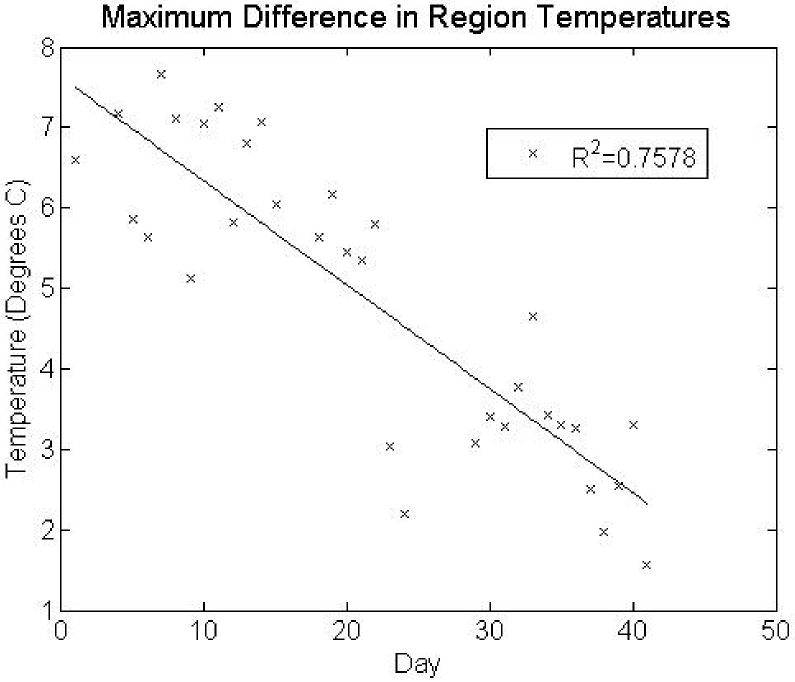

Figure 48. Maximum difference between the control region and the hot spot region vs day for 10AM-2PM

Restricting analysis to measurements acquired between 10 AM and 2 PM improved the R^2 values on both plots by removing the thermal outliers. The maximum difference between the control region and the hot spot consistently showed the highest R^2 values of all the plots, suggesting that this method could be of use in detecting a CO_2 leak. This method would be implemented by looking for regions having elevated thermal signatures, particularly around midday, with respect to the surrounding vegetation. Multiple images of the region should show the warmer vegetation, indicating the potential presence of a CO_2 leak. This would then be confirmed using a ground-based CO_2 detection system.

2011 Results

In 2011 we drew on lessons learned in the prior release years, and deployed the long-wave infrared camera earlier in the season, and with a more reliable calibration. As with the previous data, a clear diurnal thermal regulation pattern was observed each day during the 2011 release. This pattern is shown in Figures 50 and 51, representing the start and the end of the release, respectively.

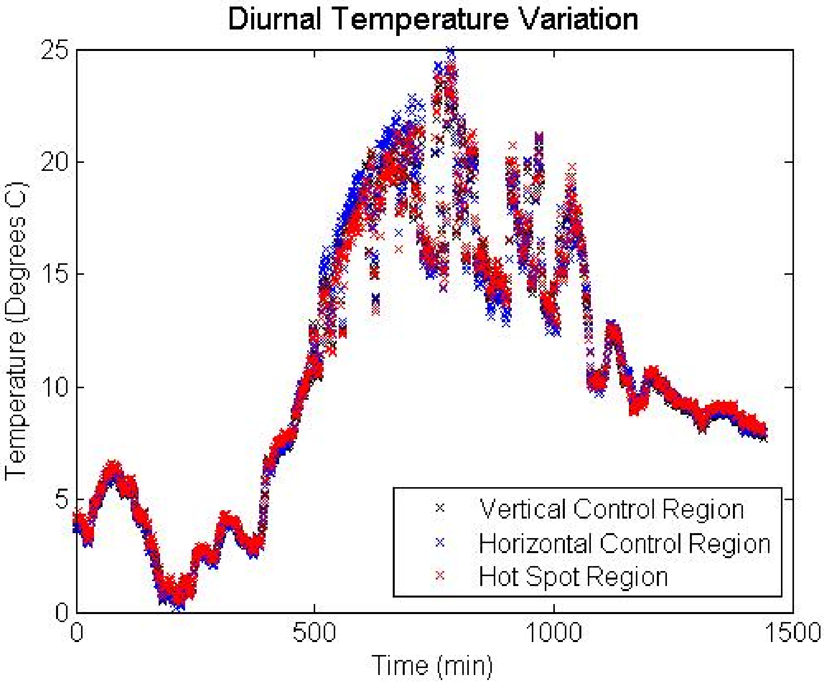

Figure 49. Diurnal trends for June 18, 2011

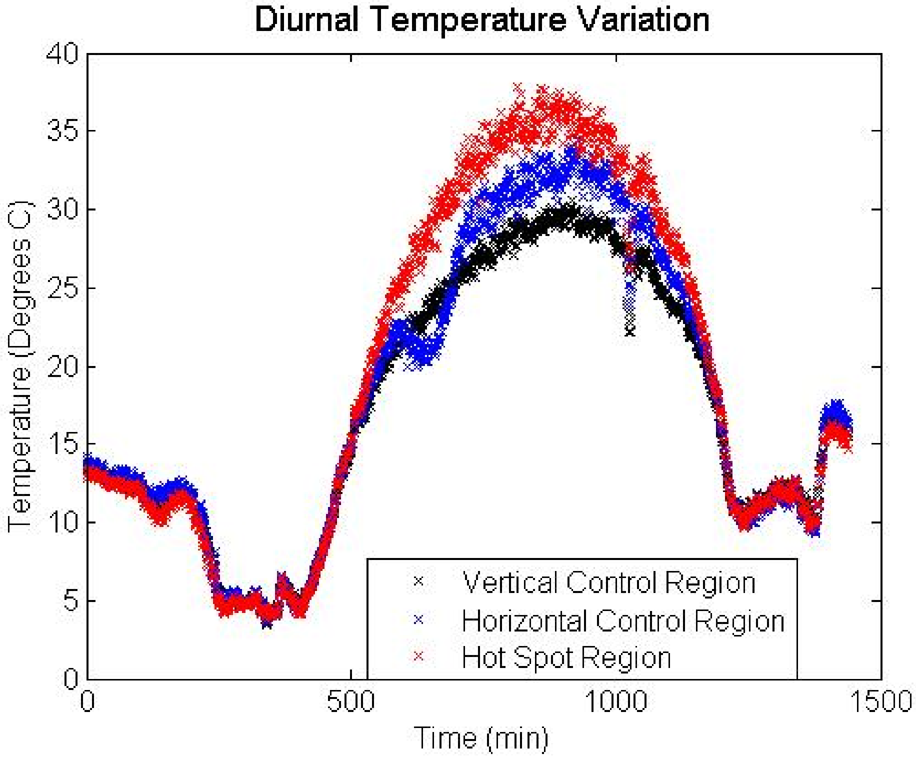

Figure 50. Diurnal trends for August 20, 2011

These two figures showed a clear separation in vegetation behavior between the start and end of the release. It was noticeable that the thermal signatures of both control regions were similar, which is an important result because it suggests that view-angle bias is not a strong concern. The dips in the diurnal temperature variations can be explained by examining the weather data for those days. The dip observed around 1020 minute mark in Figure 51 is due to a cloud passing over the vegetation patch causing a shadow over all three regions of interest, which results in a lower temperature. Similarly the numerous fluctuations of the vegetation region temperatures seen in Figure 50 correspond to temperature changes caused by clouds repeatedly crossing the ZERT field. A notable factor about the 2011 collected data was that the thermal imager was started 28 days before the start of the release. This allowed the initial conditions of the vegetation to be well documented, meaning any changes in behavior were more noticeable. Figures 52 – 55 show the overall summer 2011 results.

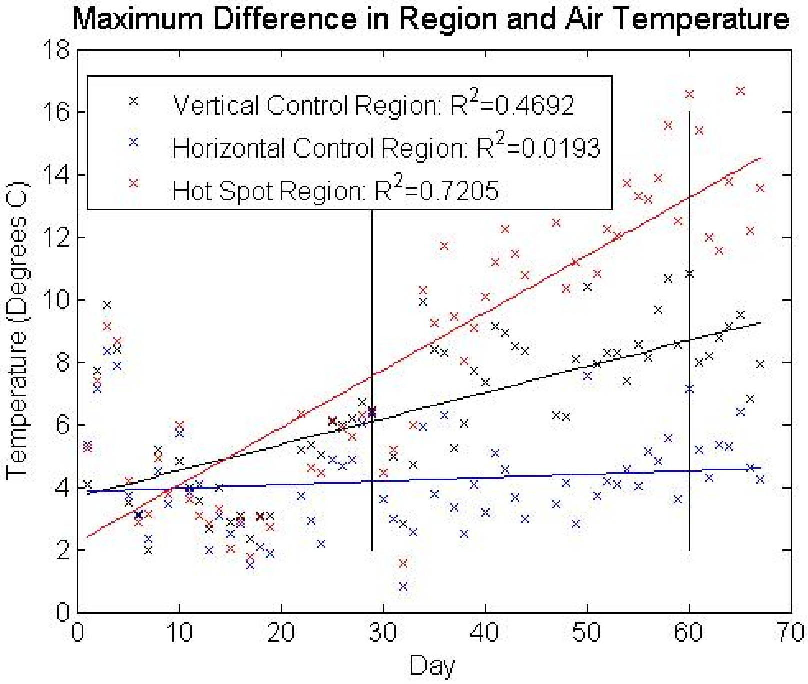

Figure 51. Maximum difference between region temperatures and ambient air temperature vs day for the 2011 release.

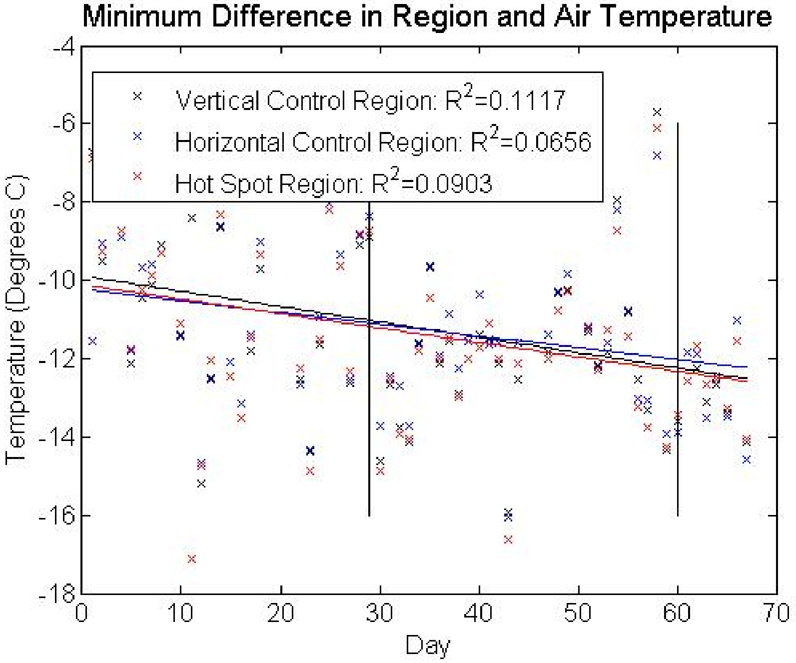

Figure 52. Minimum difference between region temperatures and ambient air temperature vs day for the 2011 release.

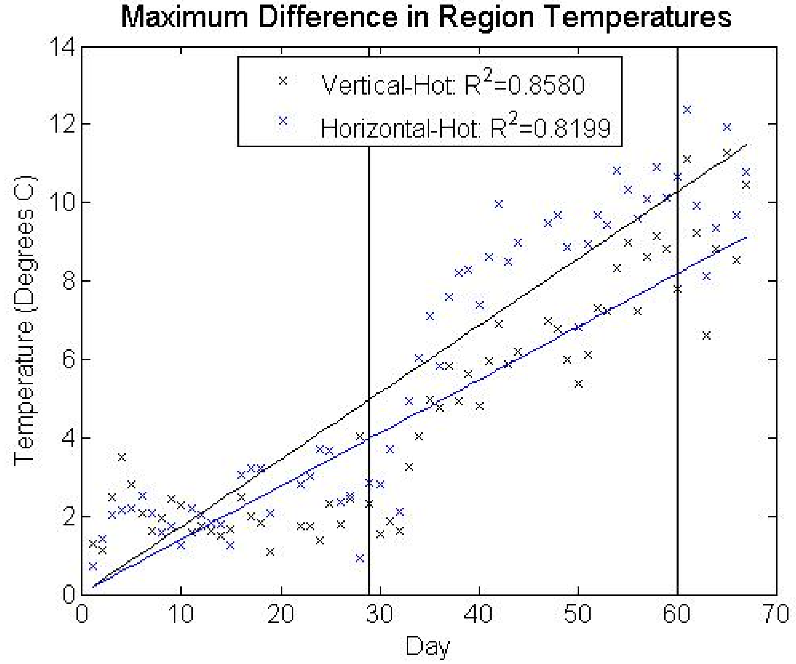

Figure 53. Maximum difference between the control region and the hot spot region vs day for the 2011 release.

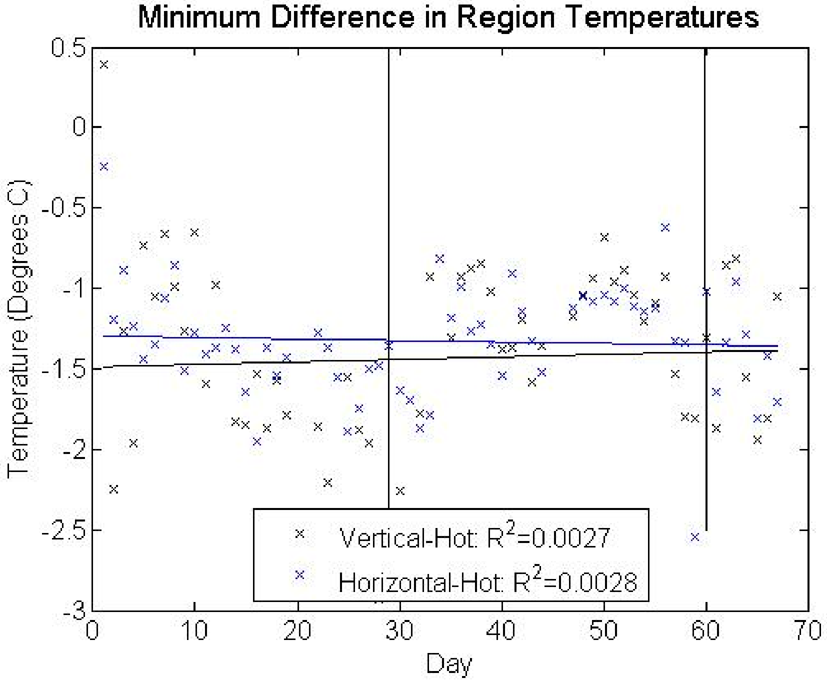

Figure 54. Minimum difference between the control region and the hot spot region vs day for the 2011 release.

As before, the plots showing minimum temperature difference had the lowest R^2 values, while the plot showing the maximum temperature difference between each control region and the hot spot region had the highest. Figure 54 was also of interest because it clearly showed the start of the release. The differences between the control regions and the hot spot regions were small until almost immediately after the start of the CO_2 release. The differences continued to grow as the hot spot vegetation rapidly died off until the end of the release. The difference tended to level off at the end as any remaining vegetation in the hot spot region was no longer being killed by the CO_2. Figures 56-57 show the maximum temperature difference plots with data acquired from 10AM-2PM again.

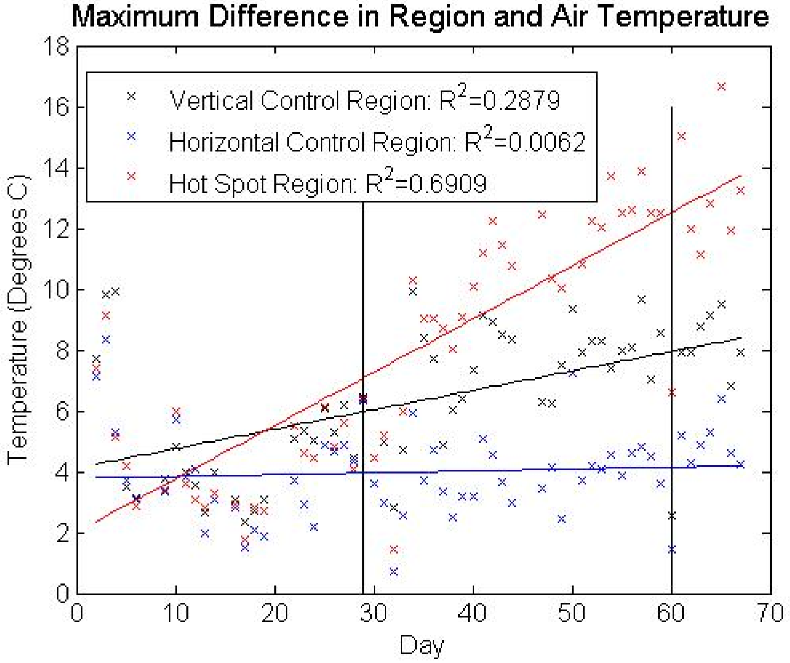

Figure 55. Maximum difference between region temperatures and ambient air temperature vs day for 10AM-2PM

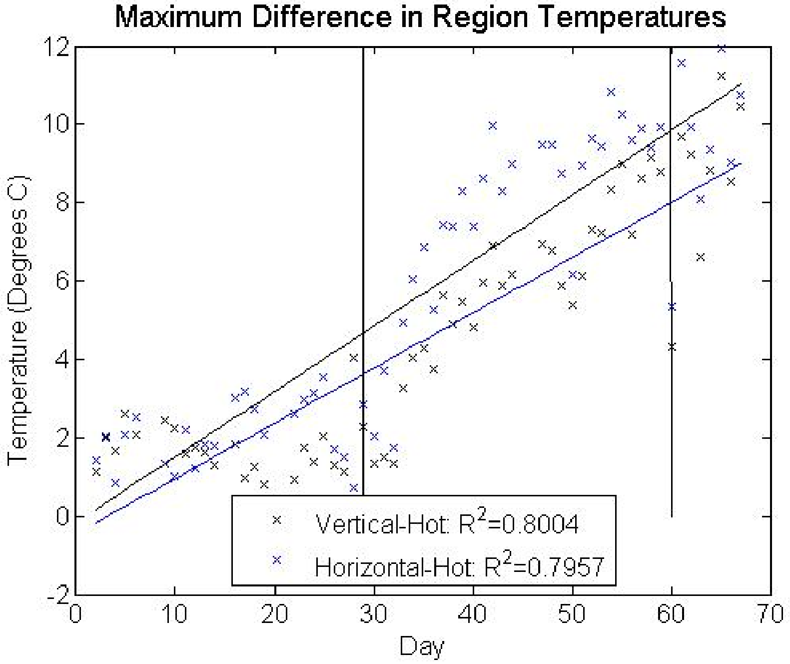

Figure 56. Minimum difference between region temperatures and ambient air temperature vs day for 10AM-2PM

For the 2011 data, limiting the thermal infrared data to between 10AM and 2 PM did not strengthen the R^2 values. This was likely a result of having a data set that started well before the release start that caused the data to be non-linear at the start and end of the release. A third method was implemented where the difference between the region temperatures and the ambient air temperature at 1:00 PM was plotted versus day. This is shown in Figure 58.

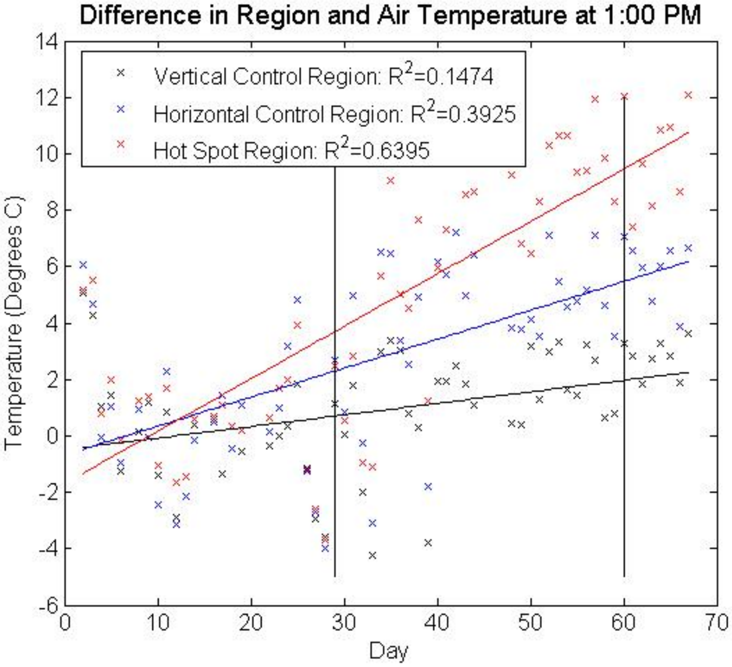

Figure 57. Difference between region temperatures and ambient air temperature vs day at 1 PM.

This resulted in higher R^2 values for the horizontal control region while slightly reducing the R^2 values of the hot spot region. However, the hot spot continued to have a fairly high R^2 value, making it an effective predictor of a CO_2 leak. The advantage of using this method was that only one image a day needed to be acquired instead of continuous daily images. An imager could be mounted in an aircraft or other aerial vehicle to monitor the site instead of requiring a scaffold. This would make it ideal for monitoring sites such as gas pipelines for which a stationary imager is undesirable. A fourth method was used that compared the difference in the region temperatures at 3:00 AM and 1:00 PM. These results are shown in Figure 59.

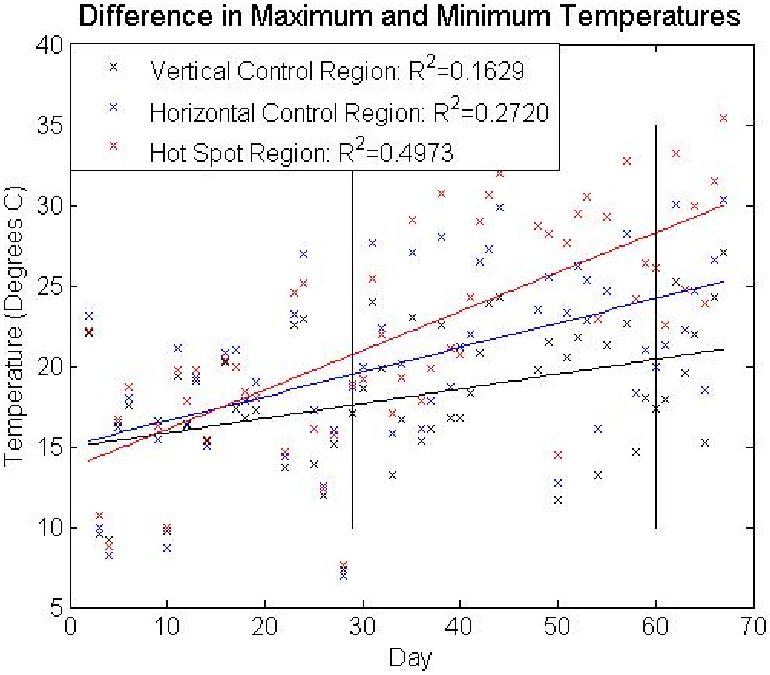

Figure 58. Difference between the temperature measured at 3AM and the temperature measured at 1PM.

This resulted in much lower R^2 values in both the hot spot region and the horizontal control region while again slightly improving the vertical control region’s R^2 values. In general, the 2011 regressions yielded lower R^2 values because of the images collected outside of the release dates, during which time the vegetation brightness temperature was changing approximately linearly, but the 2011 data present a strong case that thermal imagery can effectively identify the location of an underground gas leak. The benefit to using the full data set is that the start of the release is clearly visible in the plotted data.

Conclusions

Overall, the FLIR photon infrared imager was able to show changes in vegetation radiance consistent with the effects of elevated ground levels of CO_2. The affected vegetation began to react to the CO_2 almost immediately after the release began and deviated from the control regions in a statistically manner. This could be seen visually in the collected thermal images. For example, Figure 60 shows thermal images from before and after the release.

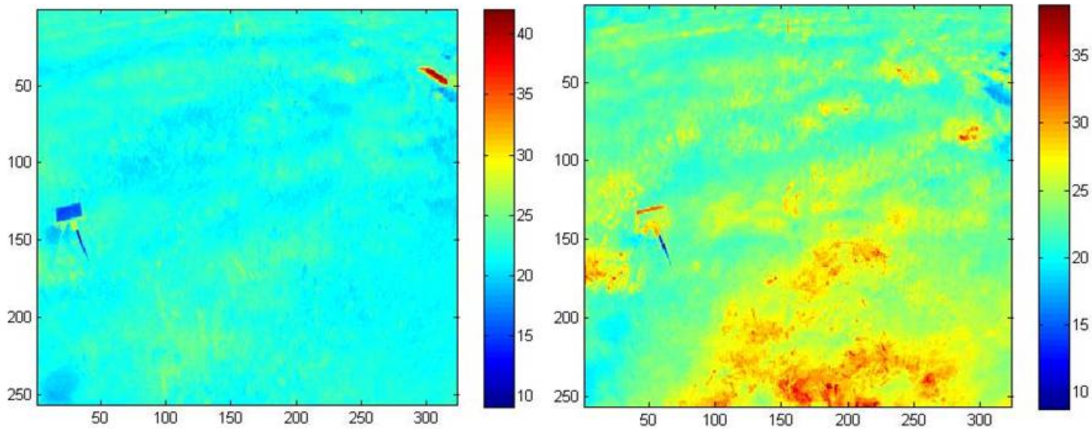

Figure 59. Thermal images (°C) for 7/13/2011 at 10:00 AM (left) and 8/10/2011 acquired at 10:00 AM (right).

The exposed vegetation at the lower right clearly had a different thermal signature than the control regions farther from the CO_2 (lower left and upper left). The 2010 and 2011 data, in particular the 2011 data, yielded fairly high R^2 values for regressions of the maximum temperature at each control region and the hot spot region. An additional benefit to this imaging method was that the change in thermal signature of the exposed vegetation appeared on the thermal images much sooner than it could be seen by eye, meaning an unwanted leak would potentially be spotted much sooner.

References

Alchanatis, V., Y. Cohen, S. Cohen, M. Moller, M. Sprinstin, M. Meron, J. Tsipris, Y. Saranga, and E. Sela. “Evaluation of Different Approaches for Estimating and Mapping Crop Water Status in Cotton with Thermal Imaging.” *Precision Agriculture* 11.1 (2010) : 27-41.

Barr, Jamie L., Seth D. Humphries, Amin R. Nehrir, Kevin S. Repasky, Laura M. Dobeck, John L. Carlsten, and Lee H. Spangler. “Laser-based Carbon Dioxide Monitoring Instrument Testing During a 30-day Controlled Underground Carbon Release Field Experiment.” *International Journal of Greenhouse Gas Control* 5.1 (2011) : 138-145.

Jackson, R. D., S. B. Idso, R. J. Reginato, and P. J. Pinter Jr. :Canopy Temperature as a Crop Water Stress Indicator.” *Water Resources Research* 17.4 (1981) : 1133-1138.

Menenti, Massimo, Li Jia, and Zhao-Liang Li. “Multi-angular Thermal Infrared Observations of Terrestrial Vegetation.” *Advances in Land Remote Sensing: System, Modelling, Inversion, and Application* 1. (2008) : 51-93.

Moran, M. S. “Thermal Infared Measurements as an Indicator of Plant Ecosystem Health.” in *Thermal Remote Sensing in Land Surface Processes*, D. A. Quattrochi and J. C. Luvall (Ed) London: Taylor and Francis, 2004. Pp. 257-282.

Spangler, Lee H. et al. “A Shallow Subsurface Controlled Release Facility in Bozeman, Montana, USA, for Testing Near Surface CO_2 Detection Techniques and Transport Models.” *Environmental Earth Sciences* 60.2 (2010) : 227-239.

Strazisar, Brian R., Arthur W. Wells, J. Rodney Diehl, Richard W Hammack, and Garret A. Veloski. “Near-surface Monitoring for the ZERT Shallow CO_2 Injection Project.” *International Journal of Greenhouse Gas Control* 3.6 (2009) : 736-744.

Torrion, Jessica A. “Development of a New Crop Water Stress Index for Agricultural Crops Using Red, Near-Infrared, and Thermal Infrared Remote Sensing Imagery.” Ph.D. thesis Texas Tech University, Lubbock, 2008. Web. http:// thinktech.lib.ttu.edu/ttu-ir/handle/2346/22546.

COMPARISON OF ZERT THERMAL AND SPECTRAL DATA

The purpose of this chapter is to compare the thermal imager results from Chapter 3 with visible and near-infrared multi-spectral imager data collected during the 2011 summer ZERT release. The analysis in Chapter 3 of this thesis showed that thermal imagery can be used alone to identify the location of a CO_2 gas leak through vegetation stress. Similarly, previous research in our lab has shown that a combination of visible and near-infrared imagery can be used for the same purpose (Rouse 2008, Rouse et al. 2010, Hogan 2011, Hogan et al. 2012a,b). The basis of both of these methods is that leaking CO_2 at the root level would cause an elevated plant stress, which would result in an observable change in the reflectance or emission properties of the exposed vegetation. The overall question to be answered in this chapter is whether the thermal data adds statistically meaningful information to the visible and near-infrared data.

Spectral Imaging Methodology

The 2011 ZERT release started July 15th and ended August 15th with a flow rate of 0.15 tons/day. Spectral images were captured using a PixeLink PL-B741U camera system built into a filter-wheel-based multispectral imager developed by the Optical Remote Sensing Laboratory. The camera parameters are summarized in Table 10. A custom optical front-end was inserted between a wide-angle lens (a Tamron MVL65) and the camera. Two 40 nm wide transmission band filters were selected: a near-infrared filter centered at 800 nm and a red filter centered at 630 nm (Hogan 2011). Figure 61 shows the complete camera and optics assembly.

Table 10. PixeLink PL-B741U camera parameters. (Hogan 2011).

Camera Parameter	Parameter Value
Resolution	1280 x 1024
Frame Rate (fps)	27
Power Consumption (W)	3.2
Interface	USB 2.0
Sensor Format	CMOS
Sensor Dimensions (mm)	8.57 x 6.86

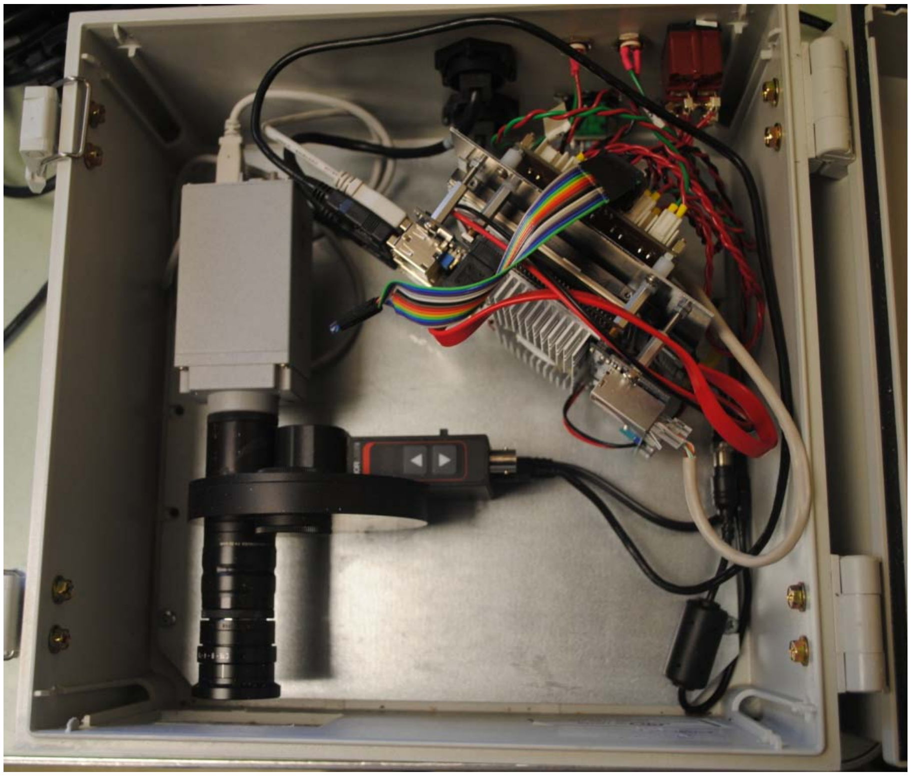

Figure 60. PixeLink imaging system developed by the Optical Remote Sensing Laboratory (Hogan 2011).

The complete system was mounted onto scaffolding at the ZERT field. Figure 35 in Chapter 3 of this thesis shows the spectral imager mounted next to the infrared imager.

The area imaged was approximately the same as that of the infrared imager, showing both affected vegetation and non-exposed vegetation. Also present in the field of view was a spectralon panel for image calibration purposes. Images from both spectral channels were acquired every 10 minutes between roughly 9 AM and 4 PM daily. In a similar manner as the infrared imager, image collection started prior to the CO_2 release in order to capture initial vegetation readings.

Image Processing

Once the images were collected, custom MATLAB routines were run in order to remove images containing non-vegetation items as well as over/under exposed images. Image calibration was performed by masking the spectralon panel in each image. A sample masked image is shown in Figure 62.

Figure 61. Sample imaging showing the spectralon panel masked in red.

The average pixel value within the masked region was then calculated and the digital number of each pixel outside the region was divided by the average spectralon pixel value (Hogan 2011). This ratio was then multiplied by the corresponding known reflectance of the panel. The data was then further reduced by creating an average daily image. From past work, it was found that the late afternoon produced the most stable reflectance bands; therefore, each daily-average image was generated only from the afternoon images (Hogan 2011). Figures 63 and 64 show sample NIR and RED reflectance images.

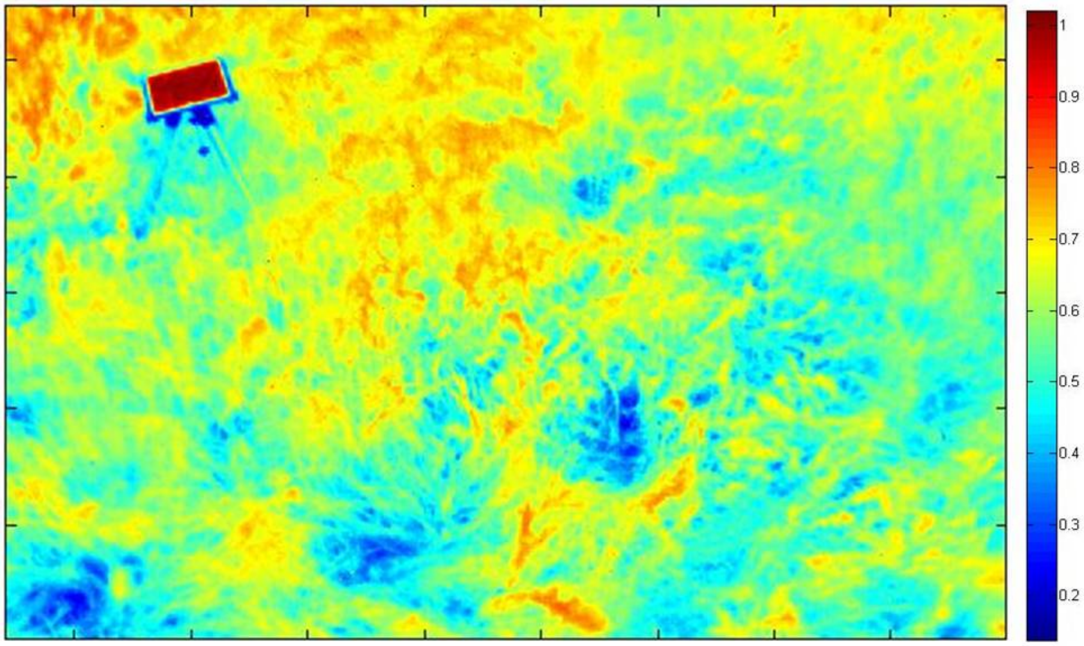

Figure 62. NIR sample daily average image from 7/22/2011.

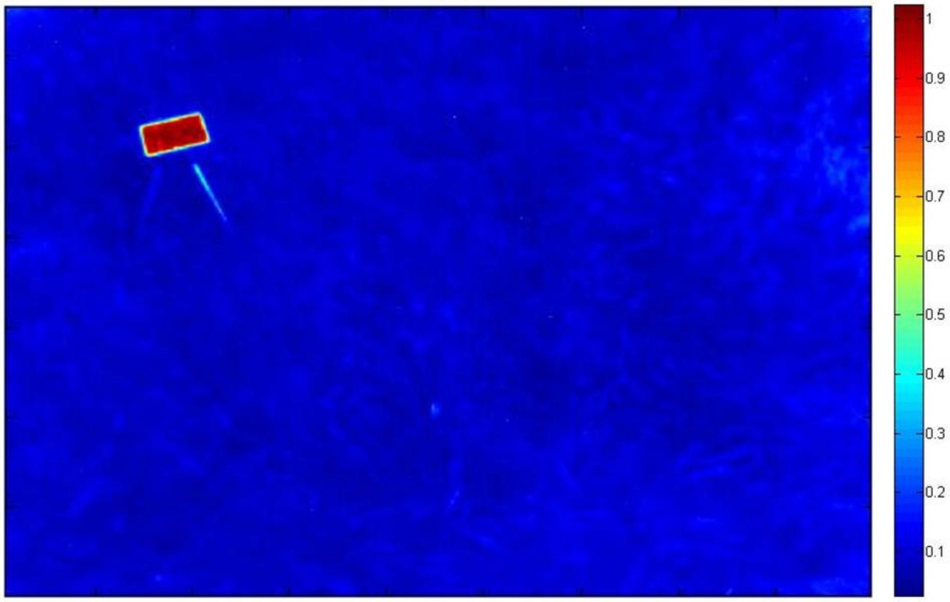

Figure 63. RED sample daily average image from 7/22/2011.

The normalized difference vegetation index, NDVI, was determined using Equation 1.

$$NDVI = \frac{NIR-RED}{NIR+RED} \quad [1]$$

A sample NDVI image is shown in Figure 65.

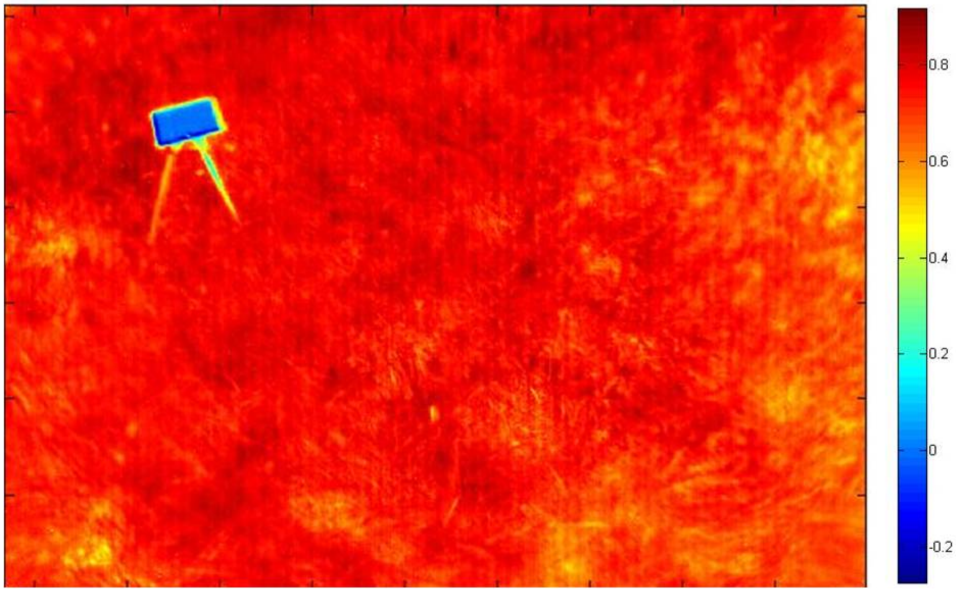

Figure 64. NDVI sample daily average image from 7/22/2011.

From the average images, a custom MATLAB script was used to select three regions of interest. Previous work used only two regions, but concerns over the camera viewing angle were raised. Since the multi-spectral imager views such a large area of vegetation from relatively close to the surface, the viewing angle of the imager changes notably between the bottom and top of the image. Using only control regions at these two edges could possibly result in skewed reflectance data due to angular variation in the bidirectional reflectance distribution function (BRDF). Using a control region in the same horizontal line as the hot spot region, in addition to the control region located diagonally from the hot spot, allows this concern to be addressed by comparing any differences in the radiance reflected from both control regions. Figure 66 shows the three regions of interest.

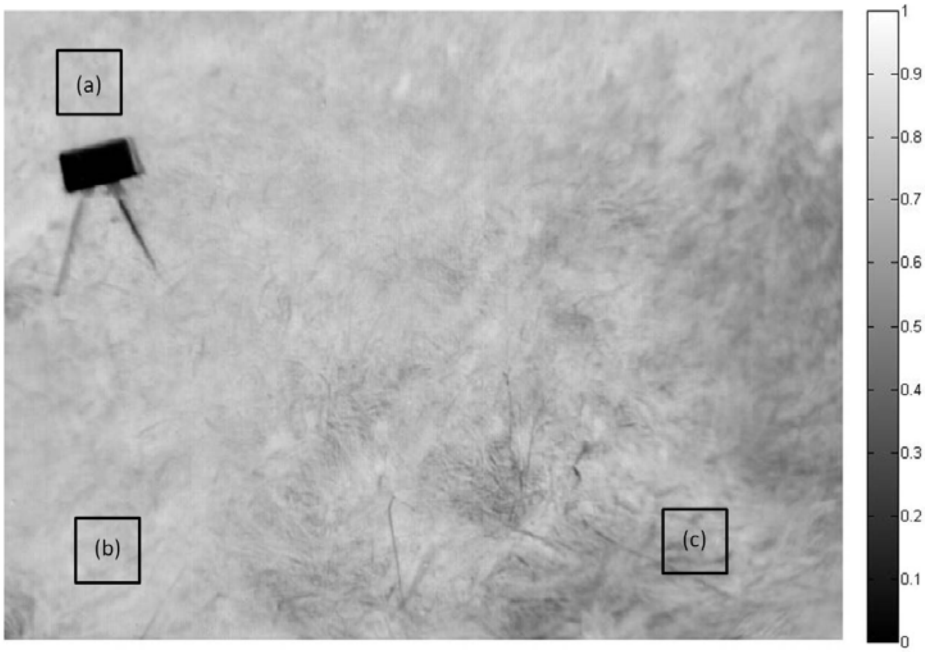

Figure 65. Regions of interest: (a) vertical control region, (b) horizontal control region, and (c) hot spot region.

For each region of interest, vectors were created containing the day number, the NIR reflectance values, the RED reflectance values, and the calculated NDVI values.

Statistical Model

Using the spectral data, linear regressions for the RED reflectance, NIR reflectance, and the NDVI versus day were calculated. A statistical model was used similar to one used on the previous years' spectral results (Hogan 2011). One significant difference was the inclusion of the infrared radiance from the thermal camera. These data were composed of the maximum radiance measured during the afternoon hours for each region of interest. It was truncated to include only data from the time period overlapping the operation of the PixeLink camera. A second difference in the statistical model was the inclusion of the second control region to determine the effects of the camera viewing angle. The generalized model is given by Equation 2.

$$DAY = \beta_0 + \beta_1 RED + \beta_2 NIR + \beta_3 NDVI + \beta_4 THERMAL + \beta_5 REGION + (\beta_6 RED * REGION) + (\beta_7 NIR * REGION) + (\beta_8 NDVI * REGION) + (\beta_9 THERMAL * REGION) \quad [2]$$

In Equation 2 the term *REGION* refers to the categorical variable representing a specific region of interest. It is defined as the "vertical control," the "horizontal control," or the "hot spot," depending on which region is being analyzed. For the purposes of this thesis, four separate cases of linear regressions were examined. The first was using only the NDVI values with respect to the regions of interest. This is shown in Equation 3.

$$DAY = \beta_0 + \beta_1 NDVI + \beta_2 REGION + (\beta_3 NDVI * REGION) \quad [3]$$

The second case looked at the combination of the RED and NIR reflectances with respect to the regions of interest. The equation for this case is given by Equation 4.

$$DAY = \beta_0 + \beta_1 NIR + \beta_2 RED + \beta_3 REGION + (\beta_4 NIR * REGION) + (\beta_5 RED * REGION) \qquad [4]$$

The third case looked at only the thermal data with respect to region of interest. This is shown by Equation 5.

$$DAY = \beta_0 + \beta_1 THERMAL + \beta_2 REGION + (\beta_3 THERMAL * REGION) \qquad [5]$$

The fourth case looked at the full model linear regression of the thermal data combined with the thermal and reflectance data, as given in Equation 2.

Statistical Results

Case I: NDVI Regression Data

The overall NDVI data set was plotted versus the day of the release in Figure 67. The resulting plot was consistent with the data from previous years, showing a consistent downward trend over the length of the release, and a notably higher rate of decay for the hot spot region where the vegetation experiences stress from the leaking CO_2 gas.

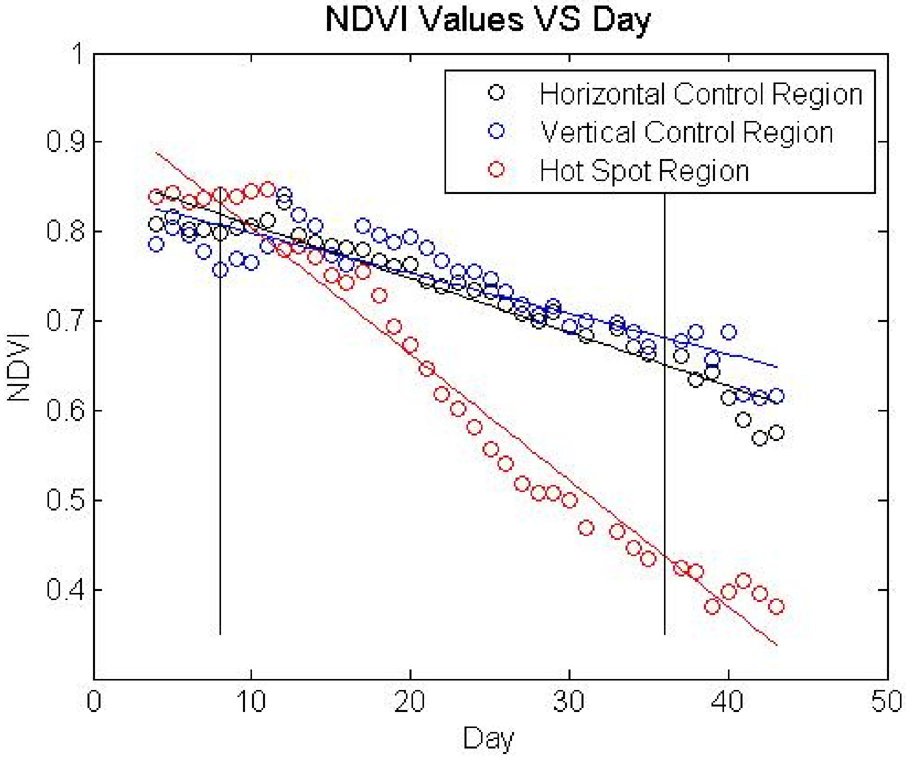

Figure 66.NDVI values plotted versus day of the experiment for the three regions of interest. The vertical lines show the start and end of the release.

Figure 67 shows that both control regions behaved in much the same way, suggesting that the camera viewing angle had little to no effect on the results. This is the same result as was found with the two control regions in the infrared image data (ch. 3). The hot spot region differed greatly from the two control regions. While starting slightly higher, it quickly dropped below the two controls after the start of the release with a much steeper slope than either control region, before leveling off at the end of the release. The regression results are shown in Table 11.

Table 11. DAY vs NDVI Regression Summary (eq. 3).

Parameter	**Term**	**Estimate**	**Standard Error**	**t value**	**Two-sided p-value**
NDVI Intercept	β_0	153.932	7.705	19.978	<0.001
NDVI Slope	β_1	-176.973	10.378	-17.052	<0.001
Vertical Control Intercept	β_2	-17.318	9.878	-1.753	0.0824
Hot Spot Intercept	β_2	-88.374	8.055	-10.971	<0.001
Vertical Control NDVI Slope	β_3	21.211	13.369	1.587	0.116
Hot Spot NDVI Slope	β_3	108.388	11.002	9.851	<0.001

The t value in Table 11 is known as the test statistic for this case where the regression test uses a Student's t distribution. The p-value is the probability of observing a sample statistic that is as extreme as the test statistic. This regression resulted in a residual standard error of 3.738 on 108 degrees of freedom with an adjusted R-squared value of 0.90. Since a term is only counted as statistically significant if its p-value is less than ~0.05, the results presented in Table 11 suggest that the vertical control NDVI slope term is not significant to the regression and can be removed. This term was removed, but not the Vertical Control intercept because of its higher p-value. Rerunning the regression yielded the final results presented in Table 12.

Table 12. Reduced Day vs NDVI Regression Summary (eq. 3).

Parameter	**Term**	**Estimate**	**Standard Error**	**t value**	**Two-sided p-value**
NDVI Intercept	β_0	144.472	4.914	29.400	<0.001
NDVI Slope	β_1	-164.191	6.588	-24.923	<0.001
Vertical Control Intercept	β_2	-1.706	0.866	-1.969	0.0515
Hot Spot Intercept	β_2	-78.914	5.454	-14.469	<0.001
Hot Spot NDVI Slope	β_3	95.607	7.545	12.671	<0.001

These results show that all the terms were now statistically significant, although the vertical control intercept was less significant than that of the hot spot. The results show that there is an important difference between the vertical control region and the hot spot region. Both regions are being compared with the horizontal control region in the regression. The coefficient estimate for the hot spot intercept is substantially larger than the vertical control intercept coefficient, meaning it has much more effect on the regression model. The small value of the intercept coefficient of the vertical control region means it has a small effect on the model as it relates to the horizontal control region. This regression gave a residual standard error of 3.764 on 109 degrees of freedom with an adjusted R-squared value of 0.90. The residuals for the NDVI model are shown in Figure 68.

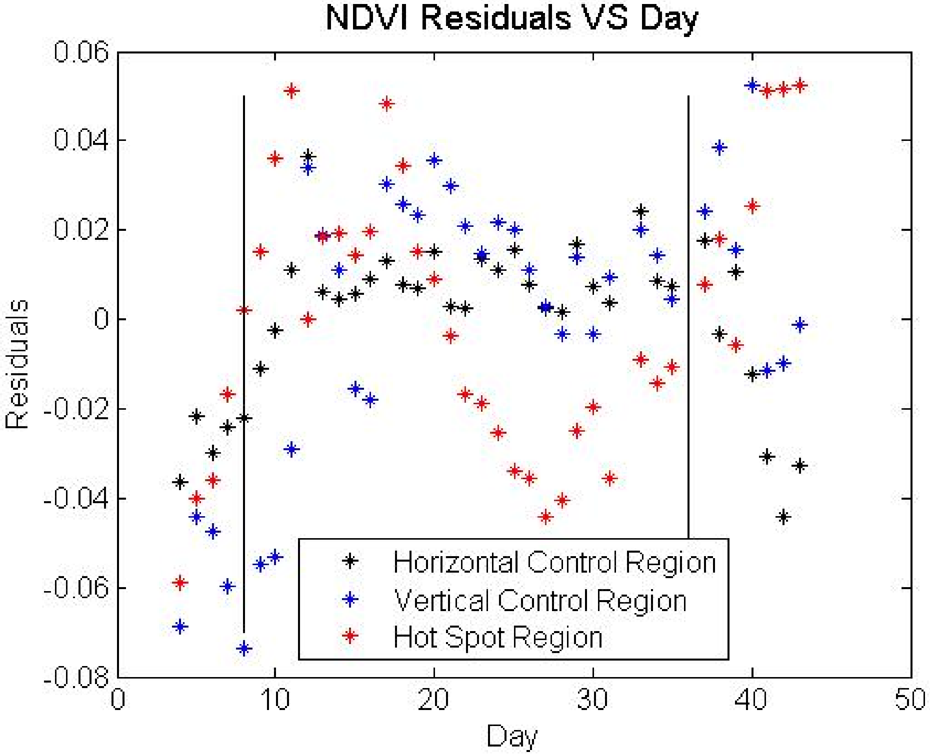

Figure 67. NDVI residuals for the regression in Table 12.

The plot of the NDVI residuals shows a strong sigmoid pattern for the three regions. Additionally, the model showed signs of serial correlation, which was tested for and the model was corrected. Equations 6, 7, and 8 were used to calculate the Durbin-Watson serial correlation coefficient for both the hot spot region and the control region (Hogan 2011).

$$r_1 = \frac{c_1}{c_0} \qquad [6]$$

$$c_1 = \frac{1}{n-1}\sum_{t=2}^{n}(residuals_t - residuals_{t-1}) \qquad [7]$$

$$c_0 = \frac{1}{n-1}\sum_{t=1}^{n}(residuals_t^2) \qquad [8]$$

Once the serial correlation term, r_1, was determined, a new corrected F-statistic was calculated using Equation 9.

$$F_{new} = \frac{1}{\sqrt{\frac{1+r_1}{1-r_1}}} \times F_{original} \qquad [9]$$

The results of the serial correlation correction are shown in Table 13 for the NDVI model.

Table 13. NDVI Serial Correlation Summary.

Region	Correlation Coefficient	Original F-stat	Original p-value	Corrected F-Stat	Corrected p-value
Hot Spot	0.372	242.2	<0.001	90.10	<0.001
Vertical Control	0.445	242.2	<0.001	107.74	<0.001

Serial correlation was present in both regions, with more in the vertical control region than the hot spot. However correcting for it did not change the confidence level of the model. Introducing squared and cubed terms into the regression produced no noticeable improvement to the residuals and were found to not be statistically significant.

Case II: NIR and RED
Reflectance Regression Data

The overall RED and NIR reflectances were plotted versus the day of the release in Figures 69 and 70. The resulting plots were consistent with the data from previous years, showing a consistent upward trend in the RED and a downward trend in the NIR over the length of the release.

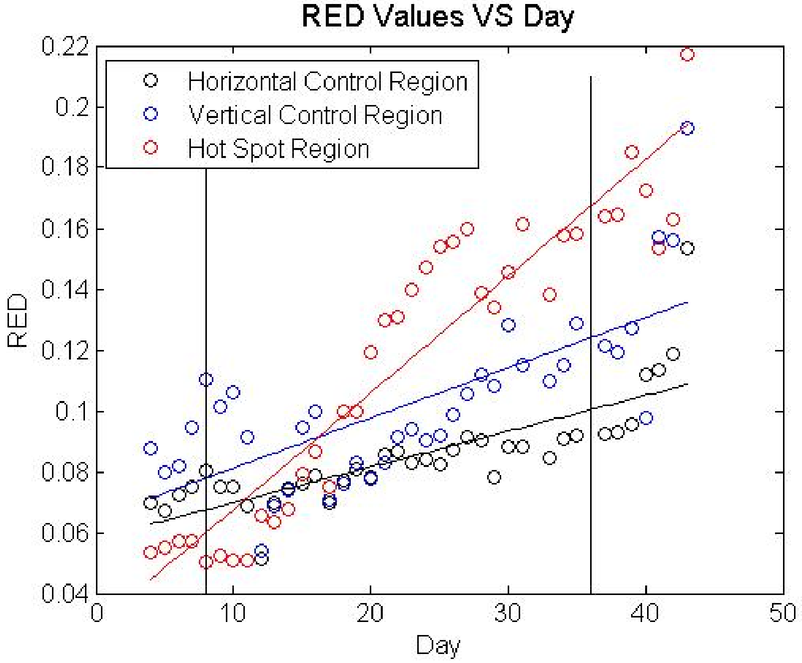

Figure 68. RED reflectance plotted versus day of the experiment for the three regions of interest. The vertical lines show the start and end of the release.

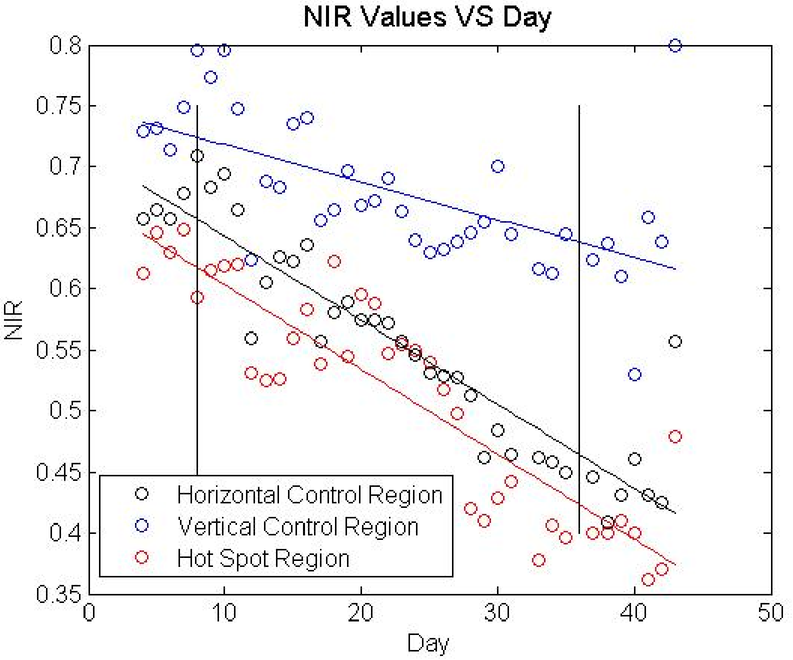

Figure 69. NDVI values plotted versus day of the experiment for the three regions of interest. The vertical lines show the start and end of the release.

The plot of the RED reflectance again showed the two control regions behaving in very similar manners, while the hot spot experiences a much steeper slope. As with the NDVI plot, the exposed vegetation began to change very soon after the start of the release. The regression results are shown in Table 14.

Table 14. DAY vs RED and NIR Reflectance Regression Summary (eq. 4).

Parameter	Term	Estimate	Standard Error	t value	Two-sided p-value
Intercept	β_0	74.908	4.618	16.220	<0.001
RED Slope	β_1	332.729	14.632	22.740	<0.001
NIR Slope	β_2	-126.880	6.545	-19.387	<0.001
Vertical Control Intercept	β_3	-26.058	6.467	-4.030	<0.001
Hot Spot Intercept	β_3	-41.302	6.526	-6.328	<0.001
Vertical Control NIR Slope	β_4	34.868	8.375	4.163	<0.001
Hot Spot NIR Slope	β_4	71.572	9.285	7.708	<0.001
Vertical Control RED Slope	β_5	-37.862	30.340	-1.248	0.215
Hot Spot RED Slope	β_5	-181.378	19.265	-9.415	<0.001

This regression resulted in a residual standard error of 2.379 on 105 degrees of freedom with an adjusted R-squared value of 0.96. The results presented in Table 14 suggest that the vertical control RED slope term was not significant to the regression and could be removed. Removing this term and rerunning the regression yielded the final results presented in Table 15.

Table 15. Reduced Day vs RED and NIR Reflectance Regression Summary (eq. 4).

Parameter	Term	Estimate	Standard Error	t value	Two-sided p-value
Intercept	β_0	75.655	4.59	16.478	<0.001
RED Slope	β_1	323.923	12.852	25.205	<0.001
NIR Slope	β_2	-126.651	6.559	-19.309	<0.001
Vertical Control Intercept	β_3	-30.936	5.165	-5.989	<0.001
Hot Spot Intercept	β_3	-42.049	6.516	-6.453	<0.001
Vertical Control NIR Slope	β_4	37.640	8.096	4.649	<0.001
Hot Spot NIR Slope	β_4	71.344	9.308	7.665	<0.001
Hot Spot RED Slope	β_5	-172.572	17.974	-9.601	<0.001

These results showed that all the terms were now statistically significant. This regression gave a residual standard error of 2.385 on 106 degrees of freedom with an adjusted R-squared value of 0.96. The residuals for the RED and NIR models are shown in Figures 71 and 72, respectively.

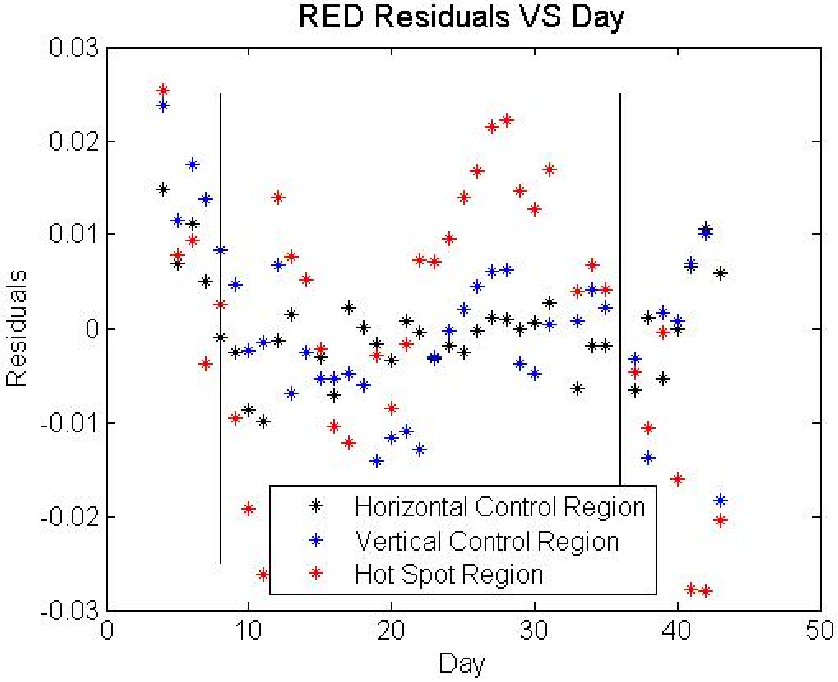

Figure 70. RED residuals for the regression in Table 14.

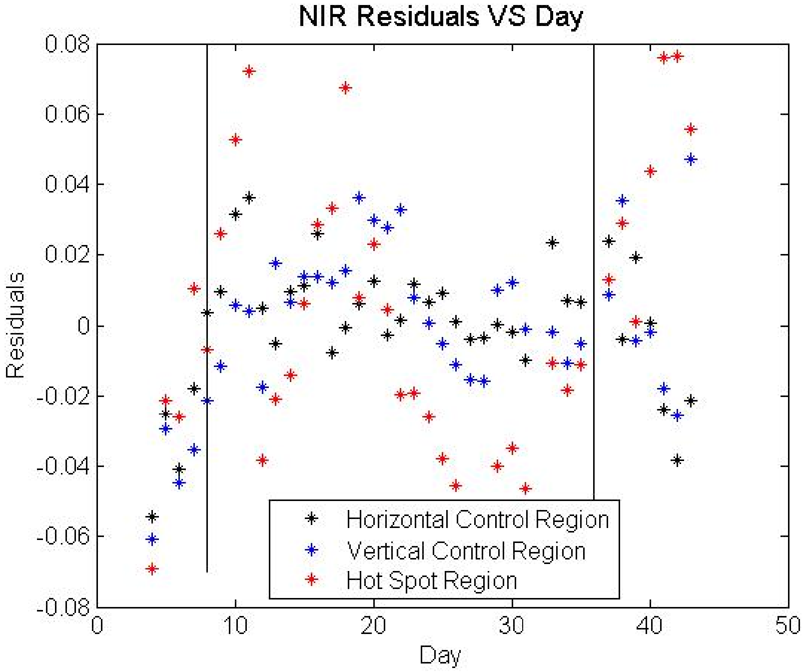

Figure 71. NIR residuals for the regression in Table 14.

The results of the serial correlation correction are shown in Tables 16 for the RED and NIR reflectance model.

Table 16. RED and NIR Reflectance Serial Correlation Summary.

Region	Correlation Coefficient	Original F-stat	Original p-value	Corrected F-Stat	Corrected p-value
Hot Spot	0.657	368.4	<0.001	163.03	<0.001
Vertical Control	0.494	368.4	<0.001	214.43	<0.001

As with the NDVI residuals, both the RED and NIR residual plots showed serial correlation, but correcting for it did not change the confidence level of the model. This divergence of the hot spot from the control regions began fairly shortly after the release of CO_2 starts, meaning the change in reflectances was likely a result of the exposure. The control regions behaved very similarly in both the RED and NIR. Introducing squared and cubed terms into the regression produced no noticeable improvement to the residuals.

Case III: Thermal Regression Data

The thermal data was truncated to the exact range of days represented in the spectral data. The maximum temperature values were selected from between the hours of 10 AM and 2 PM for each day to correspond with the spectral data averages. The overall data are plotted versus the day of the release in Figure 73.

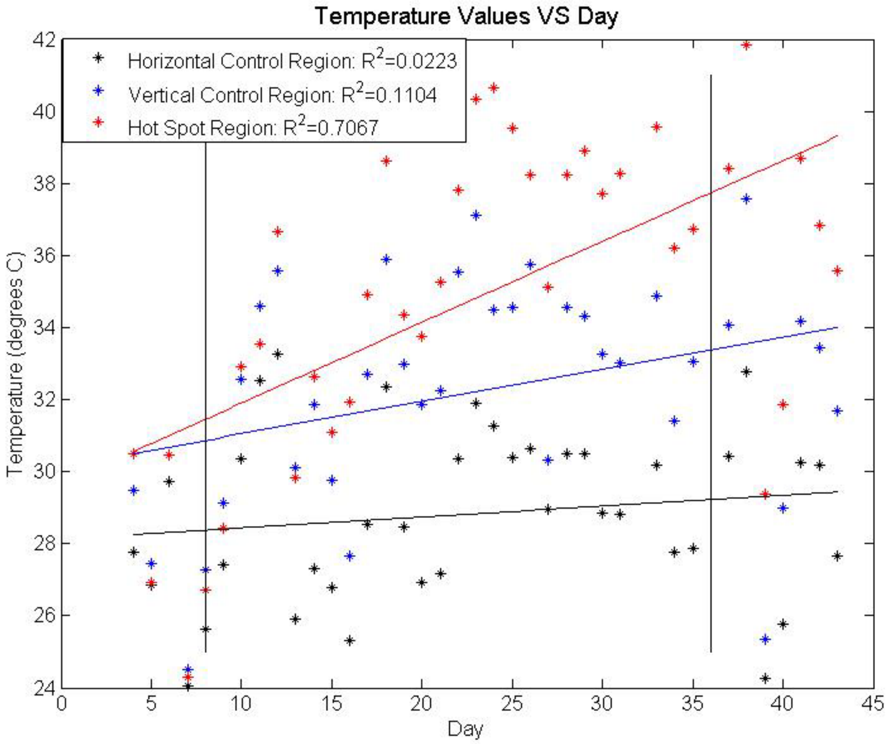

Figure 72. RED reflectance plotted versus day of the experiment for the three regions of interest. The vertical lines show the start and end of the release.

Both control regions showed similar slopes, but with offset intercepts, while the hot spot showed a much steeper slope. The hot spot region began to increase in temperature quickly after the start of the release before leveling off as the vegetation dies off towards the end of the release. The regression results are shown in Table 17.

Table 17. DAY vs THERMAL Reflectance Regression Summary (eq. 5).

Parameter	Term	Estimate	Standard Error	t value	Two-sided p-value
Intercept	β_0	-0.238	22.030	-0.011	0.991
THERMAL Slope	β_1	0.822	0.762	1.079	0.283
Vertical Control Intercept	β_2	-18.668	28.852	-0.647	0.519
Hot Spot Intercept	β_2	-36.426	26.444	-1.378	0.171
Vertical Control Thermal Slope	β_3	0.494	0.955	0.517	0.606
Hot Spot Thermal Slope	β_3	0.906	0.868	1.043	0.299

This regression resulted in a residual standard error of 11.02 on 108 degrees of freedom with an adjusted R-squared value of 0.14. These results suggested that the thermal data did not seem to be a reasonable replacement for the RED and NIR data. A reduced statistical model was written by removing the vertical control intercept and thermal slope along with the hot spot intercept. These factors were removed one at a time, based on which had the highest p-value until the remaining terms became statistically significant. Rerunning the regression yielded the final results presented in Table 18.

Table 18. Reduced Day vs Thermal Data Regression Summary (eq. 5).

Parameter	Term	Estimate	Standard Error	t value	Two-sided p-value
Intercept	β_0	-14.649	8.862	-1.653	0.101
THERMAL Slope	β_1	1.248	0.287	4.344	<0.01
Hot Spot Thermal Slope	β_2	5.354	2.525	-2.120	0.036

This regression resulted in a residual standard error of 11.09 on 111 degrees of freedom with an adjusted R-squared value of 0.13. The residuals for the thermal data regression are shown in Figure 74.

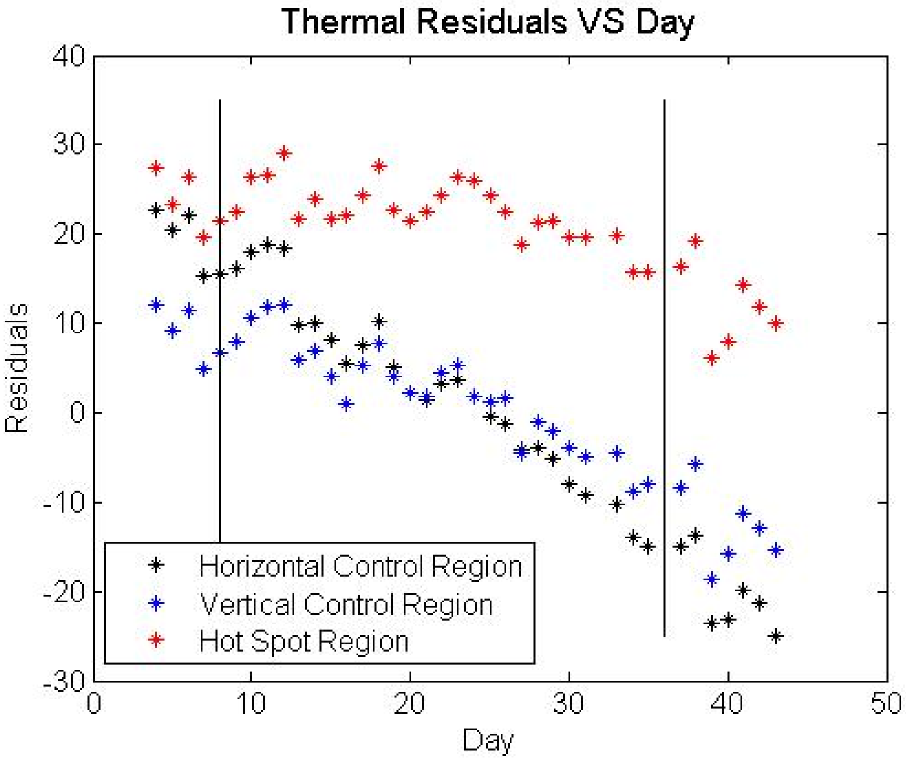

Figure 73. Thermal residuals for the regression in Table 18.

The residual plot showed a clear difference between the two control regions and the hot spot region. Introducing squared and cubed terms into the regression produced no noticeable improvement to the residuals. These regression results showed that the thermal data contain statistically meaningful information that may be useful for identifying the location of a gas leak. Most notably, simply plotting the temperature differences between the regions as a function of time, gives much stronger evidence of a CO_2 leak, as described in chapter 3 of this thesis.

A linear regression also was performed on the diurnal difference of vegetation infrared brightness temperature, measured at 1 PM and 3 AM (approximately the maximum and minimum temperatures). Plots of these diurnal temperature difference data are shown for the three regions of interest in Figure 59 of chapter 3. The regression equation is given by Equation 10.

$$DAY = \beta_0 + \beta_1 DIFFERENCE + \beta_2 REGION + (\beta_3 DIFFERENCE * REGION) \qquad [10]$$

The term *DIFFERENCE* represents the diurnal temperature difference for each region. The regression results are shown in Table 19.

Table 19. DAY vs DIFFERENCE Reflectance Regression Summary (eq. 10).

Parameter	Term	Estimate	Standard Error	t value	Two-sided p-value
Intercept	β_0	-1.235	8.128	-0.152	0.879
DIFFERENCE Slope	β_1	1.788	0.384	4.659	<0.001
Vertical Control Intercept	β_2	-8.865	11.071	-0.801	0.424
Hot Spot Intercept	β_2	4.177	12.296	0.340	0.734
Vertical Control Difference Slope	β_3	0.253	0.502	0.503	0.615
Hot Spot Difference Slope	β_3	-0.006	0.626	-0.009	0.993

This regression resulted in a residual standard error of 16.15 on 165 degrees of freedom with an adjusted R-squared value of 0.29. This results in a notably improved regression relative to the initial regression of the maximum daily temperature presented in Table 17. A reduced model was created by systematically removing the *DIFFERENCE*REGION* terms along with the *VERTICAL CONTROL* term. Rerunning the regression yielded the final results presented in Table 20.

Table 20. Reduced Day vs Difference Data Regression Summary (eq. 10).

Parameter	Term	Estimate	Standard Error	t value	Two-sided p-value
Intercept	β_0	-0.458	4.467	-0.103	0.9184
DIFFERENCE Slope	β_1	1.853	0.218	8.505	<0.001
Hot Spot Difference Slope	β_2	-5.471	2.693	-2.031	0.0438

This regression resulted in a residual standard error of 16.12 on 168 degrees of freedom with an adjusted R-squared value of 0.29. This diurnal difference thermal data still yielded a modest regression, although it was stronger than the thermal data shown previously. The residuals for these data are shown in Figure 75.

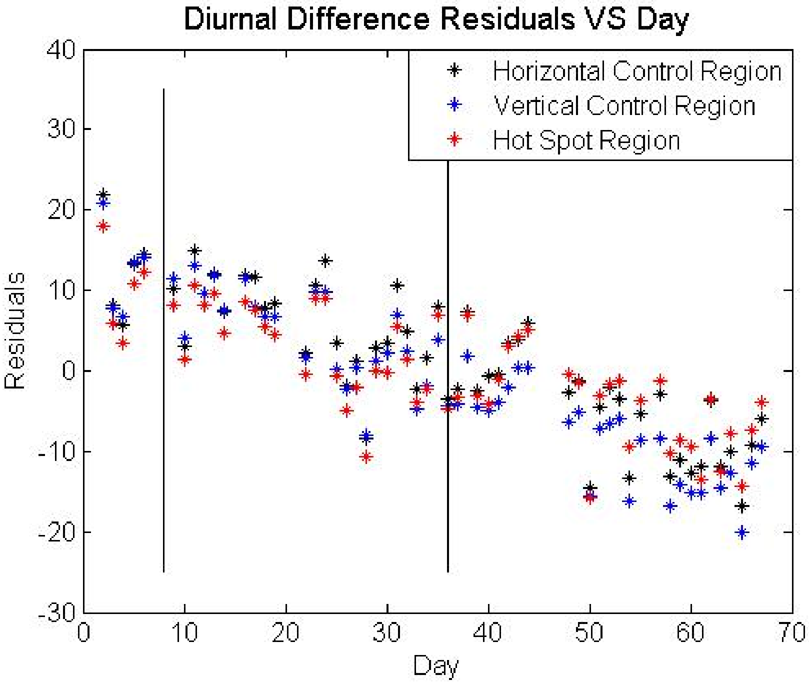

Figure 74. Diurnal difference residuals for the regression in Table 19.

The residual plot showed little difference between the two control regions and the hot spot. Introducing squared and cubed terms into the regression produced no noticeable improvement to the residuals. These regression results suggested that the diurnal brightness temperature difference provided better information to that carried by the maximum temperature obtained between 10 AM and 2 PM.

Case IV: Total Regression Data

For the last case, all the multispectral imager data were combined with the thermal data to determine whether the thermal values become significant alongside the red and NIR values. The regression results are shown in Table 21.

This regression resulted in a residual standard error of 2.274 on 99 degrees of freedom with an adjusted R-squared value of 0.96. The reduced model was created by again removing the term with the highest p-value until the remaining terms were all statistically significant. Rerunning the regression yielded the identical results presented earlier in Table 14. This regression resulted in a residual standard error of 2.385 on 106 degrees of freedom with an adjusted R-squared value of 0.96. The residuals for the reduced full model data are shown in Figures 76 and 77.

Table 21. DAY vs Total Data Regression Summary (eq. 2).

Parameter	Term	Estimate	Standard Error	t value	Two-sided p-value
Intercept	β_0	2.997e+01	3.406e+01	0.880	0.381
NDVI Slope	β_1	2.620e+01	4.828e+01	0.543	0.589
NIR Slope	β_2	-1.033e+02	2.197e+01	-4.702	8.35e-06
RED Slope	β_3	3.629e+02	1.264e+02	2.871	0.00500
Vertical Control Intercept	β_1	-3.729e+01	5.452e+01	-0.684	0.496
Hot Spot Intercept	β_1	3.708e+01	3.801e+01	0.975	0.332
Thermal Slope	β_4	8.408e-03	1.707e-01	0.049	0.961
Vertical Control NDVI Intercept	β_5	6.999e+01	7.832e+01	0.894	0.374
Hot Spot NDVI Intercept	β_5	-8.828e+01	5.752e+01	-1.535	0.128
Vertical Control NIR Intercept	β_6	-5.221e+01	3.242e+01	-1.611	0.111
Hot Spot NIR Intercept	β_6	9.240e+01	3.213e+01	2.876	0.00493
Vertical Control RED Intercept	β_7	1.699e+02	1.814e+02	0.936	0.351
Hot Spot RED Intercept	β_7	-3.575e+02	1.475e+02	-2.424	0.0172
Vertical Control Thermal Intercept	β_8	3.012e-01	2.173e-01	1.386	0.169
Hot Spot Thermal Intercept	β_8	-2.419e-02	2.049e-01	-0.118	0.906

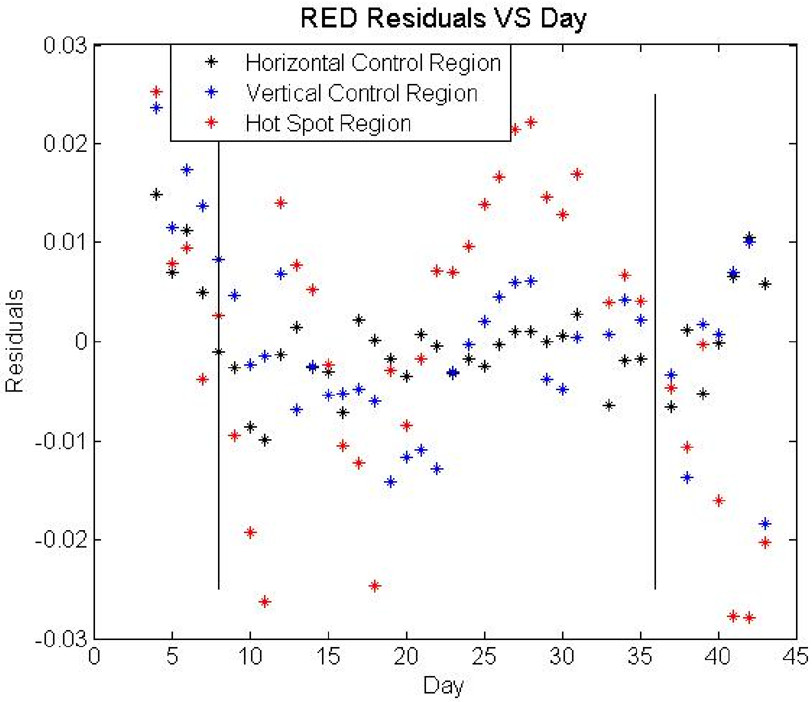

Figure 75. RED residuals for the reduced total data regression in Table 20.

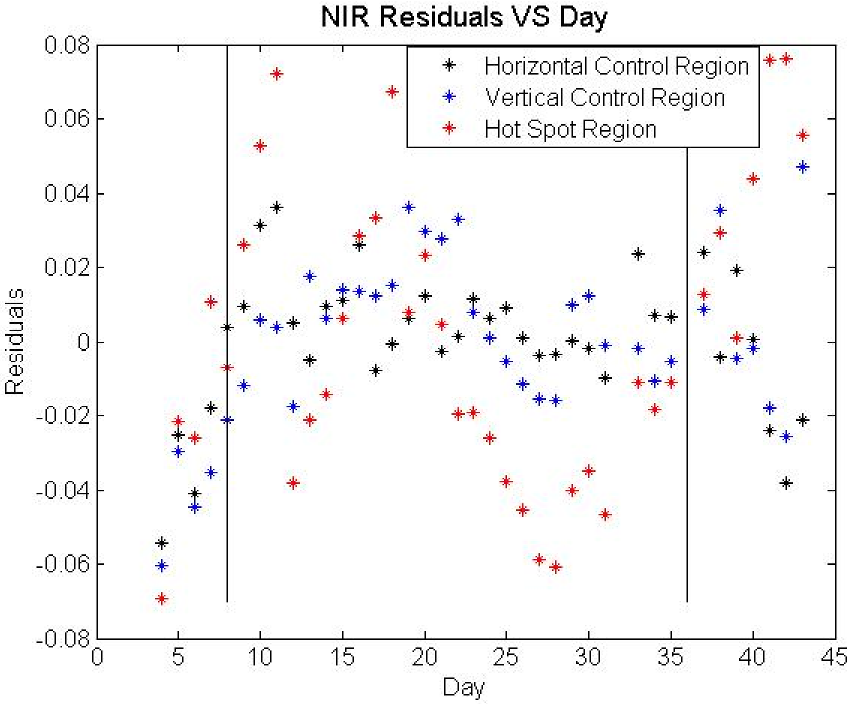

Figure 76. NIR residuals for the reduced total data regression in Table 20.

The residuals were identical to those found in the RED and NIR case. A serial correlation test was not performed on the full model residuals since they were identical to those found previously. Introducing squared and cubed terms into the regression produced no noticeable improvement to the residuals. From the regression model using all the reflectance bands and infrared data, it was concluded that thermal data did not improve the RED and NIR data. The NDVI data were strong by themselves, but ceased to be significant when combined with the RED and NIR values. This was logical, since NDVI is directly dependent on the measured NIR and RED values. Previous analysis of the multi-spectral results showed slightly stronger R^2 values in the NDVI (Hogan 2011 and Rouse 2008). The thermal data were also strong when viewed by themselves as a function of temperature variation between regions. However, including it with the reflectance band data caused it to become not significant, indicating that the thermal data did not carry any statistically significant unique information beyond what was already present in the red and NIR reflectances.

Conclusion

Through comparison of the regression results, it is evident that the data from the infrared imager does not contribute to the reflectance band data beyond that accounted for by the RED and NIR data. Both methods show evidence of the possibility of a CO_2 leak before it is observable in person based on elevated reflectance and thermal radiance values. Additionally, the hot spot region consistently shows much different thermal and reflectance behavior than the two control regions, with statistical significance. The vertical control intercept coefficient was consistently found to be very small in the reduced regression models where it was compared directly to the horizontal control region, meaning there is only a slight concern with the imager viewing angle. The two methods have advantages and disadvantages. The reflectance based method requires only a single image of the vegetation in order to explain approximately 95% of the variance in the data, which is better than that found using the thermal infrared data alone. With a single thermal infrared image, approximately 13% of the data variance was explained, while using two thermal images from the approximate thermal extremes during a day to explained approximately 29% the variance. However, the reliance of the reflectance-band data on a spectralon panel for providing calibrated results can make the thermal infrared imager more practical for routine field use. This is particularly valuable if it is desired to monitor for gas leaks from an airborne platform. Additionally, the data processing for the infrared imager is much simpler than for the multispectral imager's reflectance band data.

References

Hogan, Justin A. "Multi-Spectral Imaging of Vegetation for CO_2 Leak Detection." M.S. thesis Montana State University, Bozeman, 2011. Web. http://etd.lib.montana.edu/etd/view/item.php?id=1255.

Hogan, Justin A., Joseph A. Shaw, Rick L. Lawrence, and Randal M. Larimer. "Low-cost Multispectral Vegetation Imaging System for Detecting Leaking CO_2 Gas." *Applied Optics* 51.4 (2012a): 59-66.

Hogan, Justin A., Joseph A. Shaw, Rick L. Lawrence, Jennifer L. Lewicki, Laura M. Dobeck, and Lee H. Spangler, "Detection of Leaking CO_2 Gas With Vegetation Reflectances Measured By a Low-Cost Multispectral Imager," *IEEE J. Selected Topics Appl. Earth Obs. And Rem. Sens.* 5.3 (2012b): 699-706.

Rouse, Joshua H. "Measurements of Plant Stress in Response to CO_2 Using a Three-CCD Imager." M.S. thesis Montana State University, Bozeman, 2008. Web. http://etd.lib.montana.edu/etd/view/item.php?id=803.

Rouse, Joshua H., Joseph A. Shaw, Rick L. Lawrence, Jennifer L. Lewicki, Laura M. Dobeck, Kevin S. Repasky, and Lee H. Spangler, "Multi-spectral imaging of vegetation for detecting CO_2 leaking from underground," *Environ. Earth Sci.* 60.2 (2010): 313-323.

CONCLUSIONS AND FUTURE WORK

This thesis discusses two novel uses for radiometrically calibrated microbolometer infrared imagers. The calibration techniques developed by the Optical Remote Sensor Lab broadened the uses of radiometrically calibrated remote-sensing thermal imagers. With improved calibrations, microbolometer imagers provide accurate qualitative thermal data, beyond displaying general thermal trends.

My contribution to this research was to be a leading participant in collecting data for both the thermal infrared imaging of the bee hives as well as the imaging the ZERT test site. For the bee hive vitality work, I used calibration algorithms developed previously to radiometrically calibrate the images I acquired and transfer them from the infrared imager to a computer. With assistance I wrote MATLAB scripts to select the hive faces and return the desired radiance values for each hive. I then performed the regression tests on all the thermal infrared images taken in 2010 and 2011. This image processing work on the bee hive images was unique to this thesis, having never been implemented before. For all the ZERT research, I took a leading role in deploying the thermal imager and multispectral imager in 2011. I again used previously developed calibration algorithms to calibrate all the images taken from 2009-2011. I then adapted the custom MATLAB software from the bee imaging research to select regions of interest in the ZERT thermal infrared images and return radiance statistics. I then ran linear regressions on the thermal infrared data, which had never been tried before. To compare the thermal infrared images to the reflectance band data, I used previously developed image manipulation MATLAB software that generated RED, NIR, and NDVI values from each day of the CO_2 release. I then ran linear regressions on the full model containing all the reflectance band values and thermal infrared data. This comparison was unique to my thesis, having never been tried before. For my thesis, I therefore built on previous work with novel thermal imager calibration and multispectral imaging for gas leak detection, and conducted experiments and processed the resulting data sets for two entirely new remote sensing applications.

The first new application discussed was the imaging of beehives with thermal cameras to remotely determine their vitality. Data from several imaging periods between 2010 and 2011 were calibrated and processed. Regressions with large R^2 values were observed between the mean hive temperature and the normalized frame counts. While this technique works adequately for images acquired after sunset, improved regressions were obtained when using images acquired just prior to sunrise. Measurements taken in the early summer were found to be more indicative of hive vitality than those taken in the early fall. This may be a result of the bees' behavior at the approach of winter. Using an uncooled handheld infrared camera to determine hive vitality is a much simpler method than visually inspecting every hive. Commercial bee yards typically have large numbers of hives that would make visual inspections of every hive unrealistic. Using a thermal camera to image large groups of hives simultaneously would be beneficial to commercial bee keepers. For the images analyzed in this thesis, all the bee hives were outdoors.

Future work would involve using the thermal cameras in an enclosed space, similar to the warehouses bee hives are kept in over winter, to demonstrate the method's usefulness in commercial bee keeping. Thermal images acquired in 2011 within a small trailer containing six hives show that thermal signatures can be seen in enclosed spaces. However, frame counts were not available for these hives, meaning nothing is known about the health of the hives to compare with the thermal values. Additionally, an even more compact system would be desirable. The current camera/laptop system is usable by a single person but could be difficult in a crowded warehouse. Requiring the camera to be 3-4 m away from the hives being imaged could also be problematic. With the successful use of thermal signatures to determine hive vitality, it would be worth pursuing the development of a more manageable system, perhaps based on an ultra-compact camera combined with an embedded computer.

The second novel use of the calibrated infrared imager was in determining the location of CO_2 gas leaks from underground, based on vegetation infrared brightness temperatures. The thermal signatures of the unaffected and affected vegetation can be observed to change over the duration of the gas release. This trend is also measured in the statistics from the processed images. For the three sets of summer data reported here, the differences in temperature between the control region and the region near the hot spot clearly showed the effects of the CO_2. Within a day or two of the start of the release, the hot spot region began to diverge from the control region. This change was also present in the diurnal brightness temperature difference. Both regions displayed similar trends at the start of the release, which became noticeably different by the end. The region near the hot spot showed a much higher diurnal temperature profile at the end possibly due to the vegetation’s weakened ability to thermally regulate itself. Other explanations exist for the change in temperature profile, but weakened thermal regulation is an explanation that is consistent with the observations. For the 2011 release, the two controls were found to have very similar trends, meaning the thermal measurements are mostly independent of the camera viewing angle but are statistically significantly different. This suggests that only one control region might be needed in future image processing.

With the successful demonstration of this method of detecting high concentrations of CO_2, the thermal data were then combined with data from the multispectral imager. The multispectral imager has been used in previous years to image the ZERT site and has successfully shown a change in vegetation reflectance due to the CO_2. The purpose of adding the thermal to the spectral data was to see if the regressions could be improved or if the thermal imager is a viable alternative method of making these measurements. Using statistical regression models it was found that the NIR and RED spectral bands provided the strongest regression models. The thermal data were determined not to be statistically significant in the presence of the NIR and RED data. This shows that both methods have potential in remotely detecting CO_2 leaks independent of each other. The benefit of using the thermal imager is that it is simpler, having one channel instead of two, and not requiring the use of a calibration panel in the field.

Future work will include adapting the single thermal imager to a system that is capable of viewing much larger areas. Since so many current and proposed carbon sequestration sites cover much larger areas of land than the ZERT test site, the system will need to be adapted for practical use. Suggested solutions include mounting the thermal imager to a tethered weather balloon or conducting flyovers of the site. Both methods would allow much larger tracts of land to be analyzed. The thermal images would still be processed in the manner described in Chapter 3 of this thesis, with regions selected in a set pattern. Elevated thermal signature readings would indicate a potential leak and confirmation would be made using ground-based gas tests. This would provide a simple, yet effective, method of detecting CO_2 leaks in a timely fashion.

REFERENCES CITED

Alchanatis, V., Y. Cohen, S. Cohen, M. Moller, M. Sprinstin, M. Meron, J. Tsipris, Y. Saranga, and E. Sela. "Evaluation of Different Approaches for Estimating and Mapping Crop Water Status in Cotton with Thermal Imaging." *Precision Agriculture* 11.1 (2010) : 27-41.

Bachu, S. and J.J. Adams. "Sequestration of CO_2 in Geological Media in Response to Climate Change: Capacity of Deep Saline Aquifers to Sequester CO_2 in Solution." *Energy Conversion and Management* 44.20 (2003) : 3151-3175.

Barr, Jamie L., Seth D. Humphries, Amin R. Nehrir, Kevin S. Repasky, Laura M. Dobeck, John L. Carlsten, and Lee H. Spangler. "Laser-based Carbon Dioxide Monitoring Instrument Testing During a 30-day Controlled Underground Carbon Release Field Experiment." *International Journal of Greenhouse Gas Control* 5.1 (2011) : 138-145.

Batjes, N.H. "Mitigation of Atmospheric CO_2 Concentrations by Increasing Carbon Sequestration in the Soil." *Biology and Fertility of Soils* 27.3 ((1998) : 230-235.

Bellante, Gabriel John. "Hyperspectral Remote Sensing as a Monitoring Tool for Geological Carbon Sequestration." MA thesis Montana State University, Bozeman, 2011. Web.

Carroll, Susan, Yue Hao, and Roger Aines. "Geochemical Detection of Carbon Dioxide in Dilute Aquifers." *Geochemical Transactions* 10.4 (2009).

Ehlig-Economides, Christine and Michael J. Economides. "Sequestering Carbon Dioxide in a Closed Underground Volume." *Journal of Petroleum Science and Engineering* 70.1-2 (2010) : 123-130.

Foley, I., Personal Correspondence to P. W. Nugent, State Entomologist, Montana Department of Agriculture, February 2011.

Geoffray, Herve, Alain Bardoux, Michel Laporte, and Jean-Luc Tissot, "Uncooled Infrared Microbolometer Arrays for Earth Remote Sensing", Proc. SPIE 4130, 527 (2000).

Hogan, Justin A. "Multi-Spectral Imaging of Vegetation for CO_2 Leak Detection." M.S. thesis Montana State University, Bozeman, 2011. Web. http://etd.lib.montana.edu/etd/view/item.php?id=1255.

Hogan, Justin A., Joseph A. Shaw, Rick L. Lawrence, and Randal M. Larimer. "Low-cost Multispectral Vegetation Imaging System for Detecting Leaking CO_2 Gas." *Applied Optics* 51.4 (2012a) : 59-66.

Hogan, Justin A., Joseph A. Shaw, Rick L. Lawrence, Jennifer L. Lewicki, Laura M. Dobeck, and Lee H. Spangler, "Detection of Leaking CO_2 Gas ith Vegetation Reflectance Measured by a Low-Cost Multispectral Imager," *IEEE J. Selected Topics Appl. Earth Obs. Remote Sensing* 5.3 (2012b) : 699-706.

Holloway, Sam. "Storage of Fossil Fuel-Derived Carbon Dioxide Beneath the Surface of the Earth." *Annual Review of Energy and the Environment* 26 (2001) : 145-166.

Jackson, R. D., S. B. Idso, R. J. Reginato, and P. J. Pinter Jr. :Canopy Temperature as a Crop Water Stress Indicator." *Water Resources Research* 17.4 (1981) : 1133-1138.

Jensen, M., 2011: Personal correspondence to P. W. Nugent, Smoot Honey Company, Power, MT.

Kastberger, Gerald and Reinhold Stachl. "Infrared Imaging Technology and Biological Applications." *Behavioral Research Methods, Instruments, & Computers* 35.3 (2003) : 429-439.

Katayama, Haruyoshi , Masataka Naitoh, Masahiro Suganuma, Masatomo Harada, Yoshihiko Okamura, Yoshio Tange, and Koji Nakau. "Development of the Compact InfraRed Camera (CIRC) for Wildfire Detection." Proc. SPIE7458 (2009).

Keith, Charlie J., Kevin S. Repasky, Rick L. Lawrence, Steven C. Jay, and John L. Carlsten. "Monitoring Effects of a Controlled Subsurface Carbon Dioxide Release on Vegetation Using a Hyperspectral Imager." *International Journal of Greenhouse Gas Control* 3:5 (2009) : 626-632.

Kleinhenz, Marco, Brigitte Bujok, Stefan Fuchs, and Jürgen Tautz. "Hot Been in Empty Broodnest Cells: Heating From Within." *The Journal of Experimental Biology* 206.23 (2003) : 4217-4231.

Kruse, Paul W. *Uncooled Thermal Imaging: Arrays, Systems, and Applications*. Bellingham: ASPIE-The International Society for Optical Engineering, 2001. Print.

Liddiard, Kevin C. "The Active Microbolometer: A New Concept in Infrared Detection." *Microelectronics: Design, Technology, and Packaging* Proc. SPIE 5274, 227 (2004).

Male, Erin Jing, William L. Pickles, Eli A. Silver, Gary D. Hoffmann, Jennifer Lewicki, Martha Apple, Kevin Repasky, and Elizabeth A. Burton. "Using Hyperspectral Plant Signatures for CO_2 Leak Detection During the 2008 ZERT CO_2

Sequestration Field Experiment in Bozeman, Montana." *Environmental Earth Sciences* 60.2 (2010) : 251-261.

McAlexander, Ian, Greg H. Rau, Jimmy Liem, Thomas Owano, Ray Fellers, Douglas Baer, and Manish Gupta. "Deployment of a Carbon Isotope Ratiometer for the Monitoring of CO_2 Sequestration Leakage." *Analytical Chemistry* 83.16 (2011) : 6223-6229.

Menenti, Massimo, Li Jia, and Zhao-Liang Li. "Multi-angular Thermal Infrared Observations of Terrestrial Vegetation." *Advances in Land Remote Sensing: System, Modelling, Inversion, and Application* 1. (2008) : 51-93.

Moran, M. S. "Thermal Infared Measurements as an Indicator of Plant Ecosystem Health." in *Thermal Remote Sensing in Land Surface Processes*, D. A. Quattrochi and J. C. Luvall (Ed) London: Taylor and Francis, 2004. Pp. 257-282.

Niklaus, Frank, Christian Vieider, and Henrik Jakobsen, "MEMS-Based Uncooled Infrared Bolometer Arrays: a Review", Proc. SPIE 6836, 68360D (2007).

Nogues, Juan P., Jan M. Nordbotten, and Michael A. Celia. "Detecting Leakage of Brine or CO_2 Through Abandoned Wells in a Geological Sequestration Operation Using PressureMonitoring Wells." *Energy Procedia* 4 (2011) : 3620-3627.

Noomen, M.F. and A.K. Skidmore. "The Effects of High Soil CO_2 Concentrations on Leaf Reflectance of Maize Plants." *International Journal of Remote Sensing* 30.2 (2009) : 481-497.

Nugent, Paul W., Joseph A. Shaw, and Sabino Piazzolla. "Wide Angle Infrared Cloud Imaging for Measuring Cloud Statistics in Support of Earth Space Optical Communication." Proc. SPIE 6709 (2007).

Nugent, Paul W. "Wide-Angle Infrared Cloud Imaging for Cloud Cover Statistics." MA thesis Montana State University, Bozeman, 2008. Web.

Nugent, Paul W., Joseph A. Shaw, and Sabino Piazzolla. "Infrared Cloud Imaging in Support of Earth-Space Optical Communication." *Optics Express* 17.10 (2009).

Ono, Masato, Takeshi Igarashi, Eishi Ohno, and Masami Sasaki. "Unusual Thermal Defence by a Honeybee Against Mass Attack by Hornets." *Nature* 377 (1995) : 334-336.

Rogalski, Antoni. "Infrared Detectors: An Overview." *Infrared Physics & Technology* 43.3-5 (2002) : 187-210.

Rouse, Joshua H. "Measurements of Plant Stress in Response to CO_2 Using a Three-CCD Imager." M.S. thesis Montana State University, Bozeman, 2008. Web. http://etd.lib.montana.edu/etd/view/item.php?id=803.

Rouse, Joshua H., Joseph A. Shaw, Rick L. Lawrence, Jennifer L. Lewicki, Laura M. Dobeck, Kevin S. Repasky, and Lee H. Spangler. "Multi-spectral Imaging of Vegetation for Detecting CO_2 Leaking From Underground." *Environmental Earth Sciences* 60.2 (2010) : 313-323.

Shaw, Joseph A., Paul W. Nugent, Nathan J. Pust, Brentha Thurairajah, and Kohei Mizutani, "Radiometric Cloud Imaging with an Uncooled Microbolometer Thermal Infrared Camera," *Optics Express* **13**(15), 5807-5817, http://dx.doi.org/10.1364/OPEX.13.005807 (2005).

Shaw, Joseph A., Paul W. Nugent, Jennifer Johnson, Jerry J. Bromenshenk, Colin B. Henderson, and Scott Debnam. "Long-wave Infrared Imaging for Non-invasive Beehive Population Assessment." *Optics Express* 19.1 (2011) : 399-408.

Spangler, Lee H. et al. "A Shallow Subsurface Controlled Release Facility in Bozeman, Montana, USA, for Testing Near Surface CO_2 Detection Techniques and Transport Models." *Environmental Earth Sciences* 60.2 (2010) : 227-239.

Stabentheiner, Anton, Helga Pressl, Thomas Papst, Norbert Hrassnigg, and Karl Crailsheim. "Endothermic Heat Production in Honeybee Winter Clusters." *The Journal of Experimental Biology* 206.2 (2003) : 353-358.

Strazisar, Brian R., Arthur W. Wells, J. Rodney Diehl, Richard W Hammack, and Garret A. Veloski. "Near-surface Monitoring for the ZERT Shallow CO_2 Injection Project." *International Journal of Greenhouse Gas Control* 3.6 (2009) : 736-744.

Thurairaijah, Brentha and Joseph A. Shaw, "Cloud Statistics Measured with the Infrared Cloud Imager," *IEEE Trans. Geosci. Remote Sens.* **43**(9), 2000-2007 (2005).

Torrion, Jessica A. "Development of a New Crop Water Stress Index for Agricultural Crops Using Red, Near-Infrared, and Thermal Infrared Remote Sensing Imagery." Ph.D. thesis Texas Tech University, Lubbock, 2008. Web. http:// thinktech.lib.ttu.edu/ttu-ir/handle/2346/22546.

Xu, Xiangdong, Zhuo Yang, Zhi Wang, Chao Chen, Dong Zhou, Yang Yang, and Yadong Jiang. "Advanced Design of Microbolometers for Uncooled Infrared Detectors." *2011 International Conference on Information Science and Technology* (2011) : 745.

APPENDICES

APPENDIX A

BEE YARD MAPS

Bee Yard Map May 2010

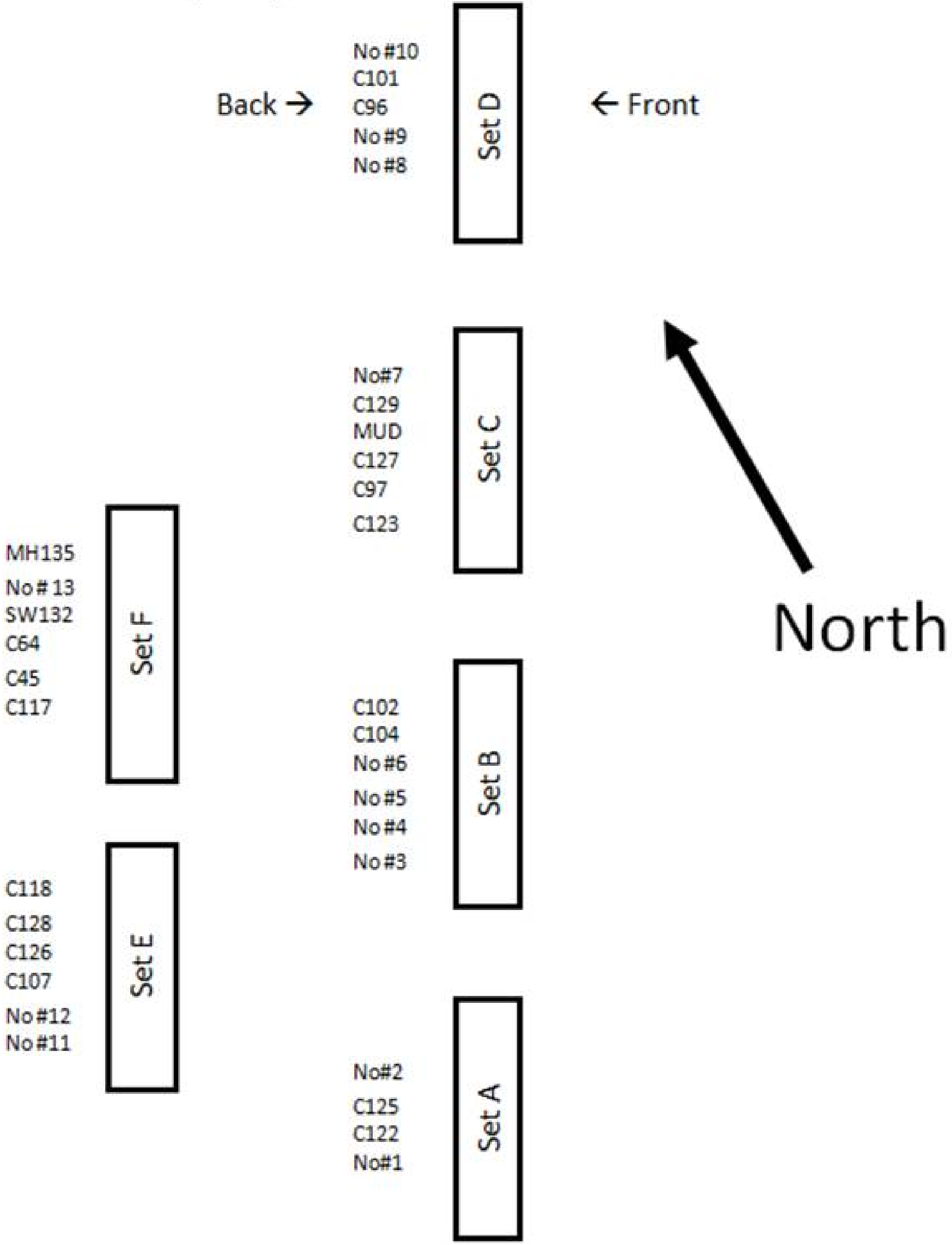

Bee Yard Map August 2010

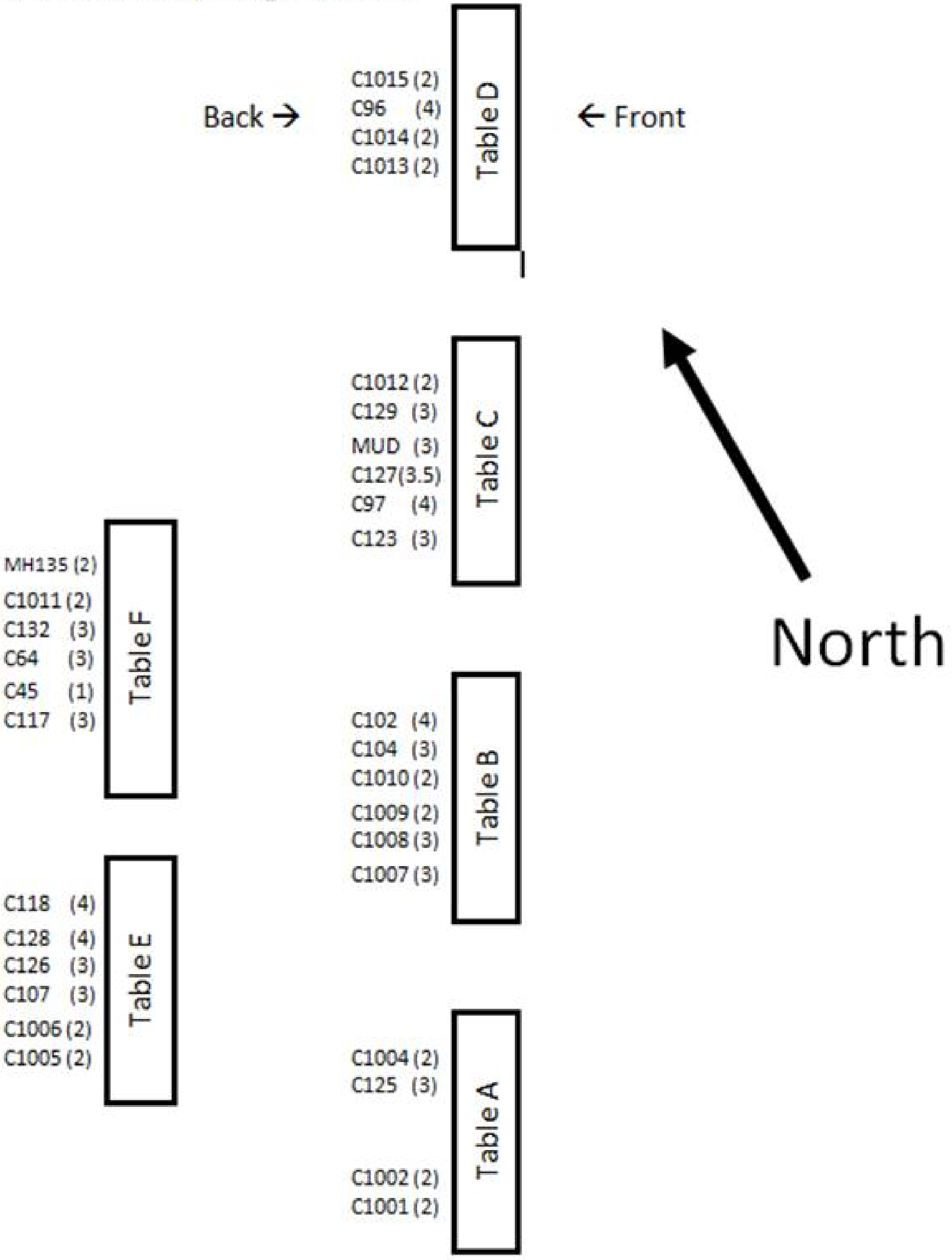

Bee Yard Map July 7-8, 2011

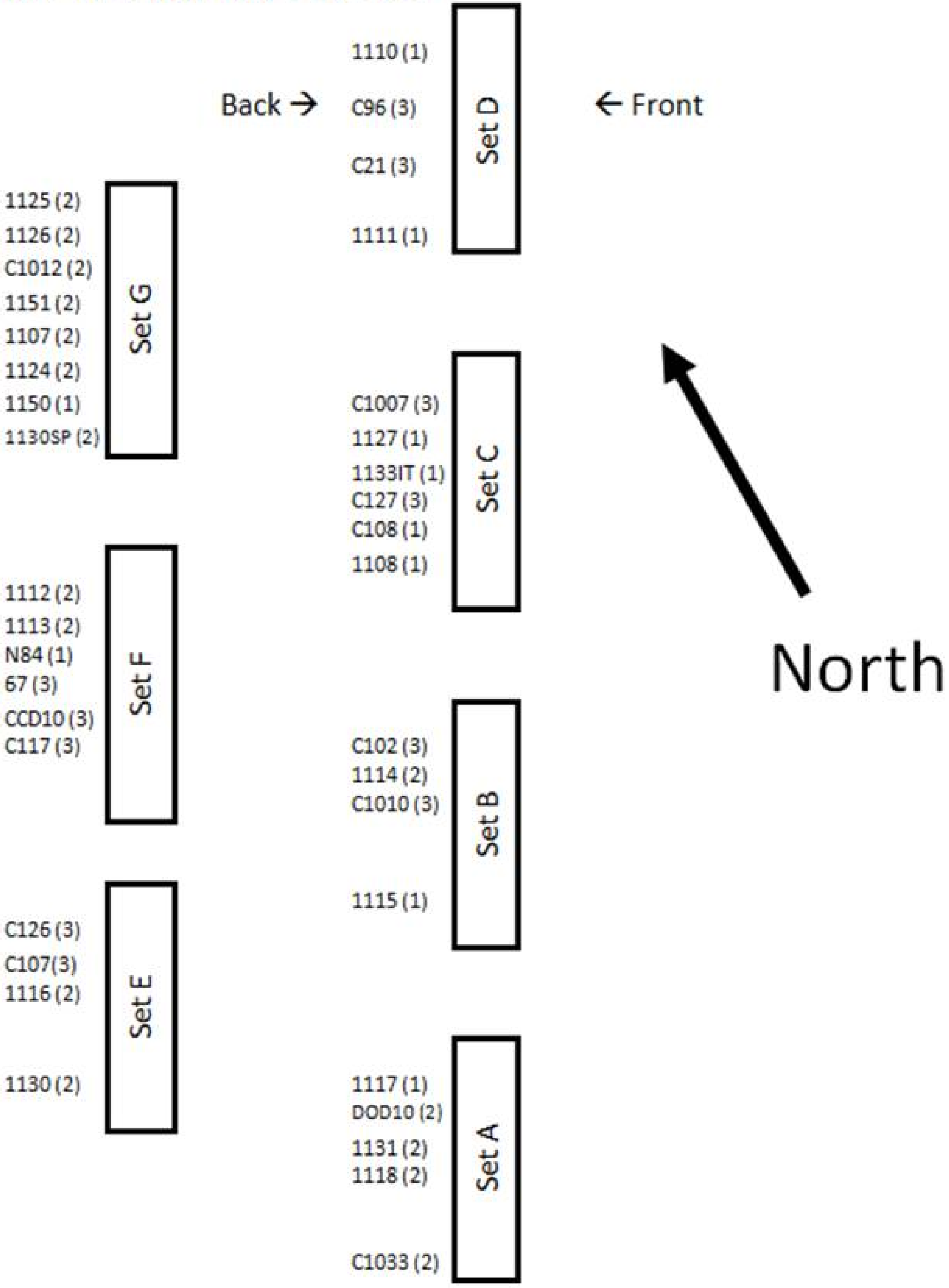

Bee Yard Map July 20-21, 2011

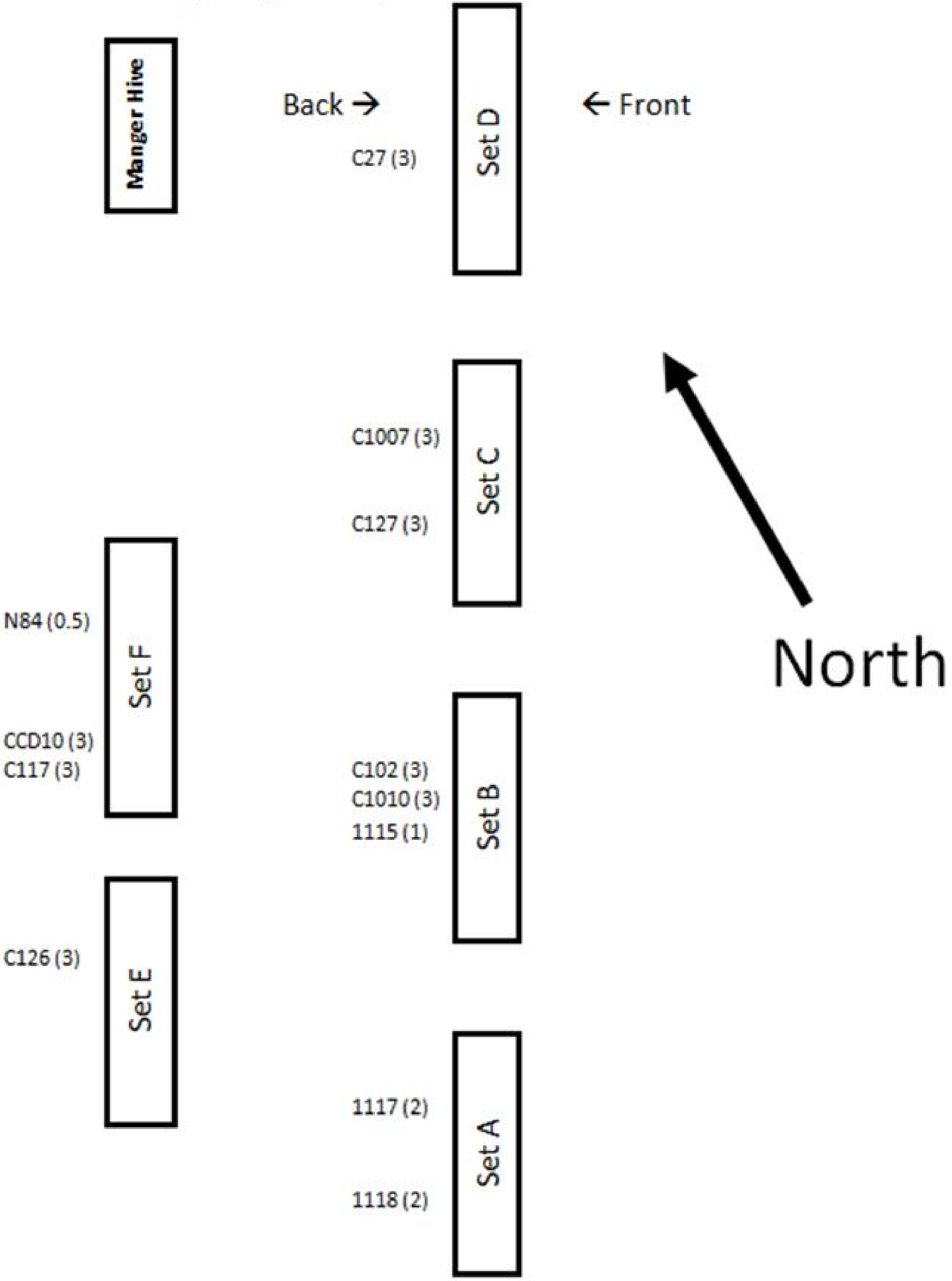

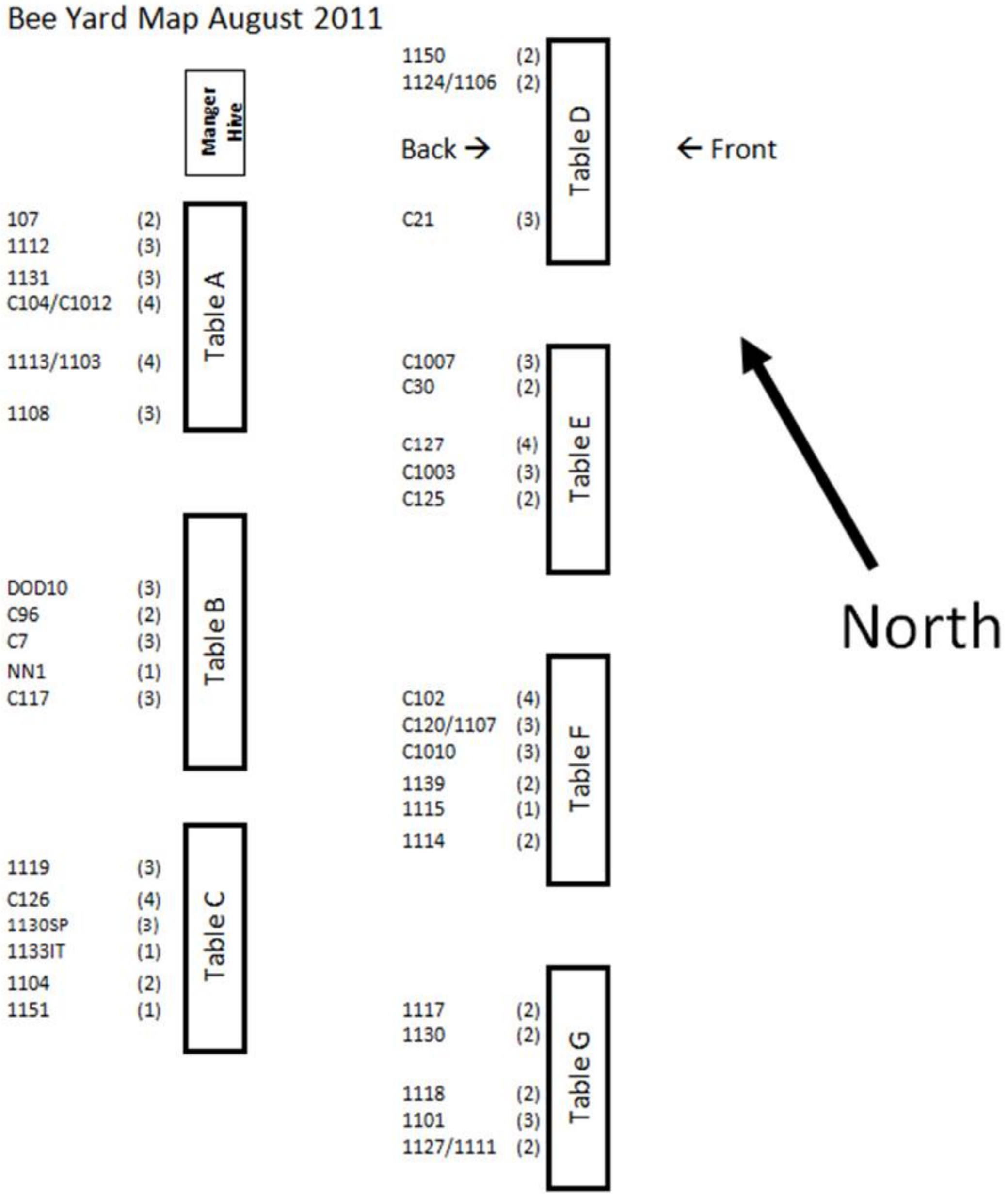

Bee Yard Map August 2011

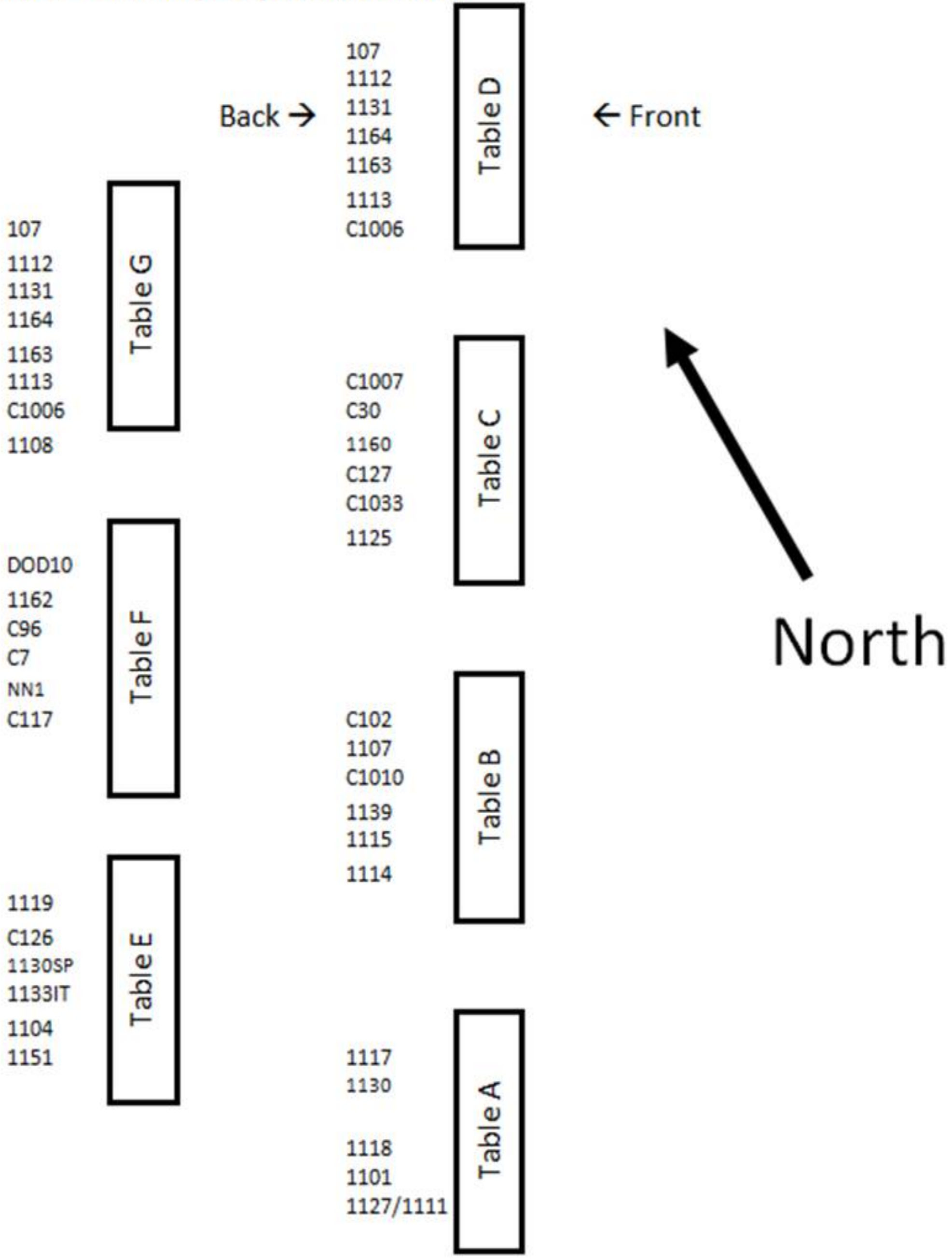

Bee Yard Map September 2011

APPENDIX B

BEE IMAGING PLOTS

July 2011

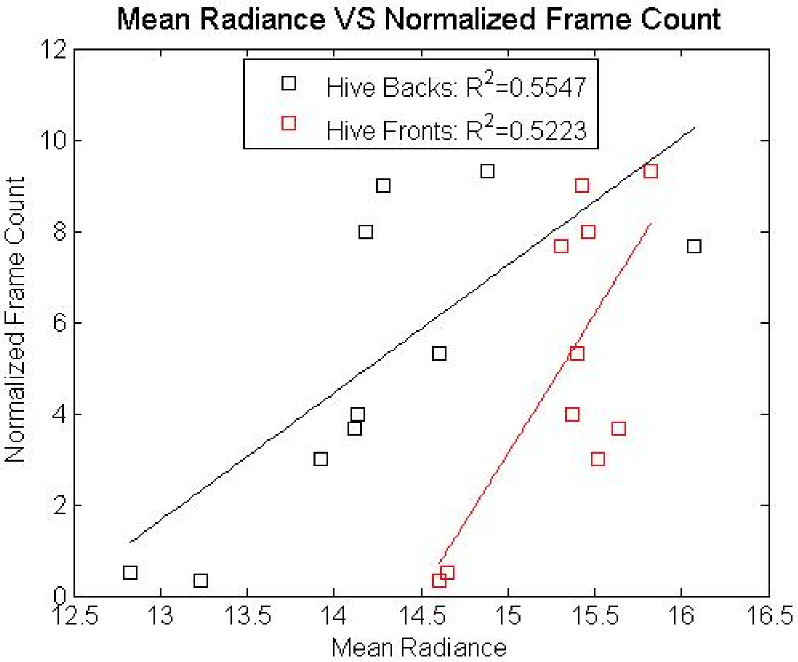

Figure 1. Mean radiance vs normalized frame count for 7/20/2011 PM 1.

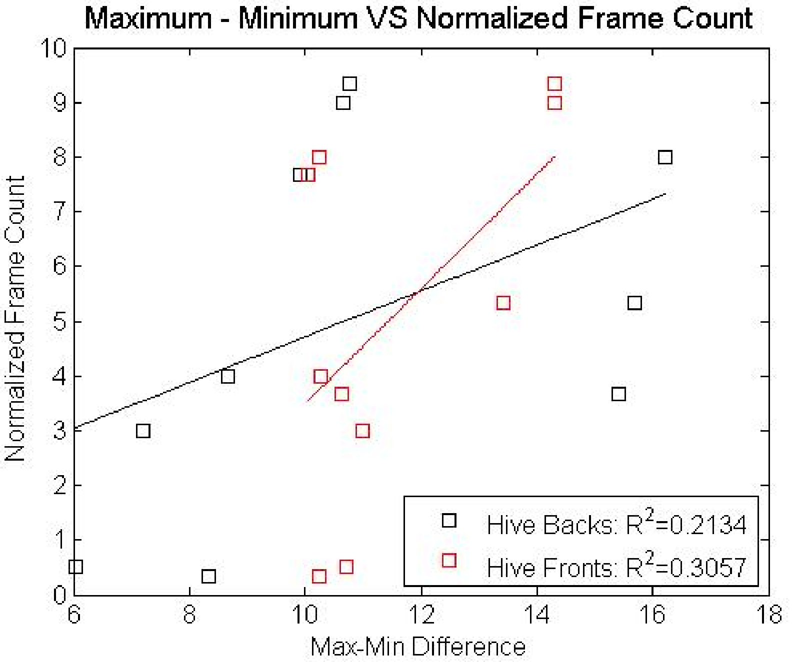

Figure 2. Difference between maximum and minimum radiance vs normalized frame count for 7/20/2011 PM 1

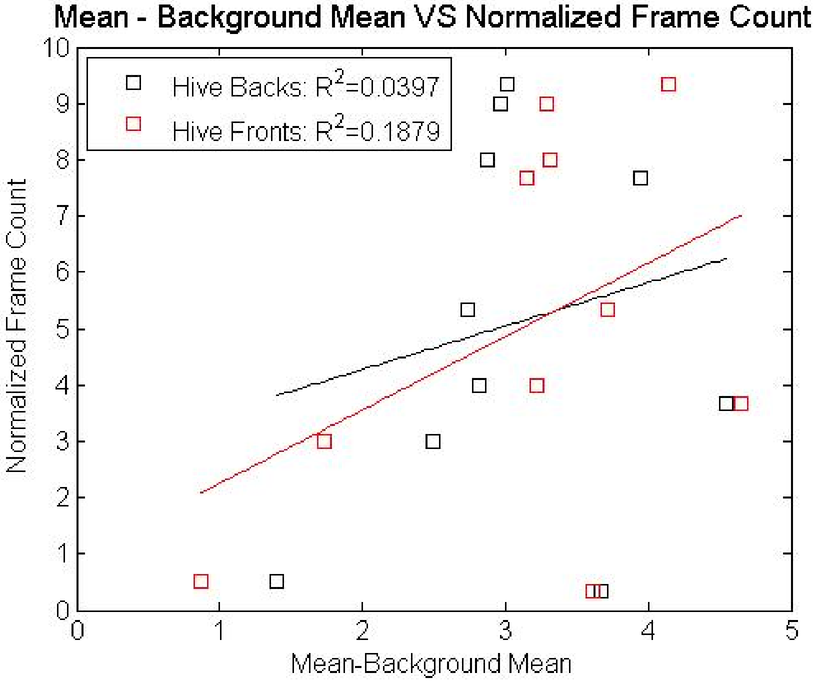

Figure 3. Difference between mean and background mean radiance vs normalized frame count for 7/20/2011 PM 1.

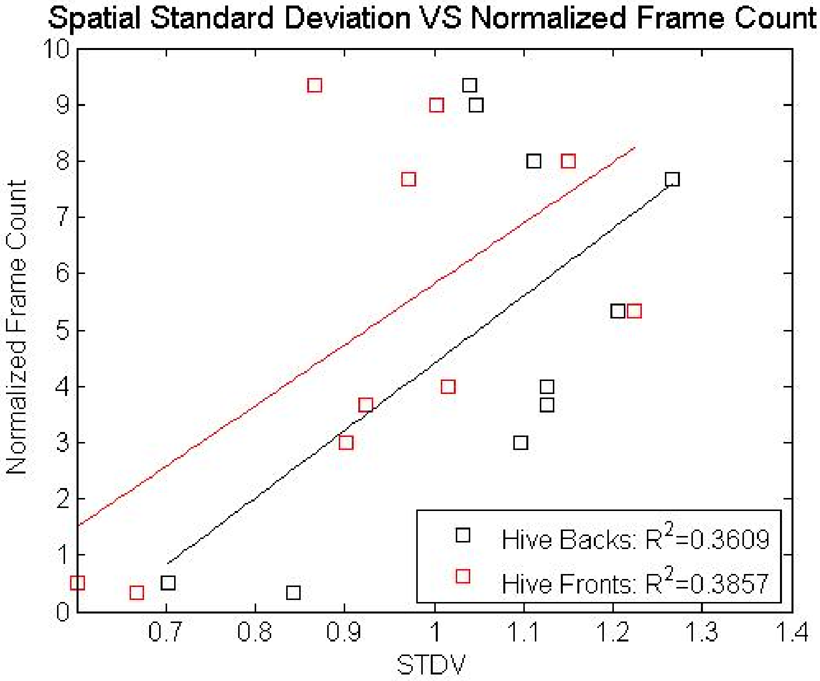

Figure 4. STDV vs normalized frame count for 7/20/2011 PM 1

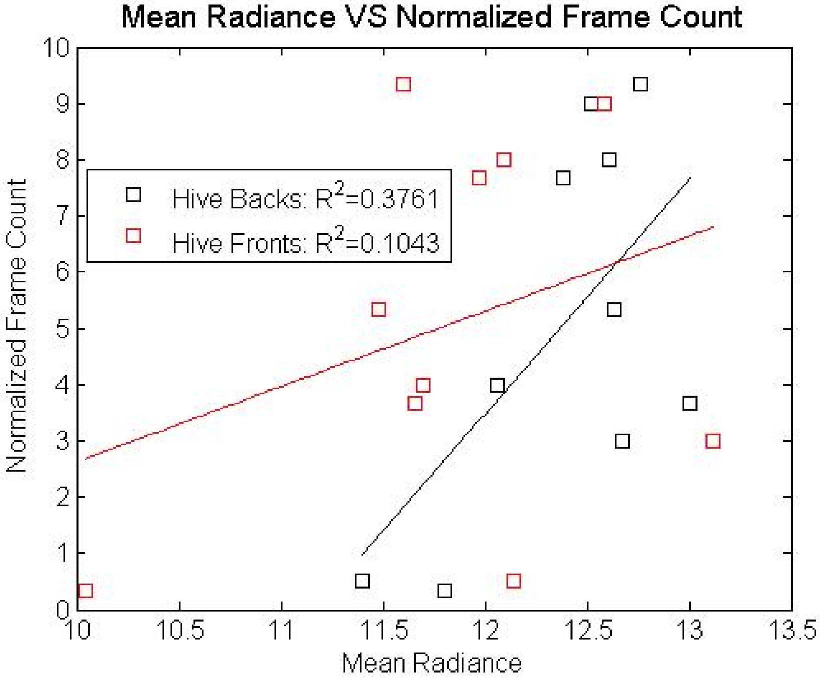

Figure 5. Mean radiance vs normalized frame count for 7/20/2011 PM 2.

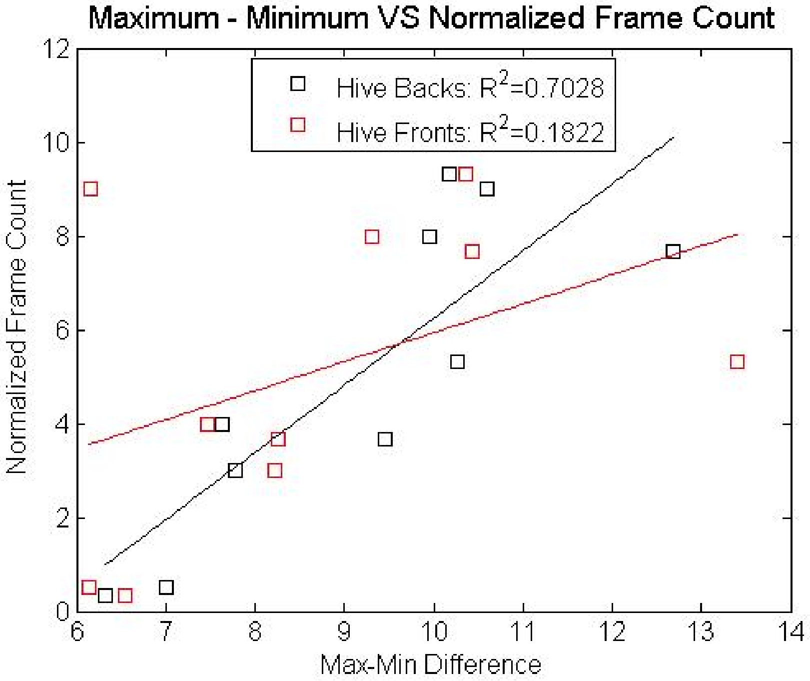

Figure 6. Difference between maximum and minimum radiance vs normalized frame count for 7/20/2011 PM 2.

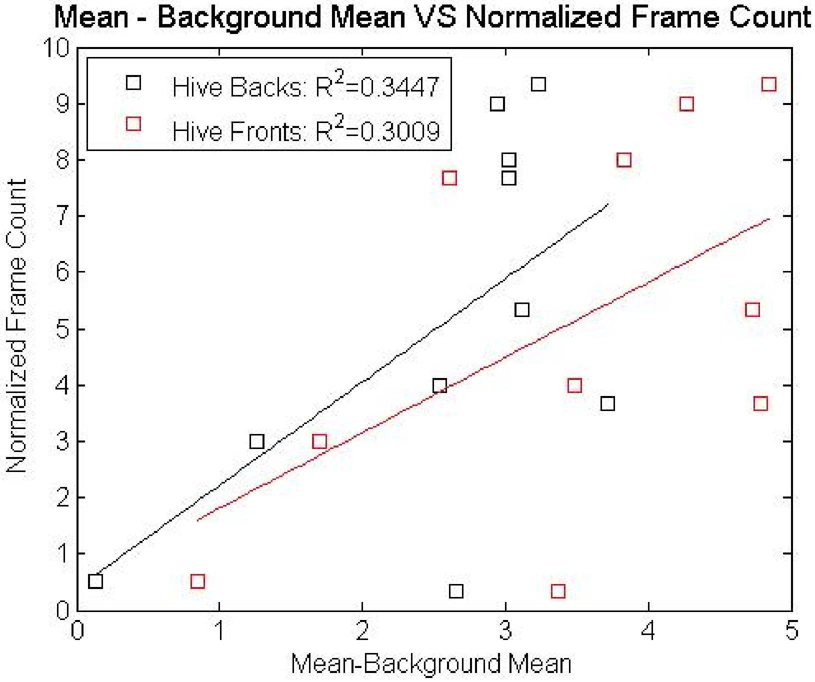

Figure 7. Difference between mean and background mean radiance vs normalized frame count for 7/20/2011 PM 2.

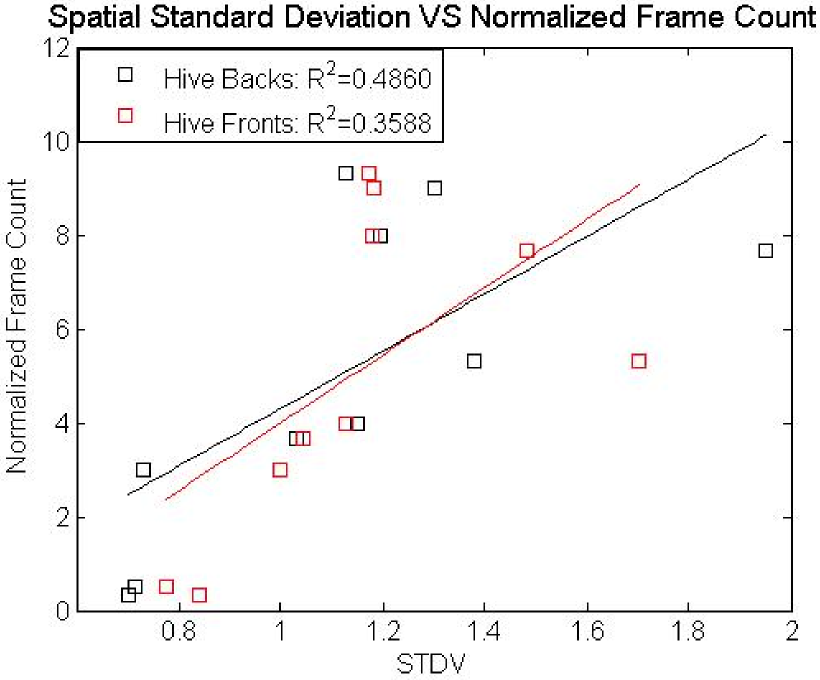

Figure 8. STDV vs normalized frame count for 7/20/2011 PM 2.

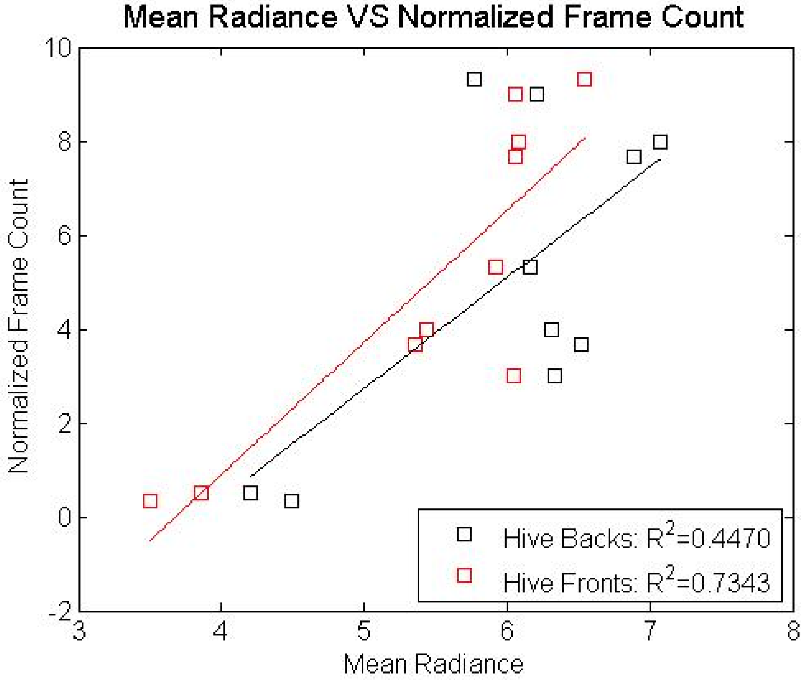

Figure 9. Mean radiance vs normalized frame count for 7/21/2011 AM.

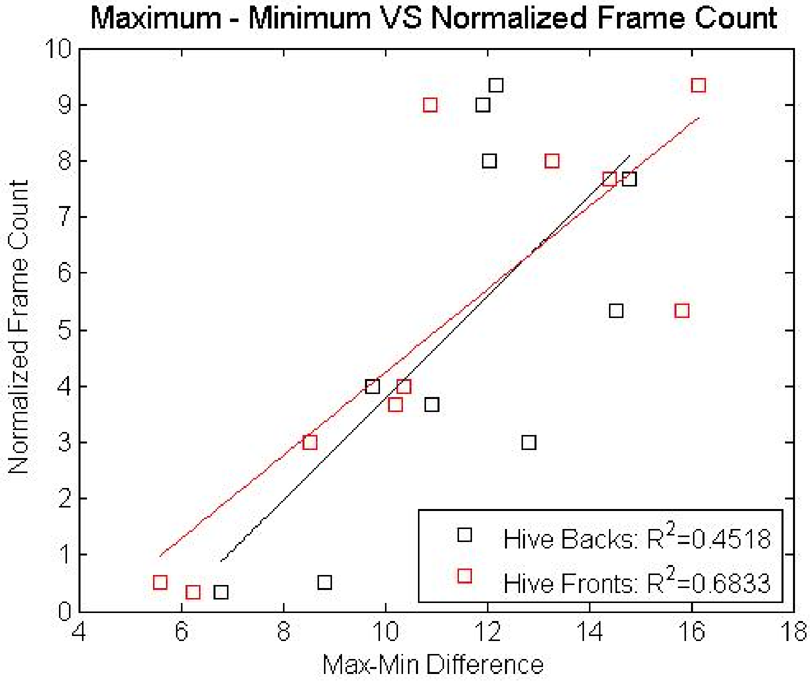

Figure 10. Difference between maximum and minimum radiance vs normalized frame count for 7/21/2011 AM.

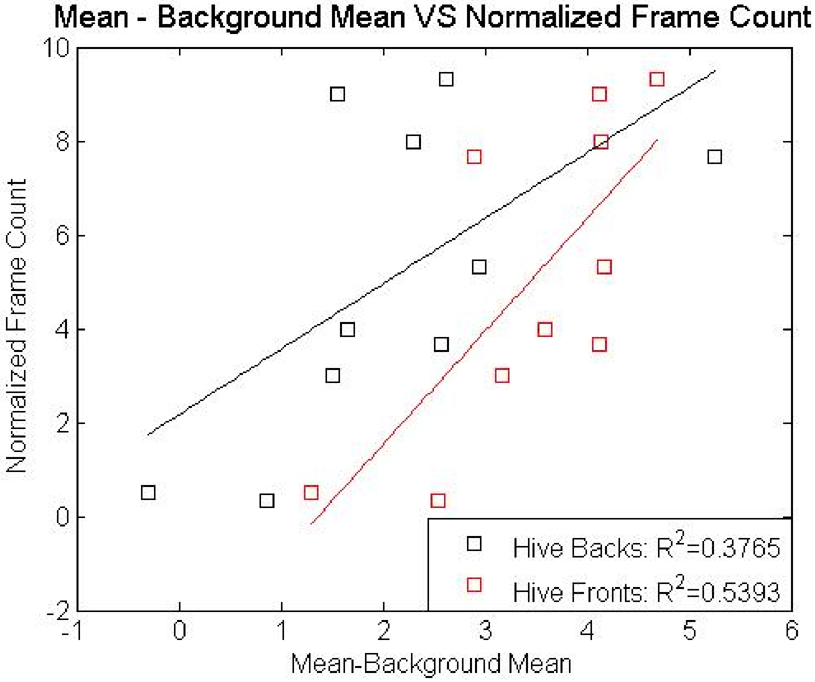

Figure 11. Difference between mean and background mean radiance vs normalized frame count for 7/21/2011 AM.

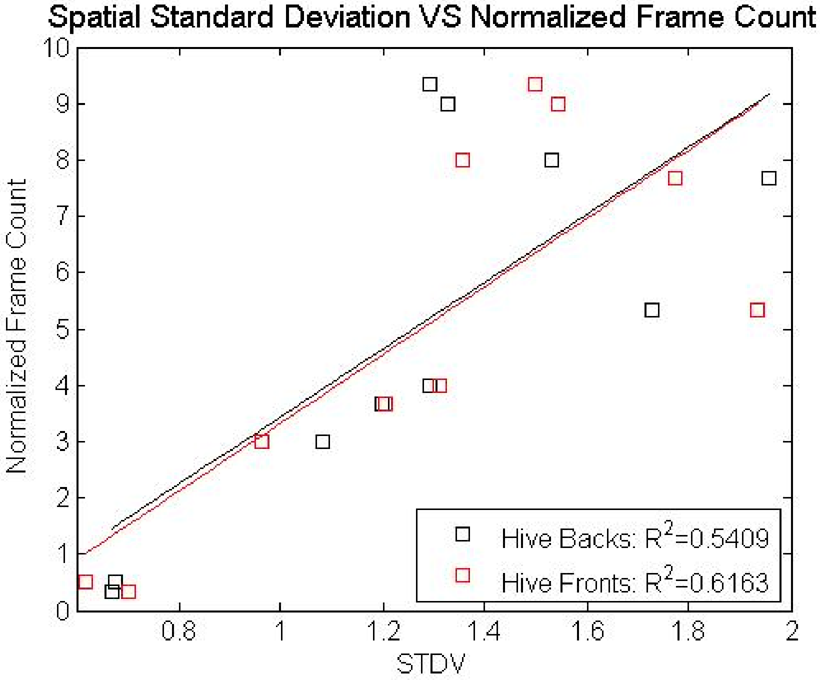

Figure 12. STDV vs normalized frame count for 7/21/2011 AM.

August 2011

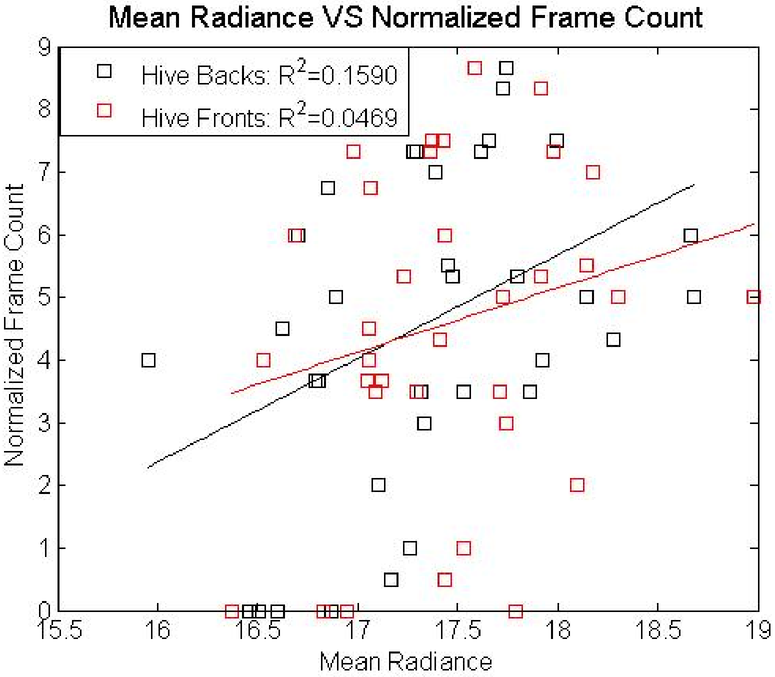

Figure 13. Mean radiance vs normalized frame count for 8/24/2011 PM.

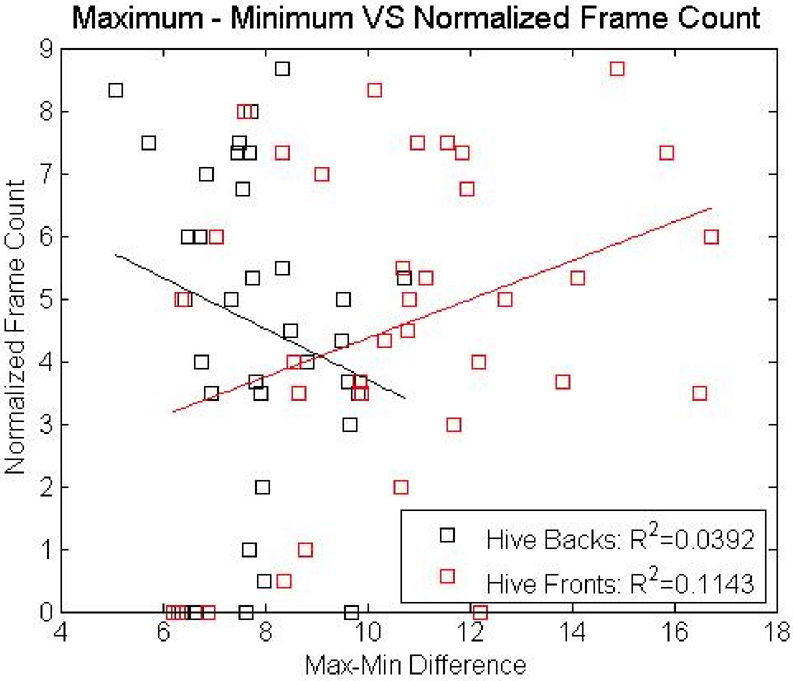

Figure 14. Difference between maximum and minimum radiance vs normalized frame count for 8/24/2011 PM.

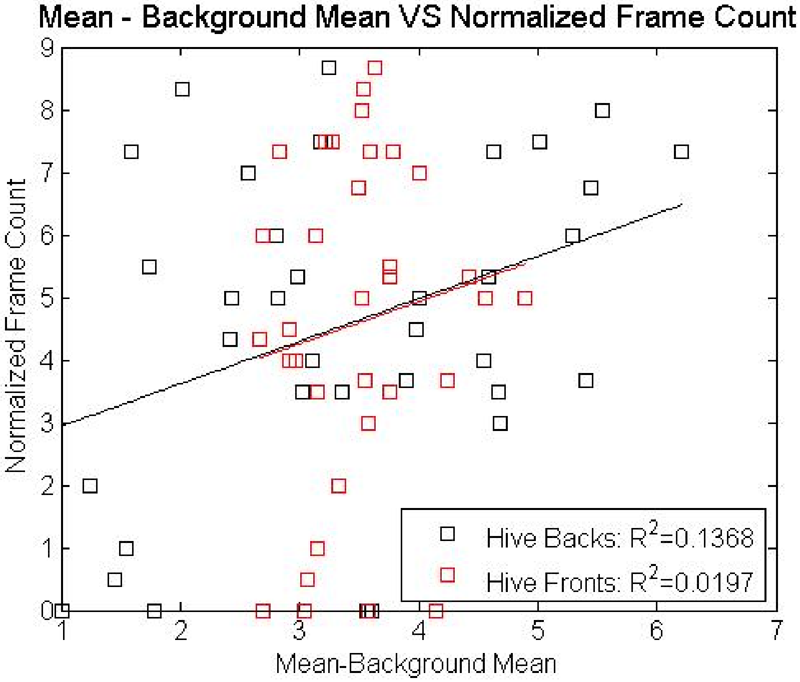

Figure 15. Difference between mean and background mean radiance vs normalized frame count for 8/24/2011 PM.

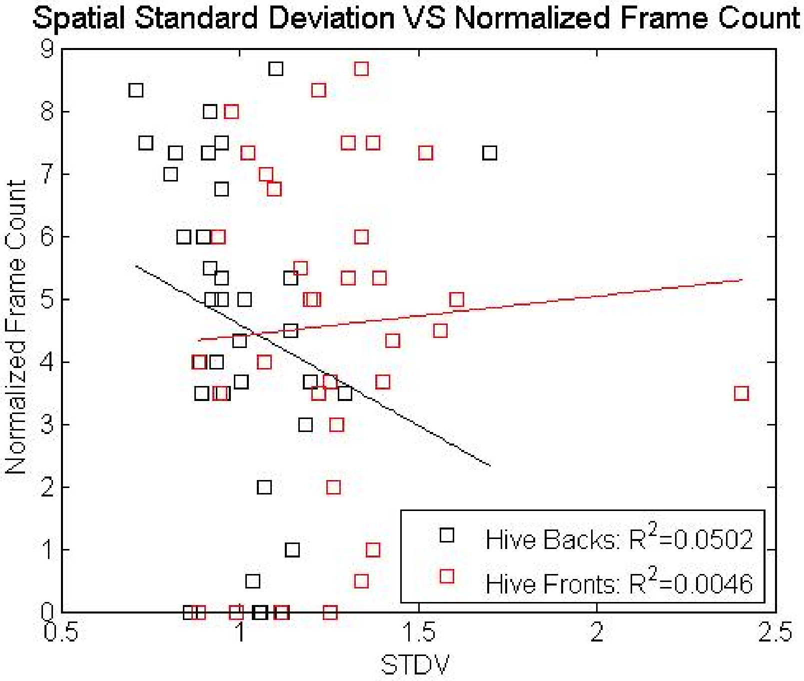

Figure 16. STDV vs normalized frame count for 8/24/2011 PM.

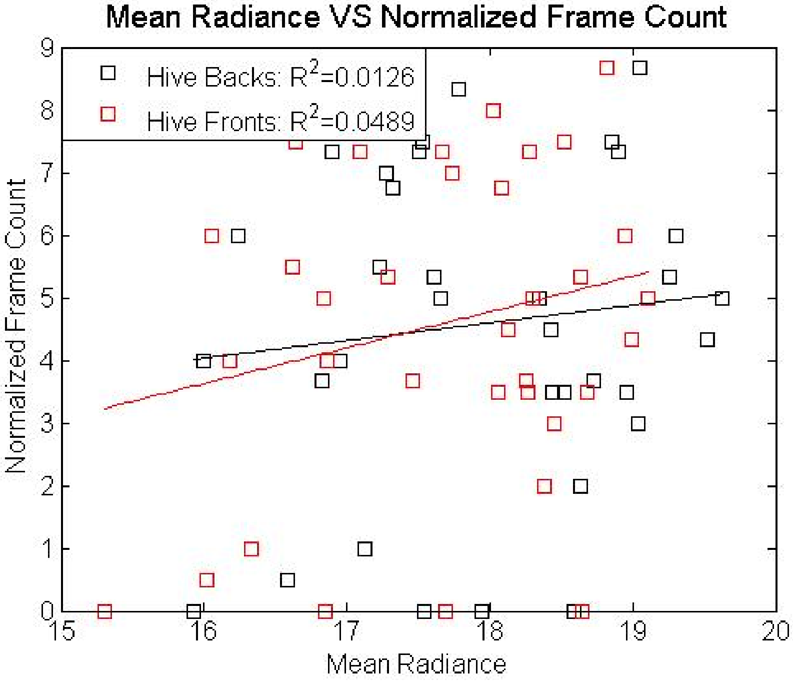

Figure 17. Mean radiance vs normalized frame count for 8/25/2011 AM.

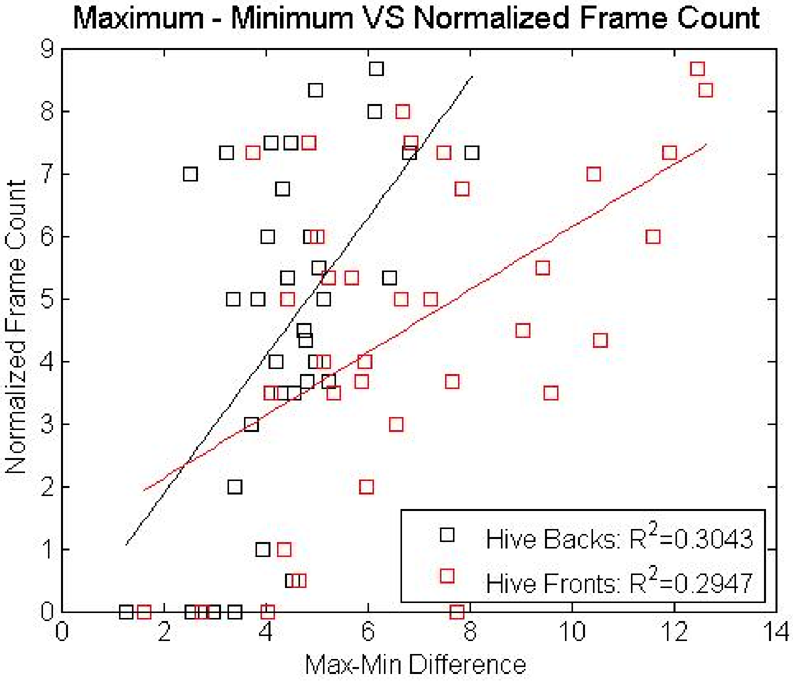

Figure 18. Difference between maximum and minimum radiance vs normalized frame count for 8/25/2011 AM.

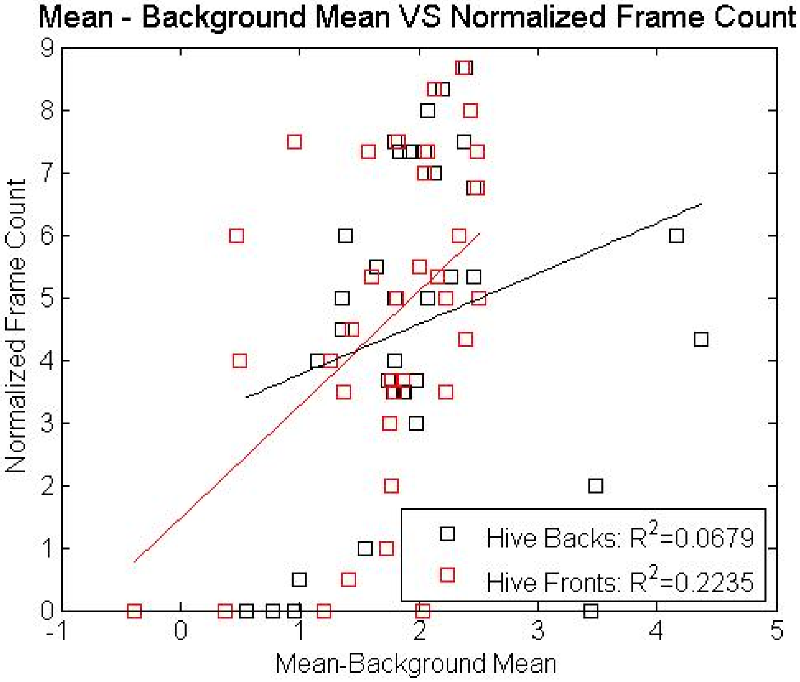

Figure 19. Difference between mean and background mean radiance vs normalized frame count for 8/25/2011 AM.

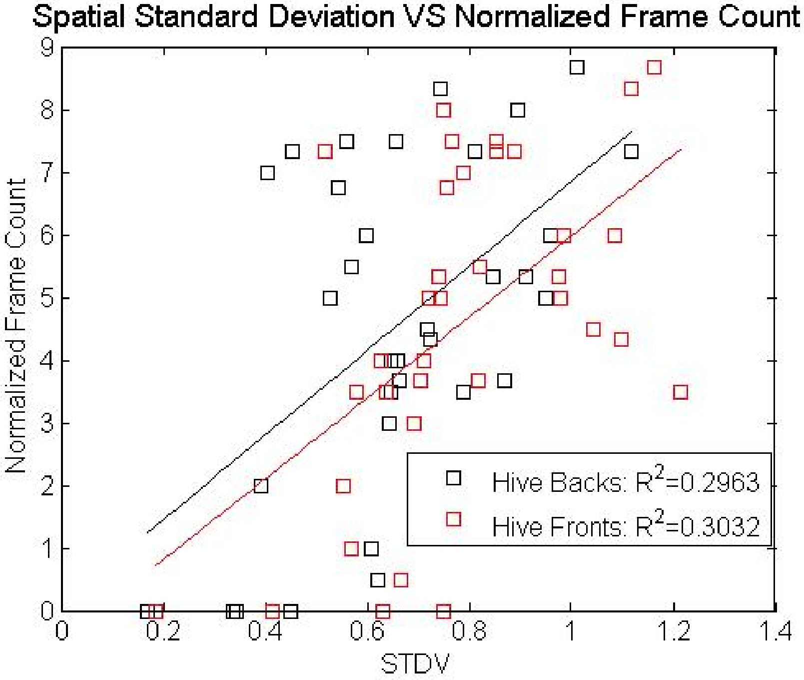

Figure 20. STDV vs normalized frame count for 8/25/2011 AM.

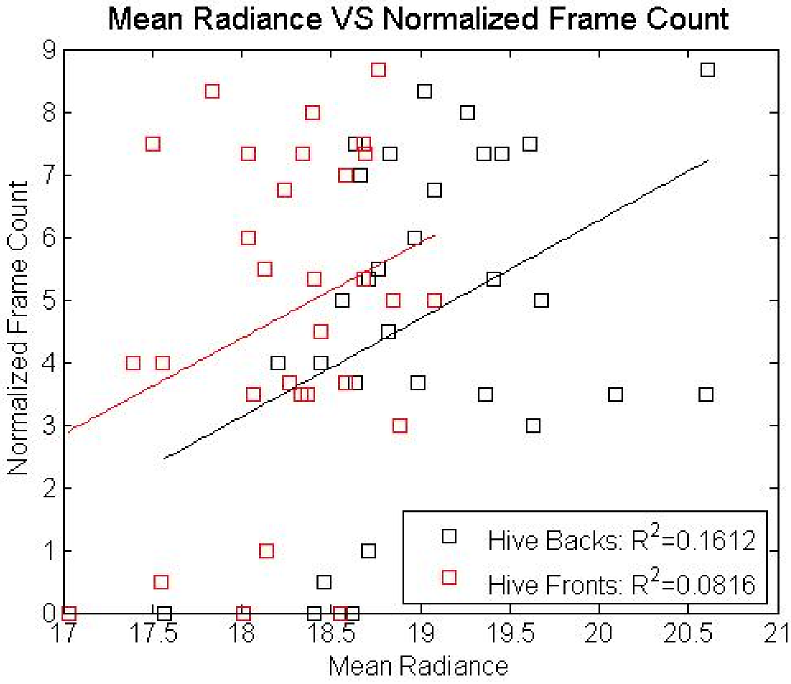
Mean Radiance VS Normalized Frame Count

Figure 21. Mean radiance vs normalized frame count for 8/25/2011 PM.

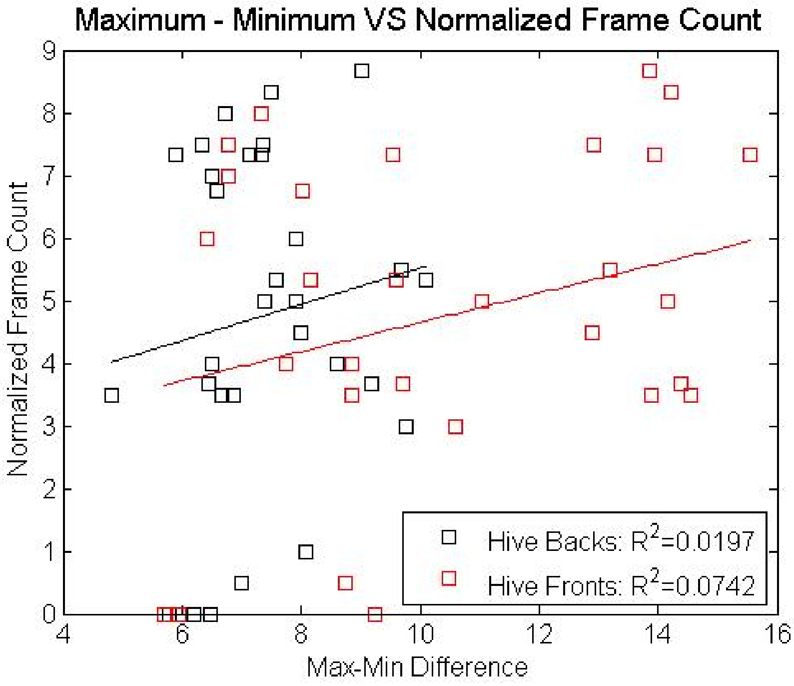
Maximum - Minimum VS Normalized Frame Count

Figure 22. Difference between maximum and minimum radiance vs normalized frame count for 8/25/2011 PM.

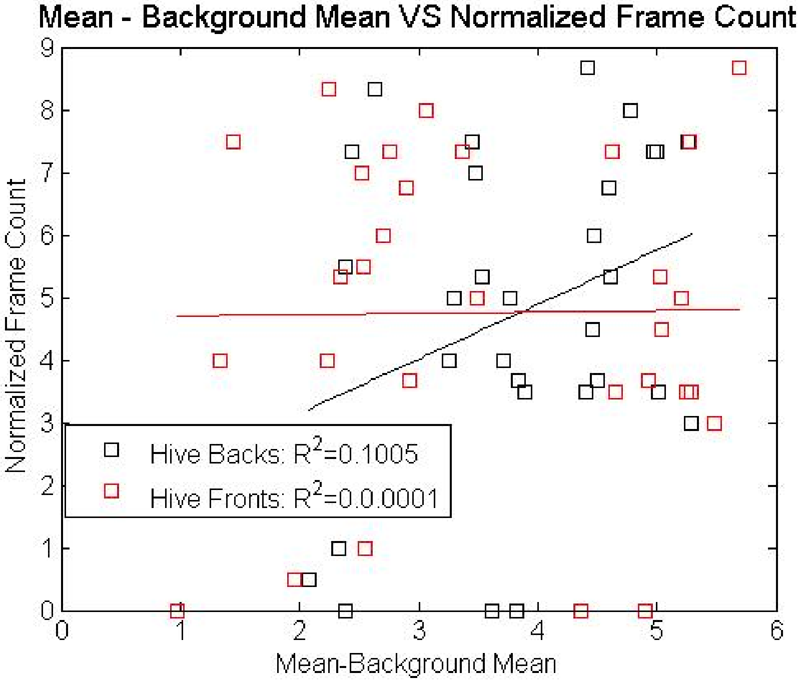

Figure 23. Difference between mean and background mean radiance vs normalized frame count for 8/25/2011 PM.

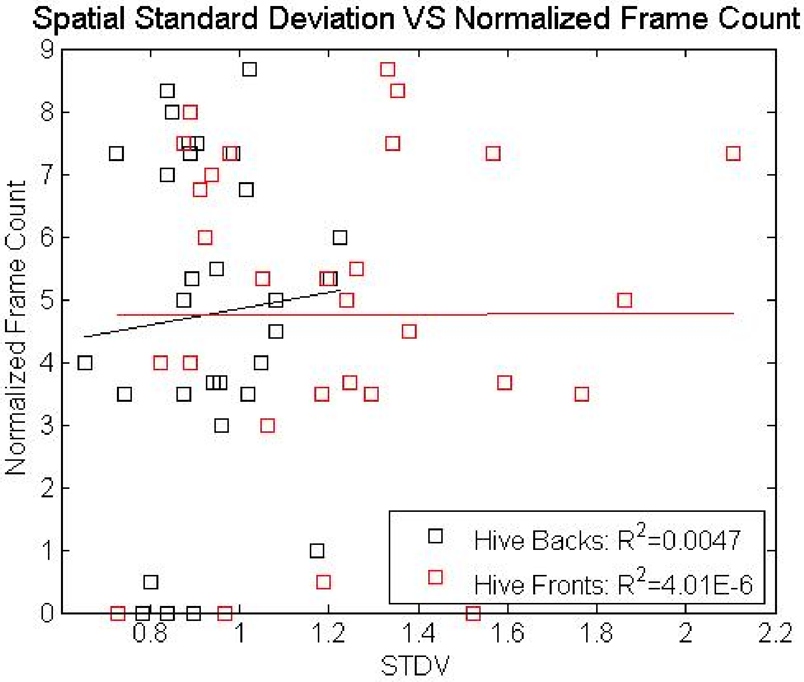

Figure 24. STDV vs normalized frame count for 8/25/2011 PM.

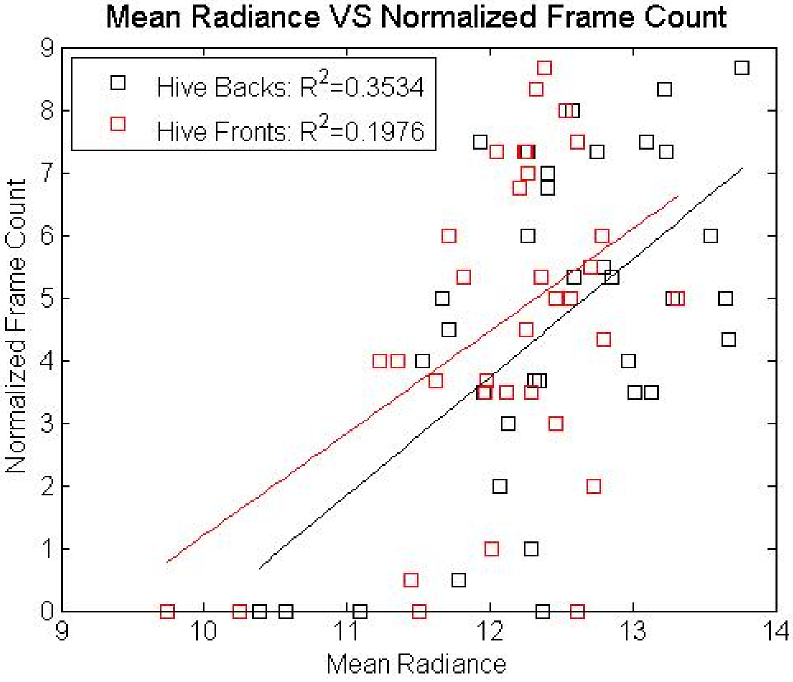

Figure 25. Mean radiance vs normalized frame count for 8/26/2011 AM.

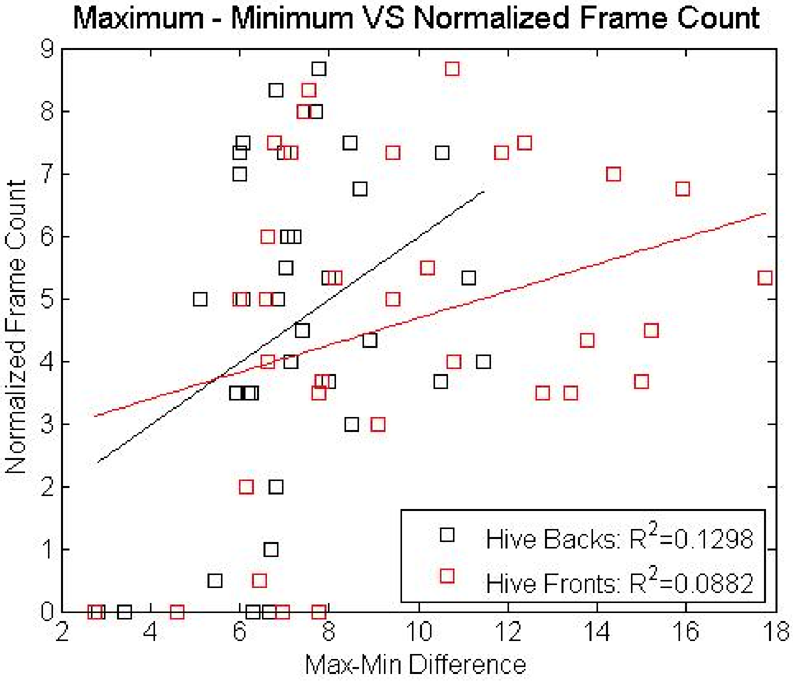

Figure 26. Difference between maximum and minimum radiance vs normalized frame count for 8/26/2011 AM.

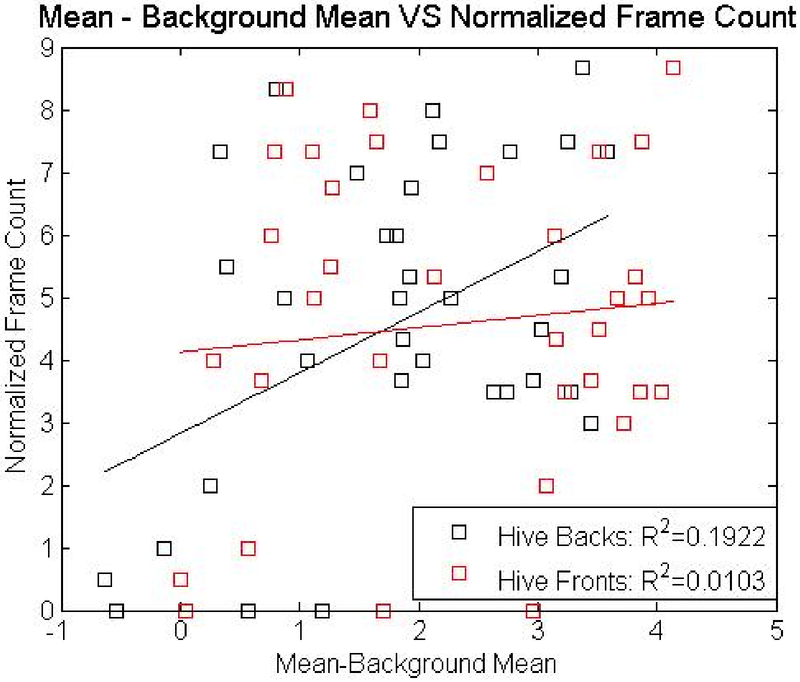

Figure 27. Difference between mean and background mean radiance vs normalized frame count for 8/26/2011 AM.

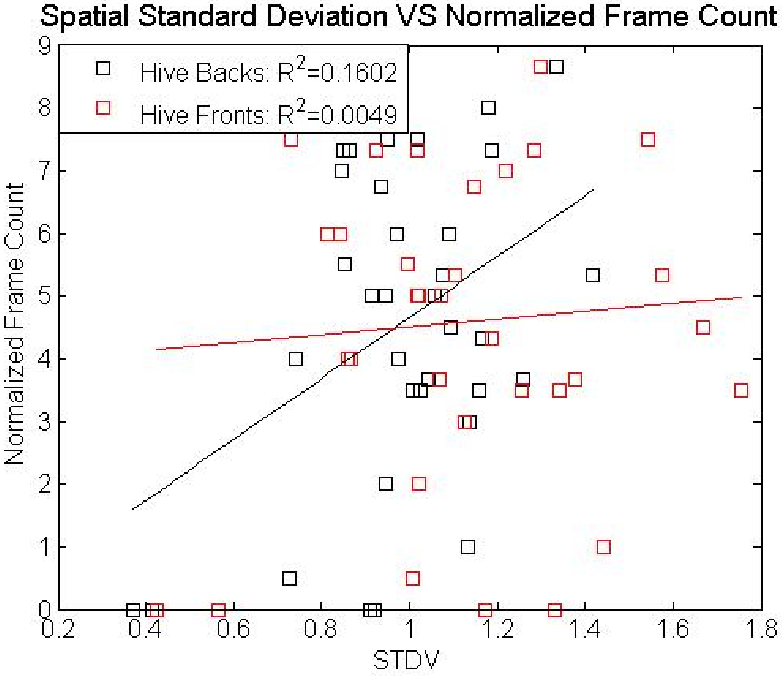

Figure 28. STDV vs normalized frame count for 8/26/2011 AM.

September 2011

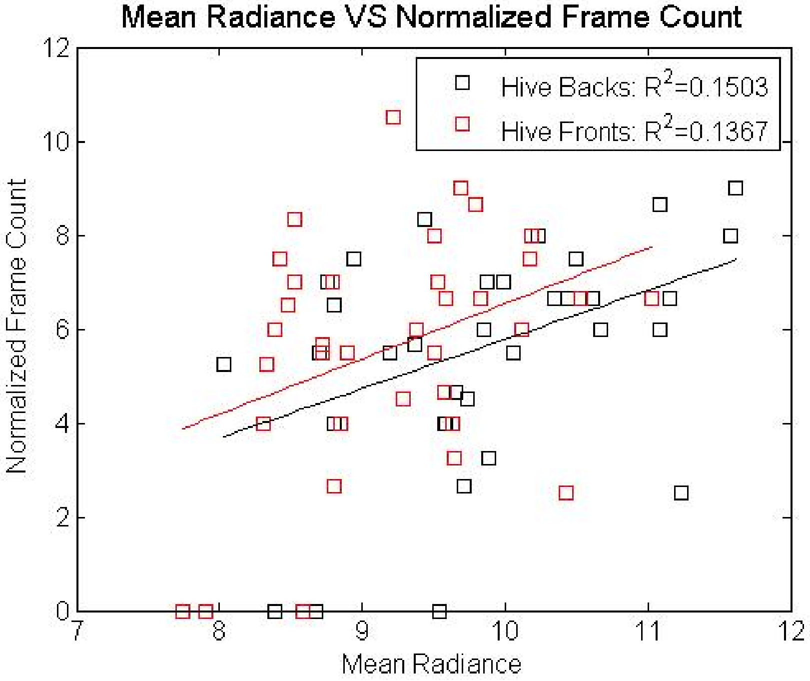

Figure 29. Mean radiance vs normalized frame count for 9/21/2011 PM.

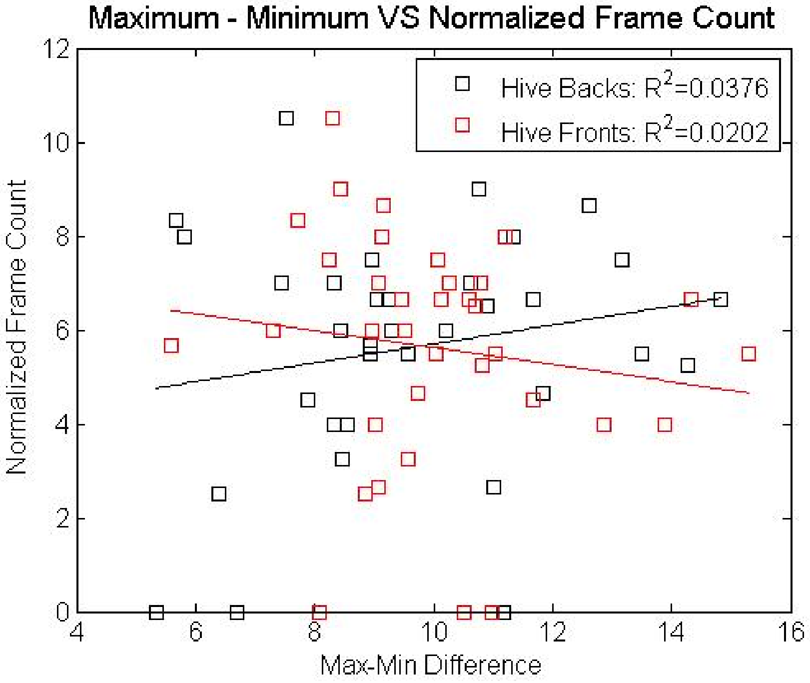

Figure 30. Difference between maximum and minimum radiance vs normalized frame count for 9/21/2011 PM.

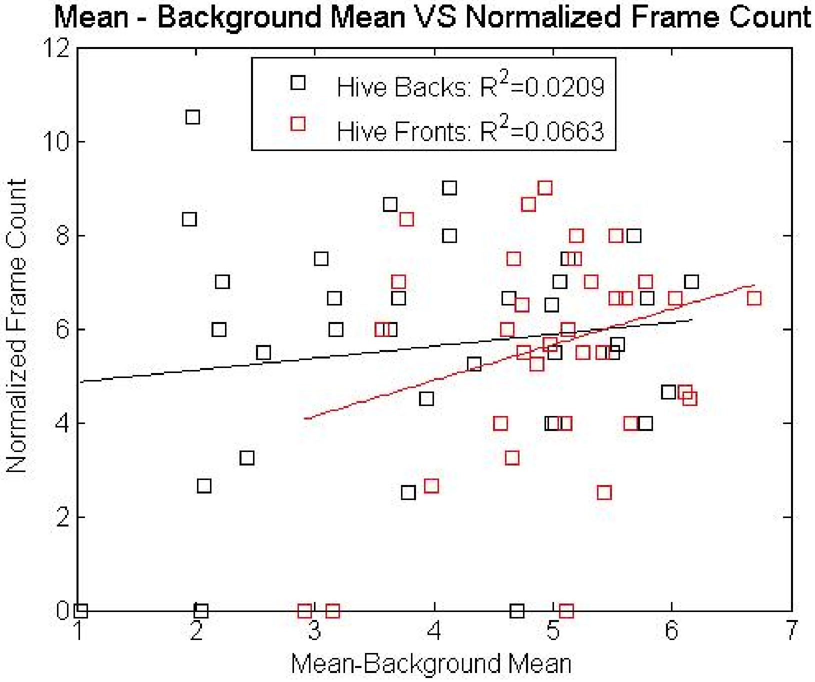

Figure 31. Difference between mean and background mean radiance vs normalized frame count for 9/21/2011 PM.

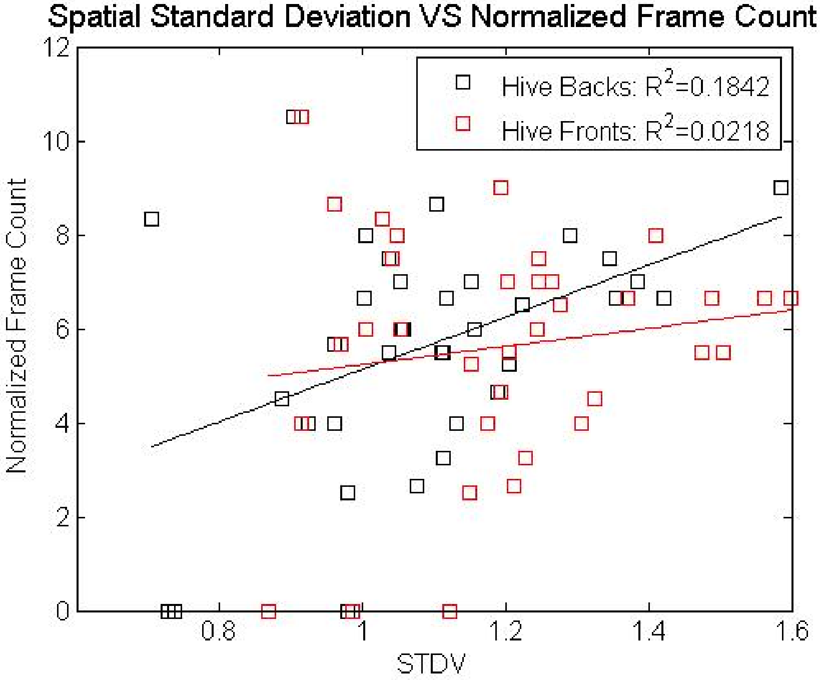

Figure 32. STDV vs normalized frame count for 9/21/2011 PM.

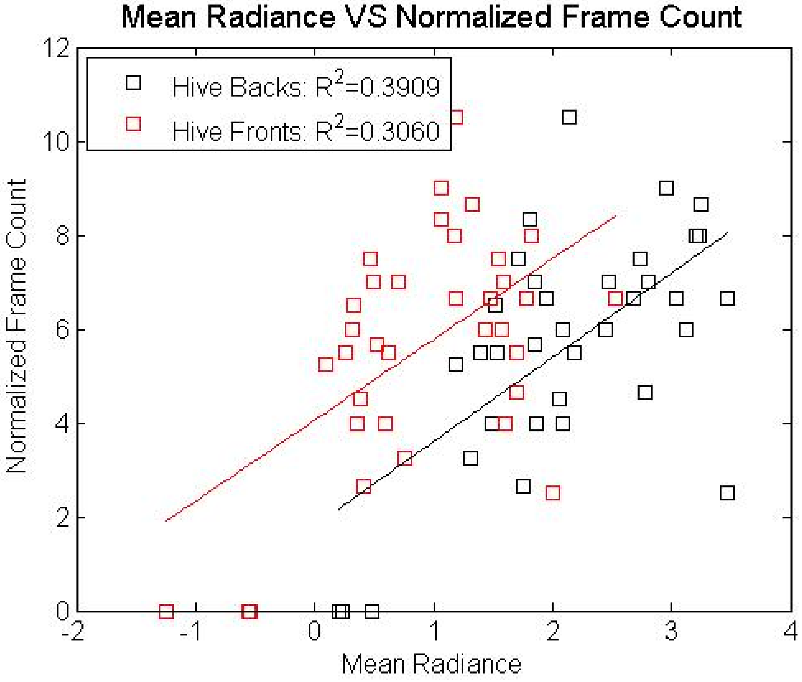

Figure 33. Mean radiance vs normalized frame count for 9/22/2011 AM.

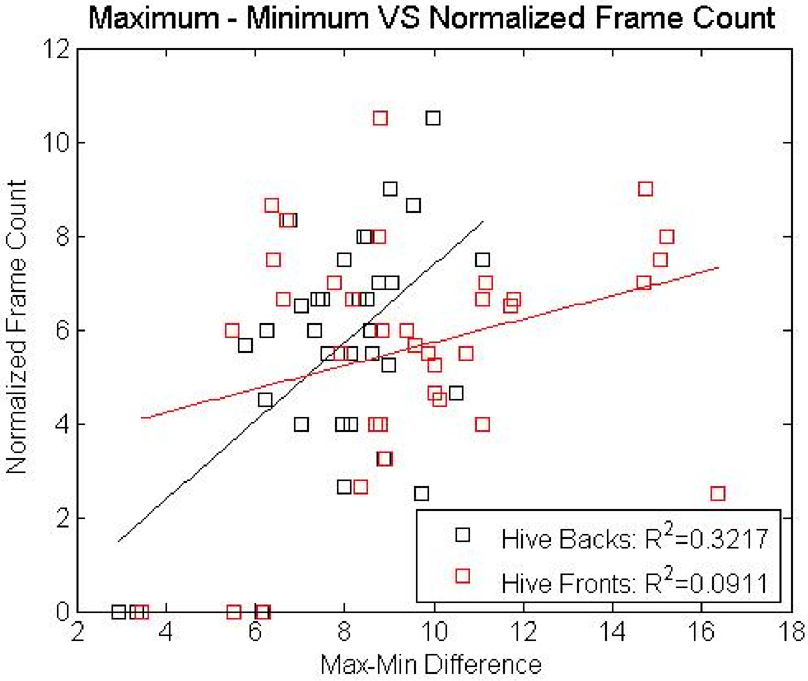

Figure 34. Difference between maximum and minimum radiance vs normalized frame count for 9/22/2011 AM.

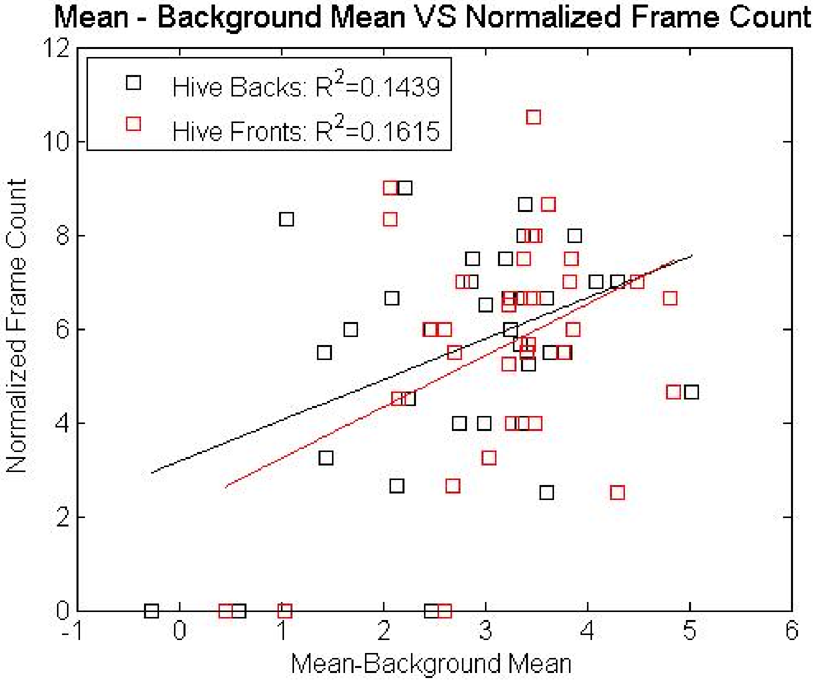

Figure 35. Difference between mean and background mean radiance vs normalized frame count for 9/22/2011 AM.

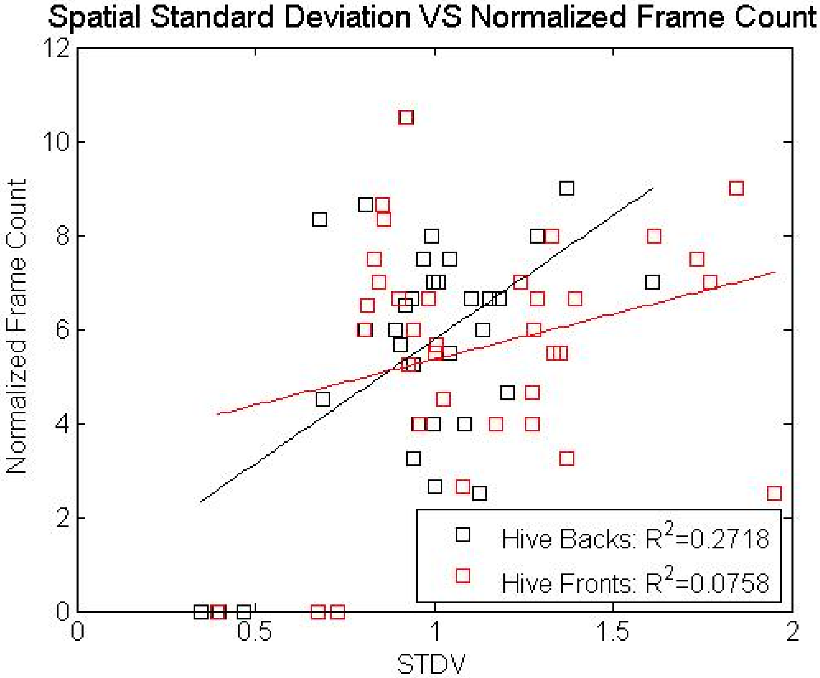

Figure 36. STDV vs normalized frame count for 9/22/2011 AM.